STUDY OF SYNTHETIC ELECTRIC AND MAGNETIC FIELDS IN THIRD ORDER NONLINEAR OPTICAL PROCESS

By

Soumik Nandi

PHYS11201904007

National Institute of Science Education and Research, Bhubaneswar

A thesis submitted to the

Board of Studies in Physical Sciences

In partial fulfillment of requirements

for the Degree of

DOCTOR OF PHILOSOPHY

of

HOMI BHABHA NATIONAL INSTITUTE

December, 2025

Homi Bhabha National Institute[1]

Recommendations of the Viva Voce Committee

As members of the Viva Voce Committee, we certify that we have read the dissertation prepared by **Soumik Nandi** entitled "**Study of synthetic electric and magnetic fields in third order nonlinear optical process**" and recommend that it may be accepted as fulfilling the thesis requirement for the award of Degree of Doctor of Philosophy.

S. No.	Doctoral Committee	Name	Signature	Date	In-Person/ Online
1.	Chairman	Dr. Kartikeswar Senapati	K. Senapati 17/04/26	17/04/2026	In-Person
2.	Guide/Convener	Dr. Ashok K Mohapatra	A.K.Mohapt	17/04/2026	In-Person
3.	Co-Guide (if any)	Dr. Ritwick Das	Ritwick Das	17/04/2026	In-Person
4.	Examiner	Dr. Akhilesh Kumar Mishra		17/04/2026	In-Person
5.	Member - 1	Dr. Kush Saha		17/4/26	Online
6.	Member - 2	Dr. Shovon Pal		17/4/26.	In-Person
7.	Member - 3	Dr. Biju Rajasekhar		17/04/2026	Online

Final approval and acceptance of this thesis is contingent upon the candidate's submission of the final copies of the thesis to HBNI.

I/We hereby certify that I/we have read this thesis prepared under my/our direction and recommend that it may be accepted as fulfilling the thesis requirement.

Date: 17/04/26

Place: Bhubaneswar

Ritwick Das 17/04/2026

Signature

Co-guide

Signature

A.K.Mohapt 17/04/2026

Guide

[1] This page is to be included only for final submission after successful completion of viva voce

STATEMENT BY AUTHOR

This dissertation has been submitted in partial fulfillment of requirements for an advanced degree at Homi Bhabha National Institute (HBNI) and is deposited in the Library to be made available to borrowers under rules of the HBNI.

Brief quotations from this dissertation are allowable without special permission, provided that accurate acknowledgement of source is made. Requests for permission for extended quotation from or reproduction of this manuscript in whole or in part may be granted by the Competent Authority of HBNI when in his or her judgment the proposed use of the material is in the interests of scholarship. In all other instances, however, permission must be obtained from the author.

Soumik Nandi

(Soumik Nandi)

DECLARATION

I, hereby declare that the investigation presented in the thesis has been carried out by me. The work is original and has not been submitted earlier as a whole or in part for a degree / diploma at this or any other Institution / University.

Soumik Nandi

(Soumik Nandi)

CERTIFICATION ON ACADEMIC INTEGRITY

Undertaking by the Student

1. I, **Soumik Nandi**, HBNI Enrolment No. **PHYS11201904007** hereby undertake that the thesis titled "**Study of synthetic electric and magnetic field in third order non-linear optical process**" is prepared by me and is an original work undertaken by me.
2. I also hereby undertake that this document has been duly checked through a plagiarism detection tool and the document is found to be plagiarism free as per the guidelines of the Institute/ UGC.
3. I am aware and undertake that if plagiarism is detected in my thesis at any stage in the future, suitable penalty will be imposed as per the guidelines of the Institute/ UGC.

Soumik Nandi 17/04/26
Signature of the Student with date

Endorsed by the Thesis Supervisor

I certify that the thesis written by the researcher is plagiarism free as mentioned above by the student.

A Mohapt
17/04/2026
Signature of the Thesis Supervisor with date

Name : Dr. Ashok K Mohapatra
Designation : Associate Professor
Department/ Centre : School of Physical Sciences
Name of the CI/ OCC : NISER Bhubaneswar

List of Publications arising from the thesis

Journal

1. "All-optical Stern-Gerlach effect in parity-time anti-symmetric nonlinear refractive medium", S. Nandi, A. Ghosh, D. Beniwal, A. Mondal, A. K. Mohapatra, and R. Das, Optics Express, **2025**, 33, 24237–24248.

2. "All-optical synthetic spin-Hall effect in third-order nonlinear optics", S. Nandi, A. Ghosh, A. K. Mohapatra, and R. Das, (manuscript accepted for publication in Journal of the Optical Society of America B).

Conferences

1. Conference on Optics, Photonics and Quantum Optics (COPaQ) 2022, 10 - 13 November 2022, IIT Roorkee.

2. DAE-BRNS National Laser Symposium (NLS 31), 3 - 6 December 2022, IIT Kharagpur.

3. 16th International Conference on Fiber Optics and Photonics, 12 - 15 December 2024, IIT Kharagpur.

Soumik Nandi

(Soumik Nandi)

DEDICATIONS

To Maa and Baba

ACKNOWLEDGMENTS

I want to first thank Dr. Ritwick Das and Dr. Ashok K Mohapatra for their continuous guidance throughout this journey. It has helped me to come out of a depressed situation and it has motivated me a lot. I got my self-confidence back due to their support. My PhD journey would remain incomplete without the support of the following people: Abhishek da, Anupa di, Rashmi di, Shailja di, Survi di and Sujit da, who were my seniors and really helped me to in experimental setups. I would like to thank the scientific officers and technicians of the School of Physical Sciences who supported me by providing a few critical equipment required for the experimental setup. Also, I have got support from my juniors, especially from Arannya, in performing experiments. Other juniors like Tousif, Nandini, Purvesh, Dipendu and Smaran have extended their support in different scenarios. Having friends like Rahul, Subhadip, and Atanu da, discussing current topics, has really made me enthusiastic to look at things from a different perspective. Now, I want the affection, love and courage from my parents that have helped to shape my current state. Finally, and most importantly, I want to thank myself because to get the degree, I have to sacrifice many things but I keep myself in the run to finish the things.

Contents

Summary

Synthetic fields in optics have gained attention over the past several years. It helps to bring the dynamics of different optical systems, like different modes in coupled waveguides, forward and backward propagating beams in photonic crystal, signal and idler beam generation through nonlinear optical process in atomic system etc., under the umbrella of a single unified formalism in the form of synthetic fields. But the study of synthetic fields in third-order nonlinear susceptibility ($\chi^{(3)}$) led phenomena are inadequate till date. So, in this thesis, I have considered the filamentation process arising from self action effect of a beam (called pump) as a result of the medium's third-order nonlinearity. Two symmetric perturbations created in the filamentation are differentiated by their transverse beam profile. The differential wave equations of these generated beams are modelled in the form of quantum mechanical Schrödinger equation in a suitable transformed frame of reference. The analogous Hamiltonian mimics that of a charged particle in an electromagnetic field where the generated beams carry opposite pseudo-charge. Although in general, Hamiltonian is non-Hermitian, it shows $\mathcal{PT}$-symmetric behaviour and the eigenvalues of Hamiltonian are real only for a negative value of nonlinear refractive index (n_2). Hence, I chose *toluene* as the nonlinear medium which shows $n_2 < 0$ at high repetition rate of nanosecond pulsed laser at $532\ nm$ wavelength. The synthetic fields are solely dependent upon pump beam characteristics and it enables us to control them all-optically. A transversely symmetric (topologically trivial) Gaussian pump beam profile would generate only an electric field that leads to symmetric splitting of the beams, creating a Hollow Gaussian Beam. This splitting creates an all-optical analogous Stern-Gerlach effect in $\chi^{(3)}$ led process. Then, an Elliptic Gaussian beam (topologically non-trivial) is generated through incorporating asymmetry in the trans-

verse profile by employing a cylindrical lens. It resulted in shifting the two beams in two opposite directions which resembles an optical analogue of spin Hall Effect. The pseudo-spins acquire an exact amount of opposite Berry phase which has been verified through experimentally acquired interference fringe pattern.

List of Figures

List of Tables

Chapter 1

Introduction

Over the centuries, the field of Optics has flourished with contributions from numerous researchers. The phenomena like interference and diffraction are well explained by the wave nature of light with a coherent source. But there was a shortage of coherent sources of light until 1960 when Theodore Maiman developed the first LASER (Light Amplification by Stimulated Emission of Radiation) [1] utilizing the concept of stimulated emission. When a beam of light interacts with an excited atom, it emits light of the same frequency as the incident one and this process is called stimulated emission of light. Amplification is done through creating optimal feedback from the generated light. Since the invention of LASER, it has revolutionized the field of research in optics and attracted many applications in agriculture [2], defence [3], medicine [4], security [5], high precision manufacturing [6] etc. It also created a path to explore the area of nonlinear optics that was hindered due to unavailability of high power coherent source. But, nonlinearity was realized way before the invention of LASER when John Kerr in 1875 showed that the refractive index of a liquid changes when applied to a DC electric field and the amount of change is proportional to square of the electric field. This effect is known as Kerr effect [7, 8]. After invention of LASER, optical counterpart is observed in both solid and liquid and is termed optical Kerr effect. This happens due to presence of third order nonlinear susceptibility ($\chi^{(3)}$) of the medium. The $\chi^{(3)}$ also contributes to self action effect where a collimated beam either gets focused [9] or diverged depending upon the sign of $\chi^{(3)}$ of the medium. I will delve deeper into this topic, but from a different perspective.

Over the past few years, the concept of synthetic electric and magnetic field has emerged in different areas of photonics [10]. Starting from ultracold atomic medium [11] to topological photonic system [12, 13], the concept now emerges in non-Hermitian photonics with $\mathcal{PT}$ symmetry [14, 15], non-abelian photonics [16], transformation optics [17], etc. The dynamics of the system are equivalent to a charged particle in an electromagnetic (EM) field under certain approximations. Different modes in a coupled waveguide system, forward and backward propagating beam in a periodic structure like photonic crystal, behave like a pseudo-charged particle under the application of EM fields and the fields depend upon properties of interacting medium and light beam. This theoretical modelling has enabled us to bring all the systems under the umbrella of a single theoretical framework.

In this thesis, I will investigate how self action effect due to third order nonlinearity would mimic the charged particle dynamics. In Chapter 2, I will first formulate the theoretical model of how the interacting beams in $\chi^{(3)}$ nonlinearity led process follow nonlinear Schrödinger equation [18]. Next, through rigorous mathematical calculation, I will derive the existence of synthetic electromagnetic fields for third order nonlinearity. In Chapter 3, I will briefly study the difference between Hermitian and non-Hermitian systems and then how parity-time ($\mathcal{PT}$) symmetry in a non-Hermitian system impacts its dynamics and why it has been studied extensively in optics. For two subsequent chapters, two specific cases will be studied where the synthetic fields are completely controlled by pump beam topology and how two eminent phenomena are mimicked in optical domain. In chapter 6, I will summarize my thesis work and will discuss the possible future outcomes.

References

[1] Theodore. H Maiman. Stimulated optical radiation in ruby. *Nature*, 187(4736):493–494, Aug 1960.

[2] Mohammad Nadimi, Da-Wen Sun, and Jitendra Paliwal. Recent applications of novel laser techniques for enhancing agricultural production. *Laser Physics*, 31(5):053001, mar 2021.

[3] Valerie Coffey. High-energy lasers: New advances in defense applications. *Opt. Photon. News*, 25(10):28–35, Oct 2014.

[4] Qian Peng, Asta Juzeniene, Jiyao Chen, Lars O Svaasand, Trond Warloe, Karl-Erik Giercksky, and Johan Moan. Lasers in medicine. *Reports on Progress in Physics*, 71(5):056701, apr 2008.

[5] Sujan Banerjee, Priyanka Dutta, Sudip Kr Bid, Debabrata Sarkhel, and Kailash Bauri. Low-cost laser security system with intrusion detection and alert mechanism. *International Journal of Current Research and Techniques*, 14(4):50241–50245, November 2024.

[6] Qimeng Liu, Jie Liu, Zhe Ming, Bo Cui, and Jian Wang. Research progress on laser-assisted precision machining technology. *Micromachines (Basel)*, 16(2), January 2025.

[7] John Kerr LL.D. Xl. a new relation between electricity and light: Dielectrified media birefringent. *The London, Edinburgh, and Dublin Philosophical Magazine and Journal of Science*, 50(332):337–348, 1875.

[8] W. Kaiser and C. G. B. Garrett. Two-Photon Excitation in CaF_2: Eu^{2+}. *Phys. Rev. Lett.*, 7:229–231, Sep 1961.

[9] P. L. Kelley. Self-focusing of optical beams. *Phys. Rev. Lett.*, 15:1005–1008, Dec 1965.

[10] Wange Song, Yi Yang, Zhiyuan Lin, Xuanyu Liu, Shengjie Wu, Chen Chen, Yongguan Ke, Chaohong Lee, Wei Liu, Shining Zhu, Yuri Kivshar, Tao Li, and Shuang Zhang. Artificial gauge fields in photonics. *Nature Reviews Physics*, 7(11):606–620, Nov 2025.

[11] Y.-J. Lin, R. L. Compton, K. Jiménez-García, J. V. Porto, and I. B. Spielman. Synthetic magnetic fields for ultracold neutral atoms. *Nature*, 462(7273):628–632, Dec 2009.

[12] Ling Lu, John D. Joannopoulos, and Marin Soljačić. Topological photonics. *Nature Photonics*, 8(11):821–829, Nov 2014.

[13] Tomoki Ozawa, Hannah M. Price, Alberto Amo, Nathan Goldman, Mohammad Hafezi, Ling Lu, Mikael C. Rechtsman, David Schuster, Jonathan Simon, Oded Zilberberg, and Iacopo Carusotto. Topological photonics. *Rev. Mod. Phys.*, 91:015006, Mar 2019.

[14] Liang Feng, Ramy El-Ganainy, and Li Ge. Non-hermitian photonics based on parity–time symmetry. *Nature Photonics*, 11(12):752–762, Dec 2017.

[15] Mohammad-Ali Miri and Andrea Alù. Exceptional points in optics and photonics. *Science*, 363(6422):eaar7709, 2019.

[16] Yi Yang, Biao Yang, Guancong Ma, Jensen Li, Shuang Zhang, and C. T. Chan. Non-abelian physics in light and sound. *Science*, 383(6685):eadf9621, 2024.

[17] J. B. Pendry, D. Schurig, and D. R. Smith. Controlling electromagnetic fields. *Science*, 312(5781):1780–1782, 2006.

[18] V. E. Zakharov. Stability of periodic waves of finite amplitude on the surface of a deep fluid. *Journal of Applied Mechanics and Technical Physics*, 9(2):190–194, Mar 1968.

Chapter 2

Theoretical Background

2.1 Wave Equations for propagation of light

Assume that $\vec{E}$ and $\vec{B}$ are the electric field and the magnetic field respectively, associated with the light wave. The four Maxwell's equations for electrodynamics [1, 2] in a source-free medium, *i.e.* medium with no free charge density ($\rho_f = 0$) and no free current density ($J_f = 0$), are

$$\begin{aligned} \vec{\nabla} \cdot \vec{D} &= 0 \\ \vec{\nabla} \cdot \vec{B} &= 0 \\ \vec{\nabla} \times \vec{E} &= -\frac{\partial \vec{B}}{\partial t} \\ \vec{\nabla} \times \vec{H} &= \frac{\partial \vec{D}}{\partial t} \end{aligned} \tag{2.1}$$

Assuming the medium to be non-magnetic, the magnetic field ($\vec{B}$) and magnetic induction ($\vec{H}$) are related as $\vec{B} = \mu_0 \vec{H}$ where μ_0 is the permeability of vacuum. The connection between electric displacement vector ($\vec{D}$) and electric field ($\vec{E}$) is $\vec{D} = \epsilon_0 \vec{E} + \vec{P}$, where ϵ_0 is the permittivity of the free space and $\vec{P}$ is called polarization [3]. We perform curl operation of the third equation of Eq. (2.1) to get the wave equation satisfied by $\vec{E}$.

$$\begin{aligned} \vec{\nabla} \times (\vec{\nabla} \times \vec{E}) &= -\frac{\partial}{\partial t}(\vec{\nabla} \times \vec{B}) \\ \Longrightarrow \vec{\nabla}(\vec{\nabla} \cdot \vec{E}) - \nabla^2 \vec{E} &= -\mu_0 \frac{\partial^2 \vec{D}}{\partial t^2} \end{aligned} \tag{2.2}$$

Incorporating the expression of $\vec{D}$ and using $c = \frac{1}{\sqrt{\mu_0 \epsilon_0}}$, Eq. (2.2) takes the form as

$$\nabla^2 \vec{E} - \frac{1}{c^2} \frac{\partial^2 \vec{E}}{\partial t^2} = \frac{1}{\epsilon_0 c^2} \frac{\partial^2 \vec{P}}{\partial t^2} \tag{2.3}$$

The term $\vec{\nabla}(\vec{\nabla} \cdot \vec{E})$ directly vanishes for beams with a plane wavefront and we can safely neglect the contribution from this term in other scenarios. In vacuum, right hand side of Eq. (2.3) becomes zero but for any medium, it is an inhomogeneous equation with non-zero polarization ($\vec{P}$) contribution. We will deep dive into the polarization context in the following section.

2.2 Linear and Nonlinear Polarization

When an electric field ($\vec{E}$) is applied in a medium, its positive and negative centres of charge are shifted from each other, creating a dipole moment ($\vec{p}$) in the medium. This dipole moment per unit volume (dipole moment density) is defined as Polarization ($\vec{P}$) [4] i.e. $\vec{P} = \frac{d\vec{p}}{dV}$. The larger the applied electric field, greater the separation and hence greater the polarization. So, polarization directly depends upon the applied electric field [see Fig. 2.1]. Mathematically speaking

$$P_i = \epsilon_0 \chi_{ij}^{(1)} E_j + \epsilon_0 \chi_{ijk}^{(2)} E_j E_k + \epsilon_0 \chi_{ijkl}^{(3)} E_j E_k E_l + \cdots \tag{2.4}$$

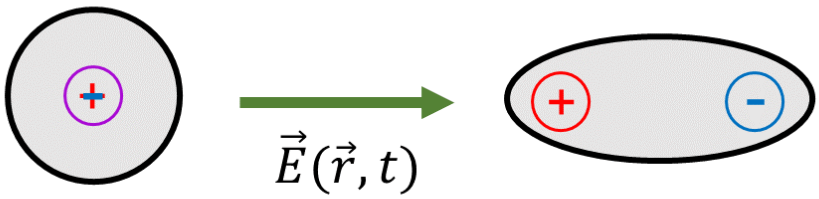

Figure 2.1: Schematic representation of charge separation created by the application of the electric field

Here, the dummy indices ($i, j, ...$) are used to represent the crystallographic axis and χ defines the susceptibility of the medium. We assume the susceptibilities to be dispersionless

for our entire thesis. Equation (2.4) explains that polarization along a particular axis depends upon electric field at all other axes.

$\chi^{(1)} \rightarrow$ Linear susceptibility of medium

$\chi^{(2)} \rightarrow$ Second order nonlinear susceptibility of medium

$\chi^{(3)} \rightarrow$ Third order nonlinear susceptibility of medium

The polarization ($\vec{P}$) in Eq. (2.3) includes both linear and nonlinear parts. It is often convenient to split polarization into its linear and nonlinear parts as $\vec{P} = \vec{P}^{(1)} + \vec{P}^{NL}$ and subsequently we have $\vec{D} = \epsilon_0\vec{E} + \vec{P}^{(1)} + \vec{P}^{NL} = \epsilon_0\epsilon_e\vec{E} + \vec{P}^{NL}$ ($\epsilon_e \rightarrow$ dielectric constant). After substituting the above expressions in Eq. (2.3), it modifies to

$$\nabla^2\vec{E} - \frac{\epsilon_e}{c^2}\frac{\partial^2\vec{E}}{\partial t^2} = \frac{1}{\epsilon_0 c^2}\frac{\partial^2\vec{P}^{NL}}{\partial t^2} \tag{2.5}$$

Now, only the nonlinear contribution remains on the right hand side. It is often convenient to express the $\vec{E}$ in terms of its amplitude and phase. For a monochromatic wave of frequency ω propagating in the z direction will effectively have a unidirectional wavevector. So, it is safe to assume $\vec{k}\cdot\vec{r} \approx k_z z \equiv kz$. Hence, the electric field is with amplitude A is described as

$$E(\vec{r},t) = A(\vec{r})e^{i(kz-\omega t)} \; + \; c.c \tag{2.6}$$

where $c.c$ is meant for complex conjugate. As the beam is propagating in z direction, we separate the longitudinal component (z) and transverse component (x and y) in the Laplacian operator in Eq. (2.5). Incorporating the expression given in Eq. (2.6), left hand side of Eq. (2.5) takes a simpler form as

$$\left(\frac{\partial^2}{\partial x^2}+\frac{\partial^2}{\partial y^2}\right)Ae^{i(kz-\omega t)}+\frac{\partial^2}{\partial z^2}\left(Ae^{i(kz-\omega t)}\right)-\frac{\epsilon_e}{c^2}\frac{\partial^2}{\partial t^2}\left(Ae^{i(kz-\omega t)}\right)$$

$$=\nabla_T^2\left(Ae^{i(kz-\omega t)}\right)+\left(\frac{\partial^2 A}{\partial z^2}\,e^{i(kz-\omega t)}+\frac{\partial A}{\partial z}2ik\,e^{i(kz-\omega t)}-k^2Ae^{i(kz-\omega t)}\right)-\frac{\epsilon_e}{c^2}(-\omega^2)Ae^{i(kz-\omega t)}$$

$$=\nabla_T^2\left(Ae^{i(kz-\omega t)}\right)+\left(\frac{\partial^2 A}{\partial z^2}+2ik\frac{\partial A}{\partial z}\right)e^{i(kz-\omega t)}+\left(\frac{\epsilon_e\omega^2}{c^2}-k^2\right)Ae^{i(kz-\omega t)} \tag{2.7}$$

According to prior knowledge, $k=\frac{n\omega}{c}=\frac{\omega}{c}\sqrt{\epsilon_e}$ and this relation vanishes the last term in Eq. (2.7). Importantly, nonlinear polarization (P^{NL}) will only sustain such combination from E that would have an identical temporal frequency of the single beam i.e. ω. Hence, the differentiation with respect to time of the electric fields would result in a factor of $-\omega^2$. In this situation, only the temporal phase part could be omitted from Eq. (2.5) and is given below

$$\left(\nabla_T^2 A\right)e^{ikz}+\left(\frac{\partial^2 A}{\partial z^2}+2ik\frac{\partial A}{\partial z}\right)e^{ikz}=-\frac{\omega^2}{\epsilon_0 c^2}P^{NL}$$

$$\Rightarrow \nabla_T^2 A+\frac{\partial^2 A}{\partial z^2}+2ik\frac{\partial A}{\partial z}=-\frac{\omega^2}{\epsilon_0 c^2}P^{NL}\,e^{-ikz} \tag{2.8}$$

$$\Rightarrow \nabla_T^2 A+\frac{\partial^2 A}{\partial z^2}+2ik\frac{\partial A}{\partial z}=-\frac{\omega^2}{\epsilon_0 c^2}\widetilde{P}^{NL}\,e^{i\Delta kz}$$

Here, Δk is the difference between the wavevectors of the interacting beams and is termed as phase mismatch [5]. $\widetilde{P}^{NL}$ contains only the corresponding amplitude combination of interacting beams which is different for different nonlinear processes. As the beam is forward propagating in the medium, it is safe to use a very well known assumption in optics that is called the slowly varying amplitude approximation (SVAA) [6, 7]. It says the

amplitude of the propagating electric field varies very slowly over one wavelength of light in the propagation direction. In a mathematical fashion $\left|\frac{\partial^2 A}{\partial z^2}\right| \ll \left|k\frac{\partial A}{\partial z}\right|$. Hence, we safely remove one term from the partial differential equation (PDE) in (2.8).

$$\nabla_T^2 A + 2ik\frac{\partial A}{\partial z} = -\frac{\omega^2}{\epsilon_0 c^2}\widetilde{P}^{NL}\, e^{i\Delta kz} \tag{2.9}$$

This is the updated form of the wave equation in case of an isotropic medium. If the interacting light beam has a planar wavefront, then Laplacian contribution will be zero and wave equation will be even more simpler to solve. But for a dispersive medium, refractive index varies with frequency $n(\omega_l) = \sqrt{\epsilon_e(\omega_l)}$, so the electric field component for different frequencies will be different and they have to be studied separately. Both Eq. (2.5) and (2.9) are valid for each frequency separately and we can write

$$\nabla_T^2 A_l + 2ik\frac{\partial A_l}{\partial z} = -\frac{\omega^2}{\epsilon_0 c^2}\widetilde{P}_l^{NL}\, e^{i\Delta kz} \tag{2.10}$$

Equation (2.10) is our fundamental wave equation for electric field that will be extensively used in the subsequent chapters. We drop the subscript l here onward for simplicity. Depending upon the nonlinear susceptibility, corresponding nonlinear polarization would only be used in the above PDE.

Although in polarization, theoretically all susceptibilities are present but only a few χ are studied extensively due to several constraints like availability of high power laser, crystallographic arrangements, etc. In the next section, we will investigate the interaction that appear due to $\chi^{(3)}$ nonlinearity.

2.3 Third-order nonlinear optical phenomena

For centrosymmetric (presence of center of inversion symmetry) media, all even order of nonlinear polarization will be absent. So, the lowest nonlinear interaction will be governed

by third-order nonlinearity ($\chi^{(3)}$). $\chi^{(3)}$ is responsible for phenomena like self phase modulation (SPM) [8, 9, 10], third harmonic generation [11, 12, 13] and self action effect [14, 15] involving a single beam and phenomena like cross phase modulation (XPM) [16, 17] and four wave mixing (FWM) [18, 19, 20] involving multiple beams.

We start with a single light beam of frequency ω propagating through a nonlinear medium and the nonlinear polarization due to $\chi^{(3)}$ for the beam is

$$P^{NL}(\omega) = 3\epsilon_0\chi^{(3)}E(\omega)(E(\omega))^*E(\omega) = 3\epsilon_0\chi^{(3)}|E(\omega)|^2E(\omega) \tag{2.11}$$

The total polarization would then be

$$P = P^{(1)} + P^{(NL)} = \epsilon_0\chi^{(1)}E + 3\epsilon_0\chi^{(3)}|E|^2E \equiv \epsilon_0\chi^{(eff)}E \tag{2.12}$$

where $\chi^{(eff)} = \chi^{(1)} + \chi^{(3)}|E|^2$ is the effective susceptibility of the medium. The total refractive index (n) of any medium can be expressed in terms of its susceptibility (χ) so in current scenario, $n = \sqrt{1+\chi^{(eff)}}$. Incorporating linear refractive index as $n_0^2 = 1+\chi^{(1)}$, and comparing expression for total refractive index $n = n_0 + n_2 I$ (I is the intensity of light) with the previous one, we can define nonlinear refractive index n_2 of the medium,

$$n_2 = \frac{3\chi^{(3)}}{4n_0n_0'\epsilon_0 c} \tag{2.13}$$

Substituting the values of the universal constants (ϵ_0 and c) in Eq. (2.13), it simplifies for SI unit as

$$n_2\ (m^2/W) = \frac{283}{n_0n_0'}\chi^{(3)}\ (m^2/V^2) \tag{2.14}$$

Incorporating the nonlinear polarization according to Eq. (2.11), the wave equation as shown in Eq. (2.10) modifies to

$$\begin{aligned} \nabla_T^2 A + 2ik\frac{\partial A}{\partial z} &= -\frac{\omega^2}{\epsilon_0 c^2}3\epsilon_0\chi^{(3)}|A|^2A \\ \implies i\frac{\partial A}{\partial z} &= -\frac{1}{2k}\nabla_T^2 A - \frac{3\omega^2\chi^{(3)}}{2kc^2}|A|^2A \end{aligned} \tag{2.15}$$

Equation (2.15) is similar in form to the Schrödinger equation in quantum mechanics but with an additional term that contains the $\chi^{(3)}$ led nonlinearity. Time (t) coordinate in quantum mechanics is replaced by z coordinate in the optical domain. Hence, Eq. (2.15) is known as the nonlinear Schrödinger equation (NLSE) [21, 22, 23]. NLSE acts as a universal formalism for waves propagating through nonlinear media, describing how waves modulate their own shape. In the next section, we will investigate one prominent wave modulation phenomenon, termed self action effect.

2.4 Self action effect

A simple look at equation (2.13) reveals that n_2 is directly proportional to $\chi^{(3)}$. So, the nonlinear refractive index could be positive ($n_2 > 0$) as well as negative ($n_2 < 0$) as $\chi^{(3)}$ can have both signs. Clearly, the dynamics would be different for two opposite signs of n_2 according to Eq. (2.15).

A sufficiently high intensity of light could modulate the total refractive index (n) of medium through nonlinear refractive index (n_2) and it gives rise to a phenomenon called self-action effect. These self-induced effects are crucial in shaping pulse dynamics in optical fibers [24], generating supercontinuum spectra [25], and enabling soliton formation [26] in nonlinear waveguides. In this effect, a beam of light modifies its own propagation by means of the nonlinear response of a medium. For $n_2 > 0$, an intense beam of light modifies the optical properties of a medium in such a manner that the beam tends to get focused within the medium and this is known as self-focusing of light [14, 27]. As a result, the laser beam induces a refractive index variation within the material with a larger refractive index at the center of the beam than at its periphery. The medium thus acts as a convex lens. For $n_2 < 0$, refractive index variation is opposite to that of $n_2 > 0$, hence, the beam tends to diverge during propagation and the medium acts as a concave lens.

Due to this non-uniformity created in the medium, the beam wavefront undergoes distortion and as a result, the beam can break up into multiple other beams. This process is known as *filamentation* [28, 29, 30, 31]. Beam breakup occurs as a consequence of the amplification of forward 'four-wave mixing' (FWM) process of the distortions present in the laser wavefront. Hence, through filamentation, a single beam can generate multiple beams that are amplified by a FWM process. Although beam break-up typically occurs for a random transverse profile, beams with regular transverse pattern can participate as well [32, 33, 34] and they could undergo the [35] filamentation process.

2.5 Mathematical Description of Synthetic Fields

We consider a strong light beam called pump ($|\psi_p\rangle$) at frequency ω_p propagating along z-direction in a medium exhibiting $\chi^{(3)}$ optical nonlinearity. In the present context, we assume that the pump beam generates two co-propagating, co-polarized weak ansatz fluctuations $|\psi_\pm\rangle$. We closely follow the mathematical description as originally described by Bespalov and Talanov [36] for the beam breakup. It is convenient to express the electric field amplitude as the sum of three wave components as

$$A(\vec{r}) = a_p(\vec{r}) + a_+(\vec{r}) + a_-(\vec{r}) \tag{2.16}$$

where a_p is the amplitude of the original pump beam and a_+ and a_- are the generated ansatz fields' amplitudes. Schematically, the pump and generated fields are represented in Fig. 2.2. In the paraxial approximation, the evolution of slowly-varying pump envelope (a_p) is governed by Eq. (2.15) [37]

$$i\frac{\partial a_p}{\partial z} = -\frac{1}{2k_p}\nabla_T^2 a_p - \frac{3\chi^{(3)}\omega_p^2}{2k_p c^2}|a_p|^2 a_p \tag{2.17}$$

where $\vec{\nabla}_T \equiv \hat{x}\frac{\partial}{\partial x} + \hat{y}\frac{\partial}{\partial y}$ and $|\psi_p(\vec{r})\rangle = \frac{1}{2}[a_p(\vec{r})e^{i(\omega_p t - k_p z)} + c.c]$ (with $\vec{r} = \vec{\rho} + \vec{z}$ and $\rho = \sqrt{x^2 + y^2}$) represents the pump mode field and $k_p = \frac{\omega_p}{c} n_p$ where $n_p \equiv n(\omega_p)$. Equation (2.17), in general, resembles the Gross-Pitaevskii (GP) equation (with zero external potential) describing s-wave interactions in a weakly interacting BEC.

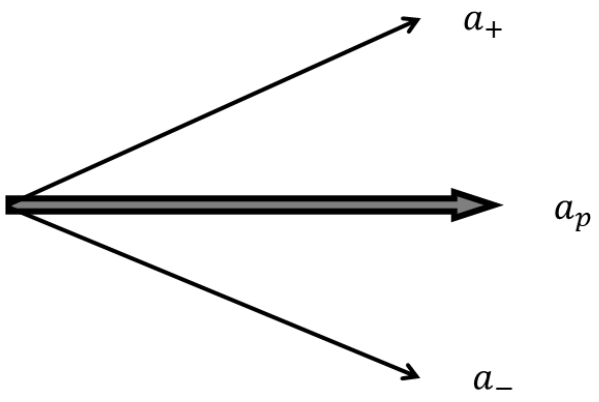

Figure 2.2: Beam breakup occurs due to growth of spatial modes from strong central component a_p

The ansatz fields are expressed as $|\psi_\pm(\vec{r})\rangle = \frac{1}{2}\left[a_\pm(\vec{r})e^{i(\omega_\pm t - k_\pm z)} + c.c.\right]$ with $k_\pm = \frac{\omega_\pm}{c} n_\pm$. The chosen ansatz fields ($|\psi_+\rangle$ and $|\psi_-\rangle$) are distinguishable from their spatial frequency spectrum and have physical resemblance to the coherent excitations appearing in Bogoliubov theory of matter-waves. We assume that ansatz fields carry same frequency ($\omega_+ = \omega_- = \omega_p$) as the pump beam and remain co-propagating throughout the interaction. So, their wave vector are nearly same as that of the pump beam, i.e. $k_+ \approx k_- \approx k_p$. The nonlinear polarization for the beams a_+ and a_- are

$$\begin{aligned} P_+^{NL} &= 3\epsilon_0\chi^{(3)}(2|a_p|^2 a_+ + a_p^2 a_-^*) \\ P_-^{NL} &= 3\epsilon_0\chi^{(3)}(2|a_p|^2 a_- + a_p^2 a_+^*) \end{aligned} \tag{2.18}$$

The first term in RHS of Eq. (2.18) is the self phase modulation term and the second term signifies the FWM term for a_+ and a_-, respectively. It is important to note that nonlinear polarization is coupled for the ansatz fields, hence the wave equations will also be coupled to each other. At this point, we consider that pump beam amplitude a_p stays nearly unchanged i.e. $a_p \approx const.$ This is defined as low-pump depletion approximation. Also, the pump acquires a dynamic phase during propagation [37]. In that circumstance, the coupled wave equations for a_+ and a_- could be expressed in a matrix form,

$$i\frac{\partial}{\partial z}\left|\Psi\right\rangle = \begin{pmatrix} \frac{\vec{p}_T^2}{2k_p} - \frac{6\chi^{(3)}\omega_p^2}{2k_pc^2}|a_p|^2 & -\frac{3\chi^{(3)}\omega_p^2}{2k_pc^2}a_p^2 e^{2i\Phi} \\ \frac{3\chi^{(3)}\omega_p^2}{2k_pc^2}a_p^{*2}e^{-2i\Phi} & -\frac{\vec{p}_T^2}{2k_p} + \frac{6\chi^{(3)}\omega_p^2}{2k_pc^2}|a_p|^2 \end{pmatrix}\left|\Psi\right\rangle \tag{2.19}$$

where $\vec{p}_T = -i\vec{\nabla}_T$ is the equivalent linear momentum operator and $\left|\Psi\right\rangle = (a_+ \;\; a_-^*)^T$ is the two-component spinor constructed using basis state ($\left|\psi_\pm\right\rangle$) envelopes. Equation (2.19) is an optical analogue of *Bogoliubov de-Gennes* (BdG) equations describing transport of a photon ensemble [38]. The dynamic phase (Φ) acquired by the pump beam due to nonlinear interaction is given by,

$$\Phi = \frac{\omega_p}{c}\int_0^z \left[n_p + n_2 I_p(\vec{\rho}, z')\right]\, dz' \tag{2.20}$$

where $I_p = 2n_p\epsilon_0 c|a_p|^2$ is incident pump intensity, $n_2 = \frac{3\chi^{(3)}}{4\epsilon_0 c n_p^2}$ is the nonlinear refractive index and z is the interaction length. Equation (2.19) could be expressed in a compact form as,

$$i\frac{\partial}{\partial z}\left|\Psi\right\rangle = \frac{\vec{p}_T^2}{2k_p}\sigma_z\left|\Psi\right\rangle - \frac{3\chi^{(3)}\omega_p^2}{2k_pc^2}\begin{pmatrix} 2|a_p|^2 & a_p^2 e^{2i\Phi} \\ -a_p^{*2}e^{-2i\Phi} & -2|a_p|^2 \end{pmatrix}\left|\Psi\right\rangle \tag{2.21}$$

where we have defined $\sigma_z = \begin{pmatrix} 1 & 0 \\ 0 & -1 \end{pmatrix}$. The off-diagonal terms of Eq. (2.19) result in dynamical (nonlinear) coupling between $|\psi_+\rangle$ and $|\psi_-\rangle$. It is worthwhile to note that the dynamics depicted by Eq. (2.19) depend on z. In order to eliminate the z-dependence, we shift to a rotated frame using a unitary transformation given by $U(\vec{r}) = \text{diag}\ (e^{i\Phi}, e^{-i\Phi})$ which leads to transformed eigenstate $|\Psi'\rangle = U^\dagger(\vec{r})\,|\Psi\rangle$. A more compact and meaningful representation is obtained when $U^\dagger$ is multiplied with Eq. (2.21) from left and use $|\Psi\rangle = U(\vec{r})\,|\Psi'\rangle$

$$\begin{aligned} U^\dagger(\vec{r})\left[i\frac{\partial}{\partial z}(U(\vec{r})\,|\Psi'\rangle)\right] &= U^\dagger(\vec{r})\frac{\vec{p}_T^{\,2}}{2k_p}\sigma_z U(\vec{r})\,|\Psi'\rangle \\ &- \frac{3\chi^{(3)}\omega_p^2}{2k_p c^2}U^\dagger(\vec{r})\begin{pmatrix} 2|a_p|^2 & a_p^2 e^{2i\Phi} \\ -a_p^{*2}e^{-2i\Phi} & -2|a_p|^2 \end{pmatrix} U(\vec{r})\,|\Psi'\rangle \end{aligned} \tag{2.22}$$

which could be simplified by noting,

$$U^\dagger\left[i\frac{\partial}{\partial z}(U\,|\Psi'\rangle)\right] = U^\dagger\left[i\frac{\partial U}{\partial z}\,|\Psi'\rangle + iU\frac{\partial}{\partial z}\,|\Psi'\rangle\right] = i\left(U^\dagger\frac{\partial U}{\partial z}\right)|\Psi'\rangle + i\frac{\partial}{\partial z}\,|\Psi'\rangle \tag{2.23}$$

The first and second term of Eq. (2.22) are explicitly calculated below

$$U^\dagger\vec{p}_T U = \vec{p}_T - iU^\dagger\vec{\nabla}_T U \tag{2.24}$$

$$\begin{pmatrix} e^{-i\Phi} & 0 \\ 0 & e^{i\Phi} \end{pmatrix}\begin{pmatrix} 2|a_p|^2 & a_p^2 e^{2i\Phi} \\ -a_p^{*2}e^{-2i\Phi} & -2|a_p|^2 \end{pmatrix}\begin{pmatrix} e^{i\Phi} & 0 \\ 0 & e^{-i\Phi} \end{pmatrix} = \begin{pmatrix} 2|a_p|^2 & a_p^2 \\ -a_p^{*2} & -2|a_p|^2 \end{pmatrix} \tag{2.25}$$

Therefore, Equation (2.22) simplifies to,

$$i\frac{\partial}{\partial z}|\Psi'\rangle = \frac{(\vec{p}_T - iU^\dagger\vec{\nabla}_T U)^2}{2k_p}\sigma_z|\Psi'\rangle - \frac{3\chi^{(3)}\omega_p^2}{2k_pc^2}\begin{pmatrix}2|a_p|^2 & a_p^2\\ -a_p^{*2} & -2|a_p|^2\end{pmatrix}|\Psi'\rangle - i\left(U^\dagger\frac{\partial U}{\partial z}\right)|\Psi'\rangle \tag{2.26}$$

It is worth noting that, as per the definition for U, we obtain,

$$iU^\dagger\frac{\partial U}{\partial z} = -\frac{\partial\Phi}{\partial z}\sigma_z = -\frac{\omega_p}{c}n_p\sigma_z - \frac{\omega_p}{c}n_2I_p\sigma_z = -k_p\sigma_z - \frac{3\chi^{(3)}\omega_p^2}{2k_pc^2}|a_p|^2\sigma_z \tag{2.27}$$

Consequently, the Equation (2.26) takes a compact form given by,

$$i\frac{\partial}{\partial z}|\Psi'\rangle = \frac{(\vec{p}_T - iU^\dagger\vec{\nabla}_T U)^2}{2k_p}\sigma_z|\Psi'\rangle - \frac{3\chi^{(3)}\omega_p^2}{2k_pc^2}\begin{pmatrix}|a_p|^2 & a_p^2\\ -a_p^{*2} & -|a_p|^2\end{pmatrix}|\Psi'\rangle + k_p\sigma_z|\Psi'\rangle$$

$$= \frac{(\vec{p}_T - iU^\dagger\vec{\nabla}_T U)^2}{2k_p}\sigma_z|\Psi'\rangle - \frac{3\chi^{(3)}\omega_p^2}{2k_pc^2}\begin{pmatrix}|\mathbb{A}_p|^2 & |\mathbb{A}_p|^2e^{-2i\theta}\\ -|\mathbb{A}_p|^2e^{2i\theta} & -|\mathbb{A}_p|^2\end{pmatrix}|\Psi'\rangle + k_p\sigma_z|\Psi'\rangle$$

$$= \left[\frac{(\vec{p}_T - q_e\vec{\mathcal{A}})^2}{2k_p}\sigma_z - \Omega\begin{pmatrix}1 & e^{2i\theta}\\ -e^{-2i\theta} & -1\end{pmatrix} + k_p\sigma_z\right]|\Psi'\rangle$$

$$i\frac{\partial}{\partial z}|\Psi'\rangle = \left[\frac{(\vec{p}_T - q_e\vec{\mathcal{A}})^2}{2M} + q_e(-\vec{\sigma}\cdot\vec{\mathcal{M}}) + k_p\sigma_z\right]|\Psi'\rangle \tag{2.28}$$

where $\vec{\mathcal{A}} = \frac{i}{q_e}U^\dagger\vec{\nabla}_T U = -\frac{1}{q_e}(\vec{\nabla}_T\Phi)\sigma_z$ is the synthetic magnetic vector potential, $\vec{\mathcal{M}} = \vec{\mathcal{M}}_T + \mathcal{M}_z\hat{z} = \frac{\Omega}{q_e}[\sin(2\theta)e^{-i(2m+1)\pi/2}\hat{x} + \cos(2\theta)e^{i(2m+1)\pi/2}\hat{y} + \hat{z}]$ $(m = \pm1, \pm2, \cdots)$

is synthetic magnetization. $\Omega = \frac{\omega_p}{c} n_2 I_p(\vec{\rho})$ is the coupling term involving nonlinearity ($\chi^{(3)}$) and pump intensity I_p. For our convenience, pump beam amplitude is rewritten as $a_p(\vec{\rho}) = \mathbb{A}_p(\vec{\rho}) e^{-i\theta(\vec{\rho})}$ where both $\mathbb{A}_p$ and θ are real and θ is the initial phase of pump beam. q_e is an emergent charge introduced artificially for developing an equivalent electrodynamic model. $\vec{\sigma} = (\sigma_x, \sigma_y, \sigma_z)$ is the triad of Pauli's spin matrices and an equivalent linear mass operator is defined as $M^{-1} = \frac{1}{k_p}\sigma_z$.

Equation (2.28) resembles Pauli's equation [39] for describing the spatial evolution dynamics of a massive spin-$\frac{1}{2}$ particle with unit magnetic moment ($|\mu| = 1$) in a magnetizing field ($\vec{\mathcal{M}}$) where time-coordinate (t) is replaced by z-coordinate. It is worth noting that the pump beam topology governs the dynamics through the gauge fields, namely, pseudo-vector potential $\vec{\mathcal{A}}$ and pseudo-scalar potential $\mathcal{V} = -\vec{\sigma} \cdot \vec{\mathcal{M}}$ [38]. The spatial (z) evolution of spinor ($|\Psi'\rangle$) is determined from the steady-state solution of the following Hamiltonian

$$\hat{H} = \frac{(\vec{p}_T - q_e \vec{\mathcal{A}})^2}{2M} + q_e \mathcal{V} \tag{2.29}$$

In the emergent charge picture, the particles in two pseudo-spin basis ($|\psi_\pm\rangle$) are assumed to inherit charges $\pm q_e$ but without any spin [40]. The sign of charges are dictated by the orientation of decoupled basis states $|\psi_\pm\rangle$ with respect to the local magnetization ($\vec{\mathcal{M}}$) direction. Therefore, the dynamics of two-level (spin-1/2) system could be ascertained through an electrodynamic interaction of oppositely charged states with emergent electric ($\vec{\mathcal{E}}$) and magnetic field ($\vec{\mathcal{B}}$) which is given by [41, 40],

$$\vec{\mathcal{E}} = -\vec{\nabla}_T \mathcal{V} - \frac{\partial \vec{\mathcal{A}}}{\partial z} \tag{2.30}$$

$$\vec{\mathcal{B}} = \vec{\nabla}_T \times \vec{\mathcal{A}} \tag{2.31}$$

The existence of $\vec{\mathcal{E}}$ and $\vec{\mathcal{B}}$ would manifest through an equal but opposite transverse (in x or y) directed synthetic Lorentz force $\vec{\mathcal{F}}_{\pm} = q_{e_{\pm}}(\vec{\mathcal{E}} + \vec{v} \times \vec{\mathcal{B}})$ where the emergent velocity $\vec{v} = M^{-1}\vec{p}_T$ that would act on two oppositely *charged* states ($|q_{e_{\pm}}\rangle$). It is evident that $\vec{\mathcal{E}}$ and $\vec{\mathcal{B}}$ both depend on $\vec{\mathcal{M}}$ which in turn depends on pump beam topology. Hence, the fields are called *all-optically* controllable synthetic fields. The pump beam topology was tuned to modify $\vec{\mathcal{E}}$ and $\vec{\mathcal{B}}$ such that we could create an analogous Stern-Gerlach (SG) effect and Topological Hall effect in $\chi^{(3)}$ mediated interaction which would be studied in detail in the subsequent chapters.

References

[1] James Clerk Maxwell. A dynamical theory of the electromagnetic field. *Philosophical Transactions of the Royal Society of London*, n/a(155):459–512, Dec 1865.

[2] J.C. Maxwell. On physical lines of force. *Philosophical Magazine*, 90(sup1):11–23, Feb 2010.

[3] Joseph Larmor. A dynamical theory of the electric and luminiferous medium. part ii; theory of electrons. *Proceedings of the Royal Society of London*, 58(347-352):222–228, Dec 1895.

[4] H. A. Lorentz. The fundamental equations for electromagnetic phenomena in ponderable bodies deduced from the theory of electrons. *Koninklijke Nederlandse Akademie van Wetenschappen Proceedings Series B Physical Sciences*, 5:254–266, Jan 1902.

[5] P. D. Maker and R. W. Terhune. Study of optical effects due to an induced polarization third order in the electric field strength. *Phys. Rev.*, 137:A801–A818, Feb 1965.

[6] F. Arecchi and R. Bonifacio. Theory of optical maser amplifiers. *IEEE Journal of Quantum Electronics*, 1(4):169–178, 1965.

[7] Paul N. Butcher and David Cotter. *The Elements of Nonlinear Optics*. Cambridge University Press, Jul 1990.

[8] W. J. Jones and B. P. Stoicheff. Inverse raman spectra: Induced absorption at optical frequencies. *Phys. Rev. Lett.*, 13:657–659, Nov 1964.

[9] N. Bloembergen and P. Lallemand. Complex intensity-dependent index of refraction, frequency broadening of stimulated raman lines, and stimulated rayleigh scattering. *Phys. Rev. Lett.*, 16:81–84, Jan 1966.

[10] Fujio Shimizu. Frequency broadening in liquids by a short light pulse. *Phys. Rev. Lett.*, 19:1097–1100, Nov 1967.

[11] R. W. Terhune, P. D. Maker, and C. M. Savage. Optical harmonic generation in calcite. *Phys. Rev. Lett.*, 8:404–406, May 1962.

[12] F. Kajzar and J. Messier. Third-harmonic generation in liquids. *Phys. Rev. A*, 32:2352–2363, Oct 1985.

[13] Aizitiaili Abulikemu and Muneaki Hase. Highly-efficient third-harmonic generation from ultrapure diamond crystals. *Opt. Mater. Express*, 13(4):916–924, Apr 2023.

[14] P. L. Kelley. Self-focusing of optical beams. *Phys. Rev. Lett.*, 15:1005–1008, Dec 1965.

[15] Jr. Fleck, J. A. and P. L. Kelley. Temporal aspects of the self - focusing of optical beams. *Applied Physics Letters*, 15(10):313–315, Nov 1969.

[16] Guozhen Yang and Y. R. Shen. Spectral broadening of ultrashort pulses in a nonlinear medium. *Opt. Lett.*, 9(11):510–512, Nov 1984.

[17] R. R. Alfano, Q. X. Li, T. Jimbo, J. T. Manassah, and P. P. Ho. Induced spectral broadening of a weak picosecond pulse in glass produced by an intense picosecond pulse. *Opt. Lett.*, 11(10):626–628, Oct 1986.

[18] R. L. Carman, R. Y. Chiao, and P. L. Kelley. Observation of degenerate stimulated four-photon interaction and four-wave parametric amplification. *Phys. Rev. Lett.*, 17:1281–1283, Dec 1966.

[19] R. Stolen. Phase-matched-stimulated four-photon mixing in silica-fiber waveguides. *IEEE Journal of Quantum Electronics*, 11(3):100–103, 1975.

[20] R. Stolen and J. Bjorkholm. Parametric amplification and frequency conversion in optical fibers. *IEEE Journal of Quantum Electronics*, 18(7):1062–1072, 1982.

[21] V. E. Zakharov. Stability of periodic waves of finite amplitude on the surface of a deep fluid. *Journal of Applied Mechanics and Technical Physics*, 9(2):190–194, Mar 1968.

[22] V. E. Zakharov and A. B. Shabat. Exact theory of two-dimensional self-focusing and one-dimensional self-modulation of waves in nonlinear media. *Soviet Journal of Experimental and Theoretical Physics*, 34:62–69, Jan 1972.

[23] Govind P. Agrawal. *Nonlinear Fiber Optics*. Academic Press, 6th edition, 2019.

[24] Federica Cattani, Dan Anderson, Anders Berntson, and Mietek Lisak. Effect of self-phase modulation in chirped-pulse-amplification-like schemes. *J. Opt. Soc. Am. B*, 16(11):1874–1879, Nov 1999.

[25] Alexander M. Heidt. Pulse preserving flat-top supercontinuum generation in all-normal dispersion photonic crystal fibers. *J. Opt. Soc. Am. B*, 27(3):550–559, Mar 2010.

[26] Ilaria Cristiani, Riccardo Tediosi, Luca Tartara, and Vittorio Degiorgio. Dispersive wave generation by solitons in microstructured optical fibers. *Opt. Express*, 12(1):124–135, Jan 2004.

[27] R. Y. Chiao, E. Garmire, and C. H. Townes. Self-trapping of optical beams. *Phys. Rev. Lett.*, 13:479–482, Oct 1964.

[28] A. Braun, G. Korn, X. Liu, D. Du, J. Squier, and G. Mourou. Self-channeling of high-peak-power femtosecond laser pulses in air. *Opt. Lett.*, 20(1):73–75, Jan 1995.

[29] Khan Lim, Magali Durand, Matthieu Baudelet, and Martin Richardson. Transition from linear- to nonlinear-focusing regime in filamentation. *Scientific Reports*, 4(1):7217, Dec 2014.

[30] Eyal Feigenbaum, Jean-Michel G. Di Nicola, and Jeff D. Bude. Revisiting beam filamentation formation conditions in high power lasers. *Opt. Express*, 27(8):10611–10630, Apr 2019.

[31] W. Ettoumi, J. Kasparian, and J.-P. Wolf. Spin-glass model governs laser multiple filamentation. *Phys. Rev. Lett.*, 115:033902, Jul 2015.

[32] Audrius Dubietis, Gintaras Tamošauskas, Gadi Fibich, and Boaz Ilan. Multiple filamentation induced by input-beam ellipticity. *Opt. Lett.*, 29(10):1126–1128, May 2004.

[33] Taylor D. Grow and Alexander L. Gaeta. Dependence of multiple filamentation on beam ellipticity. *Opt. Express*, 13(12):4594–4599, Jun 2005.

[34] L. Bergé, C. Gouédard, J. Schjødt-Eriksen, and H. Ward. Filamentation patterns in kerr media vs. beam shape robustness, nonlinear saturation and polarization states. *Physica D: Nonlinear Phenomena*, 176(3):181–211, 2003.

[35] Ryan S. Bennink, Vincent Wong, Alberto M. Marino, David L. Aronstein, Robert W. Boyd, C. R. Stroud, Svetlana Lukishova, and Daniel J. Gauthier. Honeycomb pattern formation by laser-beam filamentation in atomic sodium vapor. *Phys. Rev. Lett.*, 88:113901, Feb 2002.

[36] V. I. Bespalov and V. I. Talanov. Filamentary Structure of Light Beams in Nonlinear Liquids. *Soviet Journal of Experimental and Theoretical Physics Letters*, 3:471, Jun 1966.

[37] Robert W. Boyd. *Nonlinear Optics*. Academic Press, Inc., 3rd edition, 2008.

[38] N. Westerberg, C. Maitland, D. Faccio, K. Wilson, P. Öhberg, and E. M. Wright. Synthetic magnetism for photon fluids. *Physical Review A*, 94(2):023805, August 2016.

[39] W. Pauli. Zur quantenmechanik des magnetischen elektrons. *Zeitschrift für Physik*, 43(9):601–623, Sep 1927.

[40] Aviv Karnieli, Shai Tsesses, Guy Bartal, and Ady Arie. Emulating spin transport with nonlinear optics, from high-order skyrmions to the topological Hall effect. *Nature communications*, 12(1):1092, 2021.

[41] Karin Everschor-Sitte and Matthias Sitte. Real-space Berry phases: Skyrmion soccer (invited). *Journal of Applied Physics*, 115(17):172602, May 2014.

Chapter 3

Properties of the Hamiltonian

3.1 Hermitian vs Non-Hermitian

In physics, it is important to ascertain the nature of dynamical interaction, in terms of whether the interaction is Hermitian or not [1]. Mathematically, Hermiticity is checked through '*dagger*' operation which is defined as complex conjugation with transpose. When an operator $\hat{R}$ is Hermitian *i.e.* mathematically $\hat{R}^\dagger = \hat{R}$, it possesses some unique properties as

- Eigenvalues of $\hat{R}$ are always real
- Eigenvectors corresponding to different eigenvalues of $\hat{R}$ are orthogonal to each other

In quantum mechanics, Hermitian operators are extremely important, and accordingly, the observables (eigenvalues) are real. Amongst all operators associated with the system under consideration, our concentration will be on the Hamiltonian operator. Eigenvalues of Hamiltonian represent different energy levels and corresponding states of different energy levels are represented by eigenvectors. If Hamiltonian ($\hat{H}$) of a system is Hermitian i.e. $\hat{H}^\dagger = \hat{H}$, that signifies the energy eigenvalues are real and remain stationary. The total energy is conserved in such a system.

On the contrary, most of the physical systems are non-conservative in nature. So, the system becomes non-Hermitian in that scenario. When an operator $\hat{H}$ is non-Hermitian i.e. $\hat{H}^\dagger \neq \hat{H}$, some of its properties that differ from its Hermitian counterpart [2] are

- Eigenvalues of $\hat{H}$ are complex in general

- Left and right eigenvectors are different for a particular eigenvalue
- Eigenvectors of different eigenvalues are no longer orthogonal to each other

Although, the orthogonal relation of eigenvectors doesn't hold here, a similar property called bi-orthogonality of eigenvectors exists in non-Hermitian system. Mathematically, if $|\xi_n\rangle$ is right eigenvector and $\langle\Phi_m|$ represents left eigenvector for two different eigenvalues of $\hat{H}$, then $\langle\Phi_m|\xi_n\rangle = \delta_{mn}$, whereas for Hermitian $\hat{H}$, $\langle\xi_m|\xi_n\rangle = \delta_{mn}$, where δ_{mn} is Kronecker delta function.

Due to the above mentioned properties, non-Hermitian systems did not gain much attention due to their complicated nature. Their analysis gained momentum only after its relation with parity ($\hat{\mathcal{P}}$) and time reversal operator ($\hat{\mathcal{T}}$) was found out [3].

3.2 $\mathcal{PT}$ symmetry and non-Hermiticity

$\hat{\mathcal{P}}$ and $\hat{\mathcal{T}}$ operators are parity and time-reversal operators, respectively. Parity operator $\hat{\mathcal{P}}$ is an operator that flips the space which means $\hat{\mathcal{P}}\ x \rightarrow -x$ [4]. Parity is an involutory operator so $\mathcal{P}^2 = \mathbb{I}$ where, $\mathbb{I}$ is identity operator. Time reversal operator $\hat{\mathcal{T}}$ reverses the time and analytically, $\hat{\mathcal{T}}\ t \rightarrow -t$ [5].

Bender *et. al* has shown that if a non-Hermitian operator $\hat{H}$ commutes with $\hat{\mathcal{P}}\hat{\mathcal{T}}$ operator [2] i.e.

$$[\hat{H}, \hat{\mathcal{P}}\hat{\mathcal{T}}] = 0 \tag{3.1}$$

is called $\hat{\mathcal{P}}\hat{\mathcal{T}}$ symmetric Hamiltonian and it could have real eigenvalues [6, 7, 8, 9, 10]. This property makes non-Hermitian system interesting as real eigenvalues of any operator could be measured. Conversely, when $\hat{H}$ does not commute with $\hat{\mathcal{P}}\hat{\mathcal{T}}$ operator *i.e.* $[\hat{H}, \hat{\mathcal{P}}\hat{\mathcal{T}}] \neq 0$, eigenvalues become complex and hence the system is called a $\hat{\mathcal{P}}\hat{\mathcal{T}}$ broken system. So, parity-time ($\hat{\mathcal{P}}\hat{\mathcal{T}}$) symmetry is an essential property to inspect before further investigation of a non-Hermitian system.

Now, we will look into a fascinating property of non-Hermitian system. For that, we assume the Hamiltonian $\hat{H}$ depends upon a single parameter β that can be varied. As a result, both eigenvalues (e_n) and corresponding eigenvectors ($|\xi_n\rangle$) will also depend on β. With tuning β, values of e_n and angle between $|\xi_n\rangle$ vary as it is not fixed for non-Hermitian case. In this scenario, we might arrive at a situation where for some critical values of β, eigenvalues (e_n) become degenerate and the eigenvectors ($|\xi_n\rangle$) become parallel to each other. This critical point is known as exceptional point (EP) [11, 12, 13, 14, 15] and Hamiltonian $\hat{H}$ becomes defective and cannot be diagonalized. The non-Hermitian degeneracy at this critical point is clearly distinguishable from a regular Hermitian degeneracy [16, 17]. Apart from degeneracy, the EP shows a branch point singularity in nature. Deeply looking into this, it reveals that an EP actually acts as a transition point where on one side $\hat{H}$ is $\hat{\mathcal{P}}\hat{\mathcal{T}}$ symmetric and $\hat{H}$ does not commute with $\hat{\mathcal{P}}\hat{\mathcal{T}}$ on the other side. It demarcates the $\hat{\mathcal{P}}\hat{\mathcal{T}}$ symmetric and $\hat{\mathcal{P}}\hat{\mathcal{T}}$-symmetry broken regime [18]. Additional controlling parameters of system will be beneficial as it would make the EP tunable in the parameter space [19, 20].

Another fascinating property of a non-Hermitian operator is *pseudo-Hermiticity*, which is defined as

$$\hat{H}^{\dagger} = \hat{\eta}^{-1}\hat{H}\hat{\eta} \tag{3.2}$$

where $\hat{\eta}$ is a unitary operator. One of the most important property of pseudo-Hermitian operator is that it possesses real eigenvalue spectrum [21, 22, 23].

From past couple of decades, exploration of different non-Hermitian system is underway [24]. In optical systems, it is easy to introduce and control gain and loss in the medium compared to any other system [25]. Coupled waveguides with loss and gain [26], counter-propagating waves in Bragg gratings [27], coupled ring resonators [28] with loss and gain are among the premier ones where the non-Hermitian properties have been analyzed. From an application perspective, $\hat{\mathcal{P}}\hat{\mathcal{T}}$ symmetry in non-Hermitian systems has been utilized for

improved sensing [29]. With this brief discussion, we explicitly evaluate non-Hermiticity and $\hat{\mathcal{P}}\hat{\mathcal{T}}$ symmetry of the Hamiltonian [described in Eq. (2.29)] in the next chapter.

We have seen in the previous chapter that the Hamiltonian depends upon Ω parameter, which is directly related to the intensity of pump beam. In the following chapters, we will experimentally tune the input pump intensity and profile of generated beams (through filamentation), having opposite pseudo-charges is captured at the camera. The observed profiles are actually a linear combination of the eigenvectors of our Hamiltonian. If our Hamiltonian is non-Hermitian, then by varying pump intensity, it has a possibility to cross the EP. Eigenvectors at $\hat{\mathcal{P}}\hat{\mathcal{T}}$ symmetric region and $\hat{\mathcal{P}}\hat{\mathcal{T}}$ broken region are different from each other and at the EP, the eigenvectors will coalesce. This would be evident from a sharp change in profile of the beam while tuning pump intensity.

References

[1] Laurie M. Brown. Paul A.M. Dirac's The Principles of Quantum Mechanics. *Physics in Perspective*, 8(4):381–407, Dec 2006.

[2] Nimrod Moiseyev. *Non-Hermitian Quantum Mechanics*. Cambridge University Press, Cambridge, England, May 2011.

[3] Carl M Bender, Patrick E Dorey, Clare Dunning, Andreas Fring, Daniel W Hook, Hugh F Jones, Sergii Kuzhel, Géza Lévai, and Roberto Tateo. *PT Symmetry*. World Scientific (Europe), 1st edition, 2019.

[4] B H Bransden and C J Joachain. *Physics of atoms and molecules*. Prentice-Hall, London, England, 2nd edition, Apr 2003.

[5] Carl M. Bender, Stefan Boettcher, and Peter N. Meisinger. $\mathcal{PT}$ -symmetric quantum mechanics. *Journal of Mathematical Physics*, 40(5):2201–2229, 05 1999.

[6] Carl M. Bender and Stefan Boettcher. Real Spectra in Non-Hermitian Hamiltonians Having P T Symmetry. *Physical Review Letters*, 80(24):5243–5246, June 1998.

[7] Carl M. Bender, Dorje C. Brody, and Hugh F. Jones. Complex Extension of Quantum Mechanics. *Physical Review Letters*, 89(27):270401, December 2002.

[8] Carl M. Bender, Dorje C. Brody, and Hugh F. Jones. Must a hamiltonian be hermitian? *American Journal of Physics*, 71(11):1095–1102, 11 2003.

[9] Carl M Bender. Introduction to PT-symmetric quantum theory. *Contemporary Physics*, 46(4):277–292, 2005.

[10] Shachar Klaiman and Lorenz S. Cederbaum. Non-hermitian hamiltonians with space-time symmetry. *Phys. Rev. A*, 78:062113, Dec 2008.

[11] Mohammad-Ali Miri and Andrea Alù. Exceptional points in optics and photonics. *Science*, 363(6422):eaar7709, 2019.

[12] Emil J. Bergholtz, Jan Carl Budich, and Flore K. Kunst. Exceptional topology of non-hermitian systems. *Rev. Mod. Phys.*, 93:015005, Feb 2021.

[13] Junhua Dong, Qingmei Hu, Chang-Yin Ji, Bingsuo Zou, and Yongyou Zhang. Exceptional points in a topological waveguide-cavity coupled system. *New Journal of Physics*, 23(11):113025, Nov 2021.

[14] Haim Suchowski, Gil Porat, and Ady Arie. Adiabatic processes in frequency conversion. *Laser & Photonics Reviews*, 8(3):333–367, 2014.

[15] W. D. Heiss. The physics of exceptional points. *Journal of Physics A: Mathematical and Theoretical*, 45(44):444016, October 2012.

[16] W. D. Heiss. Phases of wave functions and level repulsion. *The European Physical Journal D - Atomic, Molecular, Optical and Plasma Physics*, 7(1):1–4, Aug 1999.

[17] M. V. Berry. Physics of nonhermitian degeneracies. *Czechoslovak Journal of Physics*, 54(10):1039–1047, Oct 2004.

[18] Géza Lévai and Miloslav Znojil. Systematic search for □□□□-symmetric potentials with real energy spectra. *Journal of Physics A: Mathematical and General*, 33(40):7165, oct 2000.

[19] Renan L. Thomes, Matheus I. N. Rosa, and Alper Erturk. Experimental realization of tunable exceptional points in a resonant non-hermitian piezoelectrically coupled waveguide. *Applied Physics Letters*, 124(6):061702, 02 2024.

[20] M. Said Ergoktas, Sina Soleymani, Nurbek Kakenov, Kaiyuan Wang, Thomas B. Smith, Gokhan Bakan, Sinan Balci, Alessandro Principi, Kostya S. Novoselov,

Sahin K. Ozdemir, and Coskun Kocabas. Topological engineering of terahertz light using electrically tunable exceptional point singularities. *Science*, 376(6589):184–188, 2022.

[21] Ali Mostafazadeh. Pseudo-hermiticity and generalized pt- and cpt-symmetries. *Journal of Mathematical Physics*, 44(3):974–989, 03 2003.

[22] Ali Mostafazadeh. Pseudo-hermitian representation of quantum mechanics. *International Journal of Geometric Methods in Modern Physics*, 07(07):1191–1306, 2010.

[23] Ali Mostafazadeh. Pseudo-hermiticity versus pt symmetry: The necessary condition for the reality of the spectrum of a non-hermitian hamiltonian. *Journal of Mathematical Physics*, 43(1):205–214, 01 2002.

[24] Changqing Wang, Zhoutian Fu, Wenbo Mao, Jinran Qie, A. Douglas Stone, and Lan Yang. Non-hermitian optics and photonics: from classical to quantum. *Adv. Opt. Photon.*, 15(2):442–523, Jun 2023.

[25] Vladimir V. Konotop, Jianke Yang, and Dmitry A. Zezyulin. Nonlinear waves in $\mathcal{PT}$-symmetric systems. *Rev. Mod. Phys.*, 88:035002, Jul 2016.

[26] R. El-Ganainy, K. G. Makris, D. N. Christodoulides, and Ziad H. Musslimani. Theory of coupled optical pt-symmetric structures. *Opt. Lett.*, 32(17):2632–2634, Sep 2007.

[27] Zin Lin, Hamidreza Ramezani, Toni Eichelkraut, Tsampikos Kottos, Hui Cao, and Demetrios N. Christodoulides. Unidirectional invisibility induced by $\mathcal{PT}$-symmetric periodic structures. *Phys. Rev. Lett.*, 106:213901, May 2011.

[28] Bo Peng, Şahin Kaya Özdemir, Fuchuan Lei, Faraz Monifi, Mariagiovanna Gianfreda, Gui Lu Long, Shanhui Fan, Franco Nori, Carl M. Bender, and Lan Yang. Parity–time-

symmetric whispering-gallery microcavities. *Nature Physics*, 10(5):394–398, May 2014.

[29] Weijian Chen, Şahin Kaya Özdemir, Guangming Zhao, Jan Wiersig, and Lan Yang. Exceptional points enhance sensing in an optical microcavity. *Nature*, 548(7666):192–196, Aug 2017.

Chapter 4

Experimental generation of synthetic fields from symmetric pump wavefront

4.1 Introduction

A non-uniformity in the transverse magnetic field ($\vec{B}$) is the most crucial and distinguishing factor that led to splitting of eigenstates for a homogeneous beam of neutral Ag-atoms in the original Stern-Gerlach (SG) experiment [1, 2, 3, 4]. The outcomes of the experiment established *spin* as an admissible degree of freedom (DoF) as well as quantization of spin angular-momentum. Since then, a variety of interacting physical systems have been explored where the idea of pseudo-spin DoF has been constructed by virtue of dynamical exchange of energy or matter-waves between the basis pseudo-spin states [5, 6, 7, 8, 9]. Although SG experiment have underpinnings in fundamentals of quantum mechanical formalism, the SG-effect forms the basis for preparing and manipulating quantum states for spintronic based manipulation in quantum computation and communication [10, 11]. The analytical framework describing the SG-effect provides a platform for exploring the dynamics of mixed quantum states, entanglement and nonlocality as well as the quantum measurement problem in spintronics and opto-spintronics [12, 13, 8, 14].

In photonic systems, the absence of a direct interaction between $\vec{B}$ with any DoF for photons eludes an exactly equivalent SG experiment using light beams [15, 12]. Gauge-dependent synthetic magnetic fields ($\vec{\mathcal{B}}$), which interact with intrinsic pseudo-spin states [16] or geometry-driven pseudo-spin states [17], are viable options for realizing an equivalent SG-effect [18, 19]. It is important to note that the intrinsic pseudo-spin states such as

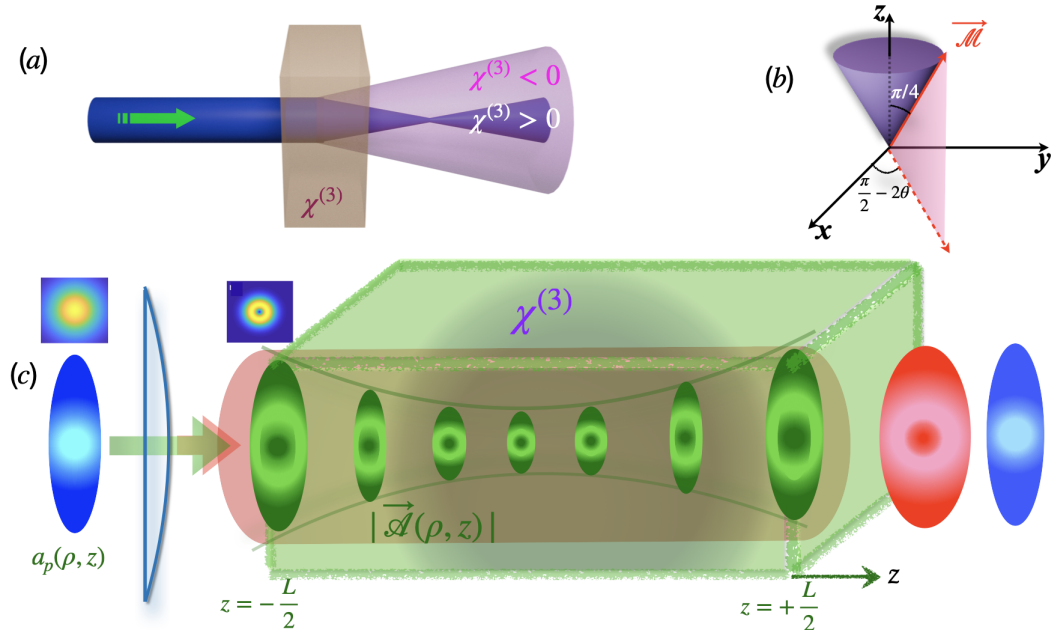

Figure 4.1: (a) shows self-action based focusing ($\chi^{(3)} > 0$) and defocusing ($\chi^{(3)} < 0$) of a Gaussian beam. (b) Orientation of analogous magnetizing field ($\vec{\mathcal{M}}$) showing that tip of the vector traces a cone of semi-angle $\frac{\pi}{4}$. The pump topological charge (θ) governs the $x - y$ span for $\vec{\mathcal{M}}$. (c) shows the evolution of pseudo-vector potential depicted by green colored wavefront ($|\vec{\mathcal{A}}| \propto |\vec{\nabla}_T \Phi|$) for an incident moderately focused Gaussian pump beam (blue colored wavefront) in a NLO medium (length L) with $\chi^{(3)} < 0$. The collimated Gaussian probe is depicted by red-colored wavefront.

circular polarization ($|\sigma_+\rangle$ or $|\sigma_-\rangle$) or polaritonic magnetic moments are restricted to two-dimensions [20, 21]. In general, nonlinear optical (NLO) systems are convenient choice for exploring multi-dimensional topological interactions owing to the fact that they are naturally perturbative that could be topologically trivial as well as non-trivial [22]. A. Karnieli *et al.* have demonstrated the SG-like splitting in a $\chi^{(2)}$-mediated sum-frequency-generation process by defining spinors in frequency basis [23, 24]. As a natural extension, the authors proposed recipe for emulating spin-transport and topological Hall effect with periodically-poled nonlinear crystals in two-dimensions [25]. In a recent report [26], an external DC electric field is employed to realize SG-like deflection in the eigen-polarizations for a periodically-poled electro-optic system. Similar experiments have been proposed in

coherently-coupled alkaline-earth single-atoms with traveling wave [27]. At the heart of such investigations lies the dynamics of Hermitian systems which ensures orthonormality of eigenstates and consequently, the definition of gauge-driven synthetic electric ($\vec{\mathcal{E}}$) and magnetic ($\vec{\mathcal{B}}$) fields are straightforward [25]. However, such a freedom is not obvious in a non-Hermitian photonic system where the symmetry constraints dictate orthogonality (or bi-orthogonality) of eigenstates [28, 29]. This is essentially due to the negative-norm eigenstates of a non-Hermitian system which requires redefining the Hilbert space [30, 31]. Among the non-Hermitian photonic systems, the Hamiltonians commuting with $\hat{\mathcal{P}}\hat{\mathcal{T}}$-operator hold a special significance owing to a spectrum of real eigenvalues along with existence of bi-orthonormal eigenstates [32]. However, the possibility of spontaneous $\hat{\mathcal{P}}\hat{\mathcal{T}}$-symmetry breaking at the exceptional point (EP) singularities complicates the *pseudo*-Hermitian dynamics and hence, the definition of synthetic fields is jeopardized [33]. A plausible alternative is to identify a non-Hermitian photonic system that remains $\hat{\mathcal{P}}\hat{\mathcal{T}}$-symmetric across the entire eigenvalue spectrum [34]. Here, we present a $\chi^{(3)}$ nonlinearity-led dynamical interaction between paraxial optical beams that exhibits a non-Hermitian character with a broadband $\hat{\mathcal{P}}\hat{\mathcal{T}}$ anti-symmetric eigenvalue spectrum when $Re(\chi^{(3)}) < 0$ [35]. A pump-probe based experimental configuration is used for observing all-optical SG-like spatial splitting of the spatial structure of the probe into *spatial-bin* or *path-bin* superposition states that are formed by combination of two spatial modes of NLO system. In the experimental configuration, the spin-degree of freedom exhibits a direct analogy with two *spatial-bins* and the gradient in $\vec{B}$ has an analogy with the spatial gradient of the pump intensity. Through an analytical formalism, we also present a feasible route for exploring topologically non-trivial manifestations in such $\chi^{(3)}$-led refractive optical nonlinearities.

4.2 Theoretical Model

We adopt the same formalism depicted in the previous chapter for third order nonlinear interaction. A negative $\chi^{(3)}$ in a cylindrically-symmetric refractive index distribution, as shown in Fig. 4.1(a), would result in the formation of stable dark solitons that are characterized by healing length $\xi \propto \frac{1}{\chi^{(3)}}$ [36]. A strong pump beam is described as $|\psi_p(\vec{r})\rangle = \frac{1}{2}[a_p(\vec{r})e^{i(\omega_p t - k_p z)} + c.c]$. It generates two co-propagating ansatz fields ($|\psi_\pm\rangle$) and their dynamics in the rotated frame are governed by the following equation

$$i\frac{\partial}{\partial z}|\Psi'\rangle = \left[\frac{(\vec{p}_T - q_e\vec{\mathcal{A}})^2}{2M} + q_e(-\vec{\sigma}\cdot\vec{\mathcal{M}}) + k_p\sigma_z\right]|\Psi'\rangle \tag{4.1}$$

where $|\Psi'\rangle = U^\dagger(a_+ \quad a_-^*)^T$ with $U = \text{diag}\ (e^{i\Phi}, e^{-i\Phi})$ and Φ is the dynamic phase acquired by pump beam. $\vec{\mathcal{A}} = \frac{i}{q_e}U^\dagger\vec{\nabla}_T U = -\frac{1}{q_e}(\vec{\nabla}_T\Phi)\sigma_z$ is the synthetic magnetic vector potential, $\vec{\mathcal{M}} = \vec{\mathcal{M}}_T + \mathcal{M}_z\hat{z} = \frac{\Omega}{q_e}[\sin(2\theta)e^{-i(2m+1)\pi/2}\hat{x} + \cos(2\theta)e^{i(2m+1)\pi/2}\hat{y} + \hat{z}]$ ($m = \pm1, \pm2, \cdots$) is synthetic magnetization with $\Omega = \frac{\omega_p}{c}n_2 I_p(\vec{\rho})$ and $a_p(\vec{\rho}) = \mathbb{A}_p(\vec{\rho})e^{-i\theta(\vec{\rho})}$ ($\mathbb{A}_p$ and θ being real). Interestingly, $\vec{\mathcal{M}}$ is always inclined at 45° with respect to z-axis and therefore, a suitable coordinate frame rotation would locally decouple the dynamical evolution of pseudo-spin basis states (see Fig. 4.1(b)). From a geometrical perspective, $|\Psi'\rangle$ evolves through a trajectory which is dictated by the parameters Ω and θ which are (all) governed by the pump field ($|\psi_p(\vec{\rho})\rangle$). From an experimental viewpoint, the ansatz fields are associated with a 'probe' field that could be wavelength detuned with respect to the strong pump beam. A signal probe beam could be restructured via optimum tailoring of eigenvalues of the Hamiltonian $\hat{H} = \frac{(\vec{p}_T - q_e\vec{\mathcal{A}})^2}{2M} + q_e\mathcal{V}$, through a suitable spatial gradient in the pump beam. In this backdrop, we intend to borrow the formalism for comprehending the original SG experiment which prescribes that a space-dependent (real) magnetic field would generate a gauge-dependent electric field in an emergent charge picture.

Having knowledge of synthetic vector potential ($\vec{\mathcal{A}}$) and synthetic scalar potential ($\mathcal{V}$), the synthetic fields are evaluated below

$$\begin{aligned}\vec{\mathcal{E}} &= -\vec{\nabla}_T\mathcal{V} - \frac{\partial\vec{\mathcal{A}}}{\partial z} \\ &= -\vec{\nabla}_T(-\vec{\sigma}\cdot\vec{\mathcal{M}}) - \frac{\partial}{\partial z}\left(-\vec{\nabla}_T\Phi\right) \\ \vec{\mathcal{E}} &= 2\vec{\nabla}_T|\mathcal{M}_T|\sigma_z\end{aligned} \tag{4.2}$$

$$\vec{\mathcal{B}} = \vec{\nabla}_T \times \vec{\mathcal{A}} = \vec{\nabla}_T \times (-\vec{\nabla}_T\Phi) = 0 \tag{4.3}$$

In the present context, $\vec{\mathcal{B}} = 0$, due to conservative (path independent) nature of $\vec{\mathcal{A}}$ and $\vec{\mathcal{E}} = 2\vec{\nabla}_T|\mathcal{M}_T|\sigma_z$ owing to the fact that the angle between $\vec{\mathcal{M}}$ and z-axis is constant. Therefore, if we consider a moderately focused radially symmetric Gaussian pump beam $\left(I_p(\rho) = I_0 e^{-\frac{\rho^2}{w^2(z)}}\right)$ which would exert an identical transverse force $\vec{\mathcal{F}}_\pm \propto \vec{\nabla}_T|\mathcal{M}_T|$ on $|q_{e_\pm}\rangle$, respectively. By virtue of radial symmetry of Gaussian beams, $|q_{e_+}\rangle$ and $|q_{e_-}\rangle$ states would be displaced from $\rho = 0$ in opposite direction and would relocate to an equilibrium position where $\vec{\mathcal{F}}_\pm$ maximizes. Alternatively, a radially-symmetric $\vec{\mathcal{F}}_\pm$ would result in a doughnut-shaped beam where the radius of the hollow-core is governed by $|\vec{\nabla}_T I_p(\vec{\rho}, z)|$ (see Fig. 4.1(c)). The conjugate charge pairs ($|q_{e_\pm}\rangle$) are located on diametrically-opposite points on ring (of hollow-core). The formation of doughnut-shape could be alternately viewed as SG-like splitting between spin-states when the conventional $\vec{B}$-field is radially symmetric. Since, the $\vec{\mathcal{F}}_\pm \propto |\vec{\nabla}_T I_p(\vec{\rho}, z)|$, the hollow-core beam, in contrast to conventional Laguerre-Gauss (LG) beam, carries zero orbital angular momentum and hence, it is topologically trivial. This is, further, analogous to SG-effect where the separated spin (or pseudo-spin) states are topologically trivial [37]. The equivalence between SG effect and our $\chi^{(3)}$ mediated interaction is presented below in a tabular form.

Parameter	**Spin-1/2 System**	$\chi^{(3)}$ **dynamics**
States	$\|\uparrow\rangle, \|\downarrow\rangle$	$\|+\rangle, \|-\rangle$
Magnetic field	$\vec{B}$	$\vec{\mathcal{M}}$
Evolution Coordinate	t	z
Mass	m_e	$k_p\sigma_z$
Magnetic moment	$\mu = \mu_e$	$\mu = 1$

Table 4.1: Shows an equivalence between the associated parameters related to the spin-1/2 system and $\chi^{(3)}$ mediated interaction process.

4.3 $\mathcal{PT}$ symmetry

Prior to embarking on the experimental investigations and the computed solutions for Eq. (4.1), we note an interesting manifestation of the Hamiltonian $\hat{H}$. In the conventional Hermitian algebra, a measurement of the spatial structure of an arbitrary probe beam, after the $\chi^{(3)}$-mediated interaction, could be expressed through an appropriate linear superposition of linearly independent solutions of $\hat{H}$. In the present case, however, the Hamiltonian represented by Eq. (2.19) exhibits a non-Hermitian character by virtue of the fact that $\hat{H}^\dagger \neq \hat{H}$ which manifests through non-orthogonal eigenstates [32]. To gain more deeper insight, we rewrite the equation (4.1) in the following form

$$i\frac{\partial}{\partial z}|\Psi'\rangle = \frac{1}{2k_p}\begin{pmatrix} (\vec{p}_T + \vec{\nabla}_T\Phi)^2 - \Gamma + 2k_p^2 & -\Gamma e^{-2i\theta} \\ \Gamma e^{2i\theta} & -(\vec{p}_T - \vec{\nabla}_T\Phi)^2 + \Gamma - 2k_p^2 \end{pmatrix}|\Psi'\rangle \tag{4.4}$$

where, we have assumed $\Gamma = \frac{3\chi^{(3)}\omega_p^2}{c^2}|a_p|^2$. A comparison of Eq. (4.4) with the Schrodinger equation, the Hamiltonian of the system could be expressed as

$$\hat{H} = \frac{1}{2k_p}\begin{pmatrix} (\vec{p}_T + \vec{\nabla}_T\Phi)^2 - \Gamma + 2k_p^2 & -\Gamma e^{-2i\theta} \\ \Gamma e^{2i\theta} & -(\vec{p}_T - \vec{\nabla}_T\Phi)^2 + \Gamma - 2k_p^2 \end{pmatrix} \tag{4.5}$$

Also, the Hermitian conjugate is given by,

$$\hat{H}^{\dagger} = \frac{1}{2k_p}\begin{pmatrix} (\vec{p}_T + \vec{\nabla}_T\Phi)^2 - \Gamma + 2k_p^2 & \Gamma e^{-2i\theta} \\ -\Gamma e^{2i\theta} & -(\vec{p}_T - \vec{\nabla}_T\Phi)^2 + \Gamma - 2k_p^2 \end{pmatrix} \tag{4.6}$$

where it is apparent that $\hat{H}^{\dagger} \neq \hat{H}$, thereby, implying Hamiltonian to represent a non-Hermitian dynamical interaction. In order to get a deeper insight, we consider an important symmetry, also known as parity-time ($\hat{\mathcal{P}}\hat{\mathcal{T}}$) symmetry of $\hat{H}$ where $\hat{\mathcal{P}}$ and $\hat{\mathcal{T}}$ are parity and time-reversal operator respectively. Here, $\hat{\mathcal{P}} = \begin{pmatrix} 0 & 1 \\ 1 & 0 \end{pmatrix}$ is chosen as the parity operator and the time-reversal operator is defined as $\hat{\mathcal{T}} = \hat{\mathcal{D}}\hat{\mathcal{K}}$ where $\hat{\mathcal{K}}$ is the charge conjugation operator and $\hat{\mathcal{D}}$ is a unitary operator ($\hat{\mathcal{D}} = \mathbb{I}$ for this case).

The commutation of $\hat{\mathcal{P}}\hat{\mathcal{T}}$ operator with $\hat{H}$ reveals,

$$\begin{aligned}
&\mathcal{PT}H(\mathcal{PT})^{-1} \\
&= \mathcal{PT}H\mathcal{T}^{-1}\mathcal{P}^{-1} \\
&= \mathcal{P}(\mathcal{T}H\mathcal{T}^{-1})\mathcal{P}^{-1} \\
&= \mathcal{P}H^{*}\mathcal{P}^{-1} \\
&= \begin{pmatrix} 0 & 1 \\ 1 & 0 \end{pmatrix}\frac{1}{2k_p}\begin{pmatrix} (-\vec{p}_T + \vec{\nabla}_T\Phi)^2 - \Gamma + 2k_p^2 & -\Gamma e^{2i\theta} \\ \Gamma e^{-2i\theta} & -(-\vec{p}_T - \vec{\nabla}_T\Phi)^2 + \Gamma - 2k_p^2 \end{pmatrix}\begin{pmatrix} 0 & 1 \\ 1 & 0 \end{pmatrix} \\
&= \frac{1}{2k_p}\begin{pmatrix} -(\vec{p}_T + \vec{\nabla}_T\Phi)^2 + \Gamma - 2k_p^2 & \Gamma e^{-2i\theta} \\ -\Gamma e^{2i\theta} & (\vec{p}_T - \vec{\nabla}_T\Phi)^2 - \Gamma + 2k_p^2 \end{pmatrix} \\
&\Rightarrow \mathcal{PT}H(\mathcal{PT})^{-1} = -H \\
&\Rightarrow \mathcal{PT}H = -H\mathcal{PT} \\
&\Rightarrow \{H, \mathcal{PT}\} = 0
\end{aligned} \tag{4.7}$$

Here, $\{\}$ signifies anti-commutation operation. So, the eigenstates of $\hat{H}$ anti-commute

with the product $\hat{\mathcal{P}}\hat{\mathcal{T}}$ operator $i.e.$ $\hat{\mathcal{P}}\hat{\mathcal{T}}\hat{\mathcal{H}}\hat{\mathcal{T}}^{-1}\hat{\mathcal{P}}^{-1} = -\hat{\mathcal{H}}$ [30]. In this $\hat{\mathcal{P}}\hat{\mathcal{T}}$ anti-symmetric regime, there are identical numbers of positive as well as negative norm eigenstates. Additionally, the Hamiltonian exhibit pseudo-Hermiticity by virtue of the fact that $\hat{\eta}\hat{H}\hat{\eta}^{-1} = -\hat{H}^{\dagger}$ where the intertwining operator $\hat{\eta} \equiv \sigma_y$ for the $\hat{\mathcal{P}}\hat{\mathcal{T}}$ anti-symmetric system [30].

This anti-commutation essentially implies that the eigenvalues will be real and the dynamics will be oscillatory for a range of dynamical parameters in $\hat{H}$. In order to appreciate this point, we note that the eigenvalues of $\hat{H}$

$$e_{\pm} = \frac{1}{2k_p}\left[2\left(\vec{p}_T \cdot \vec{\nabla}_T\Phi\right) \pm \sqrt{\left(p_T^2 + (\nabla_T\Phi)^2 - \Gamma + 2k_p^2\right)^2 - \Gamma^2}\right] \tag{4.8}$$

It is interesting to note that the eigenvalues $e_{\pm}$ always real if $\chi^{(3)} < 0$ and hence $\Gamma < 0$. Alternately, the nonlinear interaction will always mimic a Hermitian dynamics for medium exhibiting negative nonlinear refractive index ($n_2 < 0$). However, in such a scenario, the orthonormality of eigenvectors is not obvious owing to the negative-norm states of $\hat{H}$. In order to explicitly show this, we estimate two distinct eigenvectors for each eigenvalue viz. left eigenvector ($|\xi_{L_{\pm}}\rangle$) and right eigenvector ($|\xi_{R_{\pm}}\rangle$).

For $e_+ = \frac{1}{2k_p}\left[2\left(\vec{p}_T \cdot \vec{\nabla}_T\Phi\right) + \sqrt{\left(p_T^2 + (\nabla_T\Phi)^2 - \Gamma + 2k_p^2\right)^2 - \Gamma^2}\right]$, the right and left eigenvectors are

$$|\xi_{R_+}\rangle = \begin{pmatrix} 1 \\ \frac{e^{2i\theta}}{\Gamma}\left[\xi - \beta - 2\left(\vec{p}_T \cdot \vec{\nabla}_T\Phi\right)\right] \end{pmatrix} \tag{4.9}$$

$$\langle\xi_{L_+}| = \begin{pmatrix} 1 & -\frac{e^{-2i\theta}}{\Gamma}\left[\xi - \beta - 2\left(\vec{p}_T \cdot \vec{\nabla}_T\Phi\right)\right] \end{pmatrix} \tag{4.10}$$

Here, $\xi = \left((\vec{p}_T + \vec{\nabla}_T\Phi)^2 - \Gamma + 2k_p^2\right)$ and $\beta = \sqrt{\left(p_T^2 + (\nabla_T\Phi)^2 - \Gamma + 2k_p^2\right)^2 - \Gamma^2}$

has been assumed for simplification.
Similarly, for $e_- = \frac{1}{2k_p}\left[2\left(\vec{p}_T\cdot\vec{\nabla}_T\Phi\right) - \sqrt{\left(p_T^2+(\nabla_T\Phi)^2-\Gamma+2k_p^2\right)^2-\Gamma^2}\right]$, the right and left eigenvectors are

$$|\xi_{R_-}\rangle = \begin{pmatrix} 1 \\ \frac{e^{2i\theta}}{\Gamma}\left[\xi+\beta-2\left(\vec{p}_T\cdot\vec{\nabla}_T\Phi\right)\right] \end{pmatrix} \tag{4.11}$$

$$\langle\xi_{L_-}| = \begin{pmatrix} 1 & -\frac{e^{-2i\theta}}{\Gamma}\left[\xi+\beta-2\left(\vec{p}_T\cdot\vec{\nabla}_T\Phi\right)\right] \end{pmatrix} \tag{4.12}$$

Now, the inner products of one left & one right eigenvector and of two right eigenvectors are evaluated below

$$\begin{aligned}
\langle\xi_{L_-}|\xi_{R_+}\rangle &= \begin{pmatrix} 1 & -\frac{e^{-2i\theta}}{\Gamma}\left[\xi+\beta-2\left(\vec{p}_T\cdot\vec{\nabla}_T\Phi\right)\right] \end{pmatrix} \begin{pmatrix} 1 \\ \frac{e^{2i\theta}}{\Gamma}\left[\xi-\beta-2\left(\vec{p}_T\cdot\vec{\nabla}_T\Phi\right)\right] \end{pmatrix} \\
&= 1-\frac{1}{\Gamma^2}\left[\left(\xi-2\left(\vec{p}_T\cdot\vec{\nabla}_T\Phi\right)\right)^2-\beta^2\right] \\
&= 1-\frac{1}{\Gamma^2}\left[\left\{p_T^2+(\nabla_T\Phi)^2-\Gamma+2k_p^2\right\}^2-\left\{\left(p_T^2+(\nabla_T\Phi)^2-\Gamma+2k_p^2\right)^2-\Gamma^2\right\}\right] \\
&= 1-\frac{1}{\Gamma^2}\Gamma^2 \\
\langle\xi_{L_-}|\xi_{R_+}\rangle &= 0
\end{aligned} \tag{4.13}$$

$$\begin{aligned}
\langle\xi_{R_-}|\xi_{R_+}\rangle &= \begin{pmatrix} 1 & \frac{e^{-2i\theta}}{\Gamma}\left[\xi+\beta-2\left(\vec{p}_T\cdot\vec{\nabla}_T\Phi\right)\right] \end{pmatrix} \begin{pmatrix} 1 \\ \frac{e^{2i\theta}}{\Gamma}\left[\xi-\beta-2\left(\vec{p}_T\cdot\vec{\nabla}_T\Phi\right)\right] \end{pmatrix} \\
&= 1+\frac{1}{\Gamma^2}\left[\left(\xi-2\left(\vec{p}_T\cdot\vec{\nabla}_T\Phi\right)\right)^2-\beta^2\right] \\
&= 1+\frac{1}{\Gamma^2}\left[\left\{p_T^2+(\nabla_T\Phi)^2-\Gamma+2k_p^2\right\}^2-\left\{\left(p_T^2+(\nabla_T\Phi)^2-\Gamma+2k_p^2\right)^2-\Gamma^2\right\}\right] \\
&= 1+\frac{1}{\Gamma^2}\Gamma^2 \\
\langle\xi_{R_-}|\xi_{R_+}\rangle &= 2\neq 0
\end{aligned} \tag{4.14}$$

Hence, the eigenvectors of the Hamiltonian show a bi-orthogonality behaviour. Therefore, the present formalism depicts SG-like splitting in a $\hat{\mathcal{P}}\hat{\mathcal{T}}$ anti-symmetric system which, to the best of our knowledge, is yet to be shown. It is also interesting to note that, in absence of any topological structure in the pump beam *i.e.* $\theta = \eta\pi$ where η is an integer, $\hat{H}$ exhibits *particle-antiparticle* or *particle-hole* symmetry which is usually observed in BECs and superconductors. This is essentially a manifestation of the equivalence between *BdG* equation with the dynamical Eq. (4.1) [38, 39].

4.4 Experimental methods

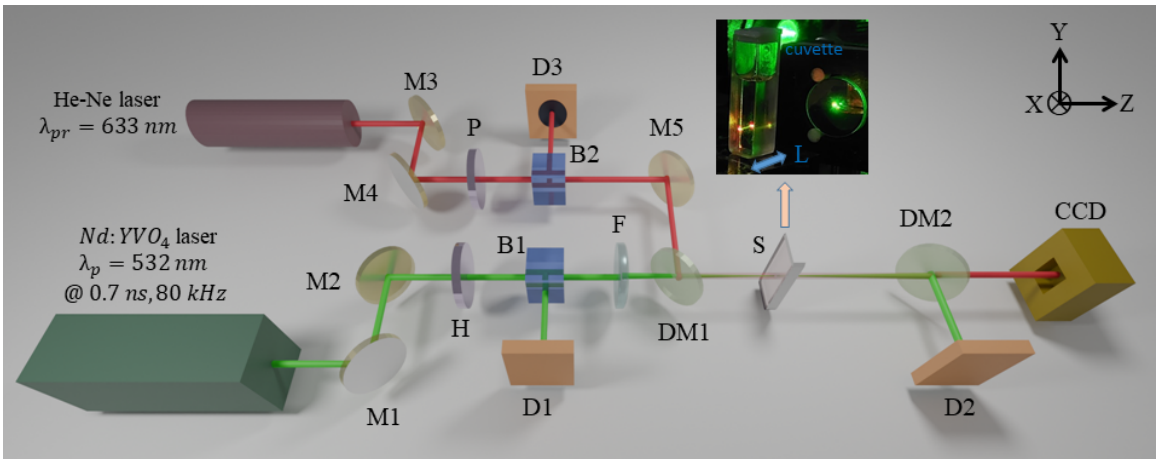

Figure 4.2: shows the collinear pump-probe based experimental configuration for observing SG-like effect in a radially symmetric synthetic electric field ($\vec{\mathcal{E}}$). B1: Polarizing beam-splitter; B2: Non-polarizing beam-splitter; S: sample; D1-D3: Power meter; H: Half-wave plate; P: Polarizer; M1-M5: Steering mirror; DM1 & DM2: Dichroic mirrors for realizing collinear arrangement; F: Plano-convex lens. *Inset*: $L = 1\ cm$ thick cuvette filled with toluene that exhibits $\chi^{(3)} < 0$ (defocusing) for $700\ ps$ pulsed laser centered at $532\ nm$ wavelength.

We prepare a collinear pump-probe experimental setup shown in Fig. 4.2 for observing the SG-like splitting in a $\chi^{(3)}$ medium. We use a frequency-doubled $Nd : YVO_4$ linearly-polarized pulsed laser (Wedge, BrightSolution Inc., Italy) as the pump source delivering a pulse of $\approx 700\ ps$ width (repetition rate = $80\ kHz$) at a central wavelength of

532 nm. The maximum pulse energy is 6 μJ in a TEM_{00} mode profile with $M^2 \leq$ 1.08. A combination of a half-wave plate (HWP) and a polarizing beam splitter (PBS) was used to attenuate the pump beam power in the experimental arm. A plano-convex lens of focal length $f = 100\ mm$ was employed to focus the pump beam which resulted in a maximum on-axis peak intensity of $\approx$ 220 MW/cm^2. Symmetrically around the focus ($z = 0$), we place a $L = 1\ cm$ thick cuvette filled with organic solvent 'toluene' which acts as a non-linear medium (inset of Fig. 4.2). The motivation behind choice of toluene is governed by high chemical as well as thermal stability along with high transparency in visible spectrum. Owing to thermo-optic manifestations, toluene exhibits negative nonlinear refractive index (n_2) when measured using nanosecond pulses. This is essentially due to thermally-induced optical nonlinearities in toluene [40, 41]. For our case, we have measured n_2 and hence, $Re(\chi^{(3)})$ for toluene using an open-aperture and closed-aperture (CA) Z-scan set-up with identical pump pulses which resulted in $Re(\chi^{(3)}) \approx -2.9 \times 10^{-19}\ m^2/V^2$ (see appendix A). A collimated, continuous wave (cw) beam from a $He - Ne$ laser source at wavelength $\lambda_{pr} = 632.8\ nm$ (Power $= 1\ mW$) is used as a probe beam. The choice of detuned probe beam is motivated by the realization of a collinear pump-probe configuration. In such a scenario, it appears that the nonlinear polarization ($P^{(3)}$) contains two distinguishable frequency components ω_{pr} and $(2\omega_p - \omega_{pr})$ where ω_{pr} is the angular frequency of probe beam. However, it is to be noted that $\omega_p - \omega_{pr} << \frac{\omega_{pr}}{2}$ in the present case. This ensures dominant nonlinear polarization to oscillate at ω_{pr} and consequently, the error involved in assuming identical $\chi^{(3)}$ for diagonal and off-diagonal terms of Eq. (2.19) is negligible [42, 43]. The transmitted pump and probe beams are combined and separated using dichroic mirrors (DM1 and DM2) and the probe beam structure is recorded by a CCD camera with a pixel size of 4.4 $\mu m \times 4.4\ \mu m$ (GRAS 2.0, Point Grey, USA) which is positioned at a distance of $z \approx$ 30 cm from the cuvette. In order to observe the modifications in the probe beam structure, we control the incident pump power by manually changing the slow and fast-axis

orientation of HWP.

4.5 Results

In our conceptual framework, the image recorded by the CCD camera is proportional to the squared amplitudes of linear superposition of $|\psi_{\pm}\rangle$ basis. The incident probe beam is a superposition of *space bin* ($|\psi_{\pm}\rangle$) states in the NLO medium. Since, the a_+ and a_- constitute the two-component spinor defined for the Hamiltonian $\hat{H}$, the transmitted beam would adhere to the dynamical Eq. (4.1). The recorded (transmitted) probe beam shape as a function of on-axis ($z = 0$) peak pump intensity (I_0) is shown in panel (i) of Fig. 4.3. At small I_0 ($\approx 10\ MW/cm^2$), the transmitted probe beam retains a Gaussian beam-shape. A null-intensity core appears at moderate I_0 ($\geq 50\ MW/cm^2$) values that appears to have a *vortex*-like character. The diameter of dark-hollow Gaussian (DHG) beam monotonically increases at higher I_0 values [44, 45, 46, 47]. At $I_0 \approx 220\ MW/cm^2$, the diameter of the bright ring is $\approx\ 1.9\ mm$ at the CCD plane and when projected back to $z = 0$ plane, the bright ring subtends an angle $\alpha_{ex} \approx 0.12°$. The appearance of dark core is a consequence of force ($\vec{\mathcal{F}}_{\pm}$) experienced by emergent charge states ($|q_{e_{\pm}}\rangle$) constituting the probe beam. Since, the pump exhibits a Gaussian shape $\left(I_p = I_0 e^{-\frac{2\rho^2}{w^2}}\right)$, this force is proportional to $\frac{dI_p}{d\rho}$ and it maximizes at $\rho_m = \frac{w}{2}$ where $w(z) = w_0\sqrt{1 + \left(\frac{z}{z_R}\right)^2}$ such that the Rayleigh range $z_R = \frac{\pi w_0^2 n(I_0)}{\lambda_p}$ depends on pump intensity. Using a knife-edge based beam profiler (NanoScan, Ophir, USA), the Gaussian pump beam waist (w_0) is measured to be $40\ \mu m$ that translates to $\rho_m \approx 90\ \mu m$ at the external exit face of the cuvette when $I_0 = 220\ MW/cm^2$. Therefore, from an analytical viewpoint, the bright ring is expected to subtend an angle $\alpha_{th} = 0.15°$ at $z = 0$ which is close to the measured α_{ex}.

In order to gain a deeper insight, we numerically solve Eq. (4.1) using the information available from the experiment such as pump intensity and shape, length and physical

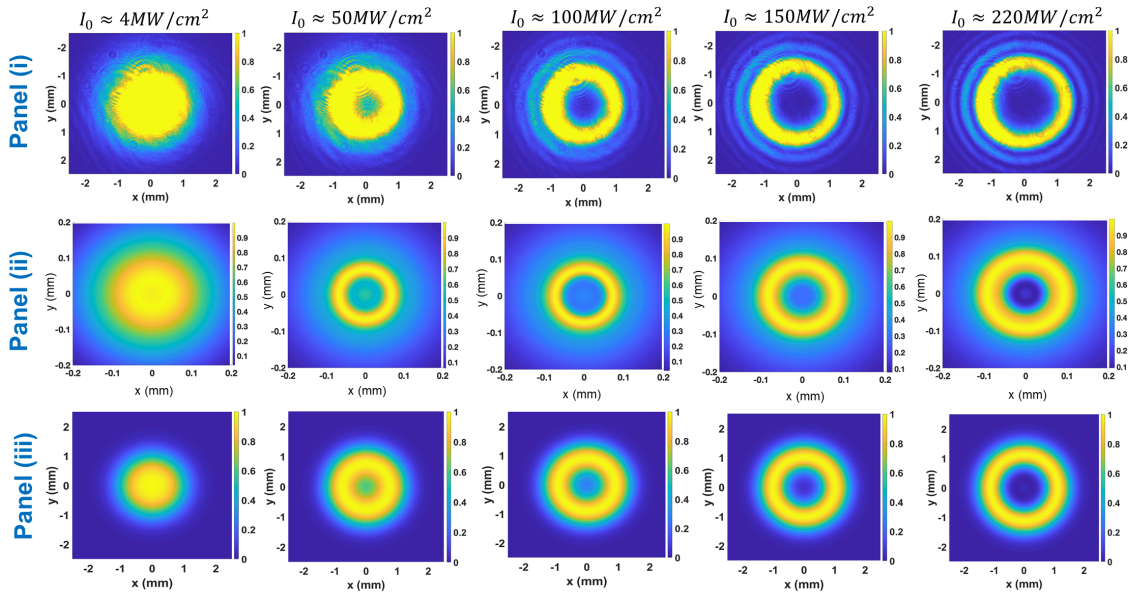

Figure 4.3: Panel (i) shows the recorded probe beam profiles in the CCD camera at different on-axis pump peak intensity (I_0). The dark-core width monotonically increases as a function of I_0 owing to a stronger gauge field driven emergent Lorentz force $\vec{\mathcal{F}}_{\pm} \propto \vec{\nabla}_T |\mathcal{M}_T|$. Panel (ii) shows simulated (using FD-BPM) probe beam profiles obtained by solving the dynamical Eq. (4.1) at $z = +\frac{L}{2}$ (exit face of cuvette). Panel (iii) shows simulated beam profiles at the CCD plane.

properties of toluene. The employed computational technique is finite-difference beam propagation method (FD-BPM) where the transverse (ρ) coordinates as well as the longitudinal (z) coordinate discretization is scaled with respect to wavelength of light. Equation (4.1) is simultaneously solved for a'_+ and $(a'_-)^*$ $\left(|\Psi'\rangle = [a'_+ \;\; (a'_-)^*]^T\right)$ at each discrete z-value by regularly updating the a'_+ and $(a'_-)^*$. By virtue of radial symmetry, we consider $a'_+(\rho, z = -\frac{L}{2})$ and $a'_-(\rho, z = -\frac{L}{2})$ to have Gaussian profile with an arbitrary phase. The transmitted beam profile is computed as a linear superposition of a'_+ and a'_- at $z = \frac{L}{2}$. The simulated probe intensity profiles are shown in panel (ii) of Fig. 4.3 which correspond to identical pump intensity levels shown in panel (i) of Fig. 4.3. Although, the transmitted probe beam profile exhibits close resemblance with experimental measurements, the spatial beam distortions in the recorded (panel (i)) probe beam, owing to thermally-induced den-

sity fluctuations in toluene, could not be modeled. Also, $\chi^{(3)}$ value for toluene is nominally overestimated in the simulations which is essentially driven by the fact that, at nanosecond time-scale (pulse-width), toluene exhibits strong accumulated thermal effects (ATE) [40]. The implications of panel (ii) of Fig. 4.3 could be appreciated by acknowledging the fact that the emergent Lorentz force $\vec{\mathcal{F}}_{\pm}$ exert oppositely directed forces on $|\psi_{\pm}\rangle$ photon states respectively. As a consequence, the photons in $|\psi_{+}\rangle$ and $|\psi_{-}\rangle$ state deviate symmetrically about the propagation (z) axis. Since, $\left|\vec{\mathcal{F}}_{+}\right| = \left|\vec{\mathcal{F}}_{-}\right|$ is radially symmetric, $|\psi_{+}\rangle$ and $|\psi_{-}\rangle$ would form rings of identical diameter. However, the absence of *time-reversal* symmetry of $\hat{H}$ manifests through a non-identical phase acquisition by pseudo-spin basis. The superposition of $|\psi_{\pm}\rangle$ states yields the recorded probe beam intensity that is recorded in panel (i) of Fig. 4.3. Owing to the radial symmetry and strength of pump beam, the appearance of dark core diameter of the transmitted probe beam increases monotonically as a function of I_0 which is quantitatively represented in Fig. 4.4. The ring diameter is estimated through a weighted average of maximally intense CCD pixel for different I_0 values. The spatial evolution of transmitted probe (recorded) as a function of I_0 could also be seen in the "Visualization1".

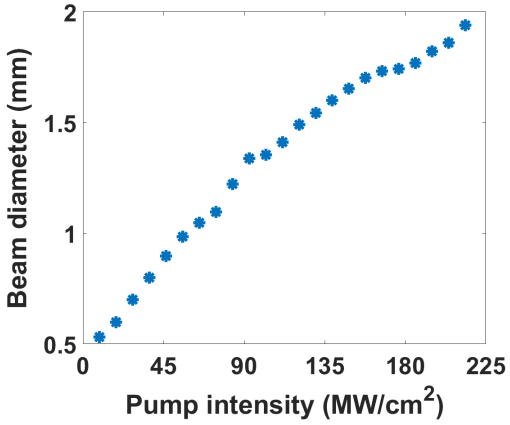

Figure 4.4: shows the variation of dark core diameter of DHG beam as a function on pump intensity. See Visualization 1 representing the evolution of probe beam as a function of increasing pump intensity (I_0).

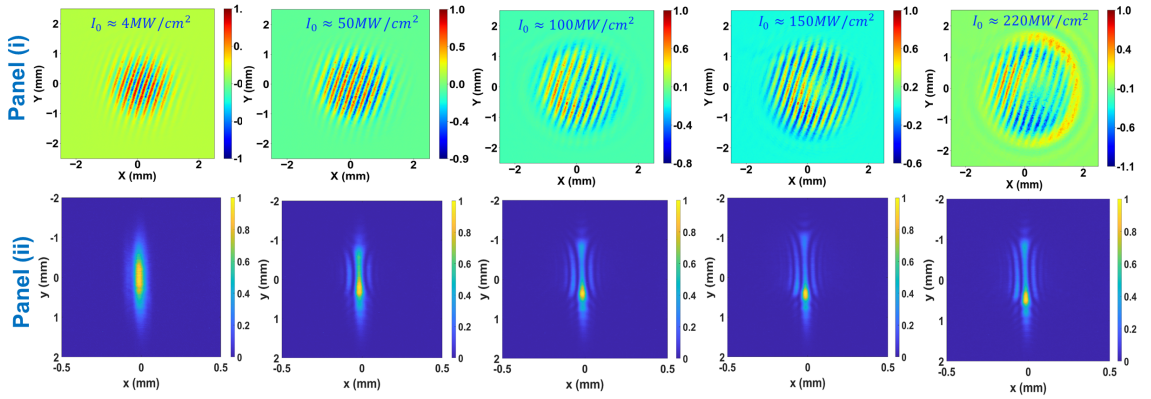

Figure 4.5: Panel (i) shows the recorded interference pattern for probe beam after subtracting reference and signal probe arm intensities at different on-axis maximum pump intensities (I_0). Panel (ii) shows recorded spatial profile of the transmitted probe beam at the focus of cylindrical lens of focal length $f = 100\ mm$. Both the panels indicate absence of an integral OAM state.

The phase evolution in the transmitted probe beam is ascertained by recording the interference pattern of the transmitted probe (or object) beam with a reference beam in a balanced Mach-Zehnder interferometer (MZI) [48, 49]. The background subtracted fringe patterns are shown in panel (i) of Fig. 4.5 which depicts the absence of any OAM carried by DHG beam [50, 51, 52]. As I_0 increases, the fringe pattern contrast exhibits a non-uniform distribution across the recording plane which is a significant appearance of small fractional OAM state of DHG beam. Alternatively, the OAM state is confirmed through a measurement using a cylindrical lens of focal length $f = 100\ mm$ [53]. Due to astigmatic transformation, a doughnut-shaped vortex beam would form 'dark-stripes' running across the brightest cross-section of the image [54]. The number and the orientation of 'dark stripes' is a measure of magnitude and sign of l respectively. The images on focal plane of cylindrical lens are shown in panel (ii) of Fig. 4.5 which shows the absence of 'dark stripes' depicting zero (or negligible) OAM in the DHG beam. Both these measurements are indicative of the fact that the gauge potentials ($\vec{\mathcal{A}}$ and $\mathcal{V}$) are pump-intensity dependent and therefore, the topological structure, if any, for the probe beam remains unaltered

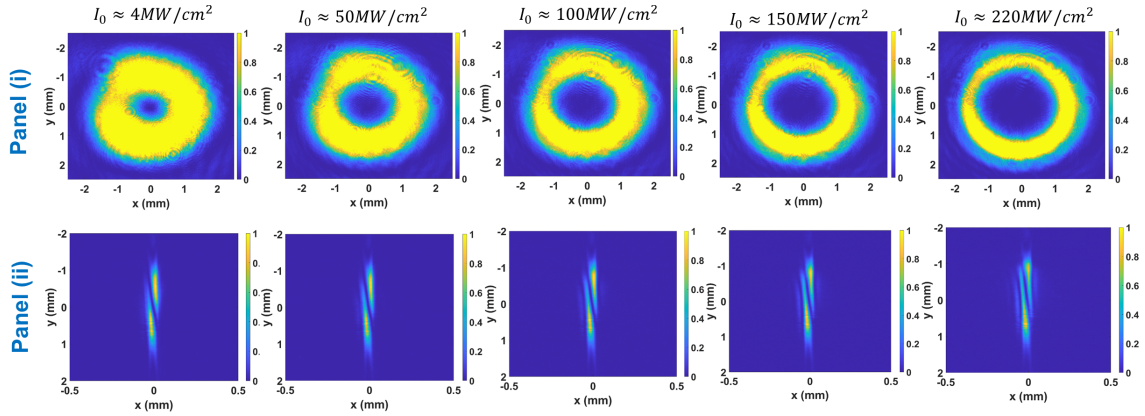

Figure 4.6: Panel (i) shows the recorded spatial profiles for the transmitted $l = 1$ vortex probe beam at different on-axis maximum pump peak intensity (I_0). Panel (ii) shows the recorded spatial profile of transmitted probe beam at the focus of cylindrical lens of focal length $f = 100\ mm$ depicting $l = 1$ OAM state.

in NLO interaction. In order to confirm that, we generate an $l = 1$ probe beam using a spiral phase plate (SPP) and record the transmitted probe beam which are shown in panel (i) of Fig. 4.6. There are minor changes in the dark hole diameter which is not apparent in the figures owing to the fact that the doughnut-shaped intensity distribution for $l = 1$ probe beam is maximum in the spatial regions where the emergent Lorentz force ($\vec{\mathcal{F}}_{\pm}$) is maximum. Consequently, the states ($|q_{e_{\pm}}\rangle$) almost remain at their position and hence, the transmitted probe beam retains a doughnut shape. The OAM-state measurement using an identical cylindrical lens is shown in panel (ii) of Fig. 4.6 which depicts the existence of $l = 1$ topological charge of the probe beam for all values of I_0. This is also confirmed through a 'fork'-like structure in the interference pattern of the transmitted ($l = 1$) probe beam with a plane wave (not shown here).

4.6 Discussion and outlook

We present an analytical framework and experimental investigations describing a $\chi^{(3)}$-mediated splitting of Gaussian probe beam into a doughnut-shaped DHG beam in the pres-

ence of a strong pump beam. The observations elucidate an all-optical analogue of SG-effect where symmetric fluctuations ($|\psi_+\rangle$ and $|\psi_-\rangle$) created by strong pump constitute the pseudo-spin ($|\uparrow_z\rangle$ and $|\downarrow_z\rangle$) basis states and the radially-symmetric gradient of the pump beam generate inhomogeneity in synthetic magnetization ($\vec{\mathcal{M}}$). By virtue of this, the pseudo-spin currents are deflected symmetrically in diametrically opposite directions about the centroid of Gaussian-shaped pump. From an experimental viewpoint, a Gaussian probe beam acquired a hollow core structure which is a superposition of transformed basis states $|\psi_g\rangle = \frac{|\psi_+\rangle + e^{2i\theta}|\psi_-\rangle}{\sqrt{2}}$ and $|\psi_e\rangle = \frac{|\psi_+\rangle - e^{2i\theta}|\psi_-\rangle}{\sqrt{2}}$. The dynamics exhibits a non-Hermitian $\hat{\mathcal{P}}\hat{\mathcal{T}}$ anti-symmetric character which entails appropriate pseudo-spin basis ($|\psi_+\rangle$ and $|\psi_-\rangle$) for realizing orthonormality. In other words, the beam restructuring which is governed by non-Hermitian dynamics, provides a viable route to realize an analogous SG-like splitting in a $\hat{\mathcal{P}}\hat{\mathcal{T}}$ symmetric system by utilizing a broad real eigenvalue spectrum for $\chi^{(3)} < 0$.

From a broader perspective, the Gaussian pump beam phase insensitivity inherits a unique character to the process of beam splitting and restructuring. Implicitly, this prescribes a smooth transfer of phase information of probe beam to its restructured counterpart. For example, in metrology, a doughnut-shaped beam improves the image fidelity in ptychography of periodically-patterned photonic and electronic structures for defect inspection as well as stimulated emission depletion (STED) microscopy [55, 56]. A natural extension would be to achieve high-fidelity ptychographic imaging of multi-periodic, quasi-periodic or distributed-periodic photonic or optical systems. This would essentially require dynamically tailorable 'dark hollow core' of the vortex beam. However, in conventional vortex beam generation, the possibility of structural tailoring must necessarily be accompanied by phase manipulation and dynamic reconfiguration of the set-up. The NLO based DHG beam generating and restructuring described here allows us to dynamically tailor the diameter of 'doughnut' without affecting its phase structure as shown in Fig. 4.4.

From quantum photonics perspective, the possibility of spatially relocating anti-bunched

correlated photons in concentric rings that are distinguishable in at least one degree of freedom such as frequency or polarization is an attractive proposition. In order to accomplish such a possibility, we incident a moderately focused strong (classical) pump beam on a polarization sensitive (or birefringent) NLO medium along with a linearly polarized signal single-photon (anti-bunched) stream. In the horizontal ($|H\rangle$) and vertical ($|V\rangle$) polarization basis, the $\chi^{(3)}$-mediated interaction of photons would be governed by dynamical equation similar to that described by Eq. (4.1). As an outcome, a ring pattern would be formed such that the correlated pair of photons are spatially located at diametrically opposite points on the ring. A natural extension would invite a spatial asymmetry in the strong pump beam which would spatially separate the spontaneously generated correlated photon pairs, thereby replacing a conventional beam splitter with NLO based tunable photon beam splitting [14]. This idea could be translated to $\chi^{(2)}$-mediated parametric downconversion process where the downconverted twin-photons that are distinguishable only in frequency, form a ring and correlated pairs are positioned diametrically opposite points on the ring [19].

References

[1] Walther Gerlach and Otto Stern. Der experimentelle Nachweis der Richtungsquantelung im Magnetfeld. *Zeitschrift fur Physik*, 9:349–352, December 1922.

[2] O. Gorceix, J. Robert, S. Nic Chormaic, Ch. Miniatura, and J. Baudon. Dispersive and nondispersive phase shifts in atomic Stern-Gerlach interferometry. *Physical Review A*, 50(6):5007–5013, December 1994.

[3] Gilbert Reinisch. Stern–Gerlach experiment as the pioneer – and probably the simplest – quantum entanglement test? *Physics Letters A*, 259(6):427–430, August 1999.

[4] Horst Schmidt-Böcking, Lothar Schmidt, Hans Jürgen Lüdde, Wolfgang Trageser, Alan Templeton, and Tilman Sauer. The Stern-Gerlach experiment revisited. *The European Physical Journal H*, 41(4-5):327–364, November 2016.

[5] H. Batelaan, T. J. Gay, and J. J. Schwendiman. Stern-Gerlach Effect for Electron Beams. *Physical Review Letters*, 79(23):4517–4521, December 1997.

[6] Yong Li, C. Bruder, and C. P. Sun. Generalized Stern-Gerlach Effect for Chiral Molecules. *Physical Review Letters*, 99(13):130403, September 2007.

[7] Shimon Machluf, Yonathan Japha, and Ron Folman. Coherent Stern–Gerlach momentum splitting on an atom chip. *Nature Communications*, 4(1):2424, September 2013.

[8] Mandip Singh. Quantum Stern-Gerlach experiment and path entanglement of a Bose-Einstein condensate. *Physical Review A*, 95(4):043620, April 2017.

[9] Ramin G. Daghigh, Michael D. Green, and Christopher J. West. A modified Stern-

Gerlach experiment using a quantum two-state magnetic field. *Results in Physics*, 9:740–744, June 2018.

[10] Leon Karpa and Martin Weitz. A Stern–Gerlach experiment for slow light. *Nature Physics*, 2(5):332–335, May 2006.

[11] Iacopo Carusotto and Cristiano Ciuti. Quantum fluids of light. *Reviews of Modern Physics*, 85(1):299–366, February 2013.

[12] A. Vaglica. Quantum fine structure of the optical Stern-Gerlach effect. *Physical Review A*, 54(4):3195–3205, October 1996.

[13] Ebrahim Karimi, Daniel Giovannini, Eliot Bolduc, Nicolas Bent, Filippo M. Miatto, Miles J. Padgett, and Robert W. Boyd. Exploring the quantum nature of the radial degree of freedom of a photon via Hong-Ou-Mandel interference. *Physical Review A*, 89(1):013829, January 2014.

[14] Aviv Karnieli and Ady Arie. Spectral path entanglement of photons using the all-optical Stern-Gerlach effect. In *Quantum Information and Measurement (QIM) V: Quantum Technologies*, page F5A.31, Rome, 2019. OSA.

[15] T. Sleator, T. Pfau, V. Balykin, O. Carnal, and J. Mlynek. Experimental demonstration of the optical Stern-Gerlach effect. *Physical Review Letters*, 68(13):1996–1999, March 1992.

[16] Oriol Arteaga, Enric Garcia-Caurel, and Razvigor Ossikovski. Stern-Gerlach experiment with light: separating photons by spin with the method of A Fresnel. *Optics Express*, 27(4):4758, February 2019.

[17] Ofir Yesharim, Aviv Karnieli, Giuseppe Di Domenico, Sivan Trajtenberg-Mills, and Ady Arie. Experimental Observation of the Stern Gerlach Effect in Nonlinear Op-

tics. In *Conference on Lasers and Electro-Optics*, page FTh1J.1, San Jose, California, 2021. Optica Publishing Group.

[18] Ofir Yesharim, Aviv Karnieli, Steven Jackel, Giuseppe Di Domenico, Sivan Trajtenberg-Mills, and Ady Arie. Observation of the all-optical Stern–Gerlach effect in nonlinear optics. *Nature Photonics*, 16(8):582–587, 2022.

[19] Abhishek Mondal and Ritwick Das. Experimental evidence of a pump-wavefront-induced Stern–Gerlach-like splitting in optical parametric generators. *Optics Letters*, 47(15):3668, August 2022.

[20] S. Edelstein, R. M. Abraham-Ekeroth, P. A. Serena, J. J. Sáenz, A. García-Martín, and M. I. Marqués. Magneto-optical Stern-Gerlach forces and nonreciprocal torques on small particles. *Physical Review Research*, 1(1):013005, August 2019.

[21] F. Pudonin, I. Sherstnev, and D. Kostzov. The Stern–Gerlach effect as a method for obtaining nanostructures with a given unidirectional anisotropy of optical properties. *Applied Physics Letters*, 125(24):241904, December 2024.

[22] Ling Lu, John D. Joannopoulos, and Marin Soljačić. Topological photonics. *Nature Photonics*, 8(11):821–829, November 2014.

[23] Aviv Karnieli and Ady Arie. All-Optical Stern-Gerlach Effect. *Physical Review Letters*, 120(5):053901, January 2018.

[24] Aviv Karnieli and Ady Arie. Frequency domain Stern–Gerlach effect for photonic qubits and qutrits. *Optica*, 5(10):1297, October 2018.

[25] Aviv Karnieli, Shai Tsesses, Guy Bartal, and Ady Arie. Emulating spin transport with nonlinear optics, from high-order skyrmions to the topological Hall effect. *Nature communications*, 12(1):1092, 2021.

[26] Wenguo Zhu, Xinzhou Liang, Weichao Xie, Huadan Zheng, Yongchun Zhong, Jieyuan Tang, Jianhui Yu, and Zhe Chen. Optical Stern–Gerlach Effect in Periodically Poled Electro□Optical Crystals. *Laser & Photonics Reviews*, 18(8):2301030, August 2024.

[27] Haihu Cui and Wenxi Lai. Optical Stern–Gerlach effect via a single traveling-wave light. *Journal of Physics B: Atomic, Molecular and Optical Physics*, 56(7):075501, April 2023.

[28] Carl M. Bender and Stefan Boettcher. Real Spectra in Non-Hermitian Hamiltonians Having P T Symmetry. *Physical Review Letters*, 80(24):5243–5246, June 1998.

[29] Carl M. Bender, Dorje C. Brody, and Hugh F. Jones. Complex Extension of Quantum Mechanics. *Physical Review Letters*, 89(27):270401, December 2002.

[30] Carl M. Bender and P. Dorey. *PT symmetry: in quantum and classical physics*. World Scientific Publishing Co. Pte. Ltd, 2018.

[31] Mustapha Maamache and Linda Kheniche. Anti-PT symmetry for a non-Hermitian Hamiltonian. *Progress of Theoretical and Experimental Physics*, 2020(12):123A01, December 2020.

[32] Katherine Jones-Smith and Harsh Mathur. Non-Hermitian quantum Hamiltonians with PT symmetry. *Physical Review A*, 82(4):042101, October 2010.

[33] W. D. Heiss. The physics of exceptional points. *Journal of Physics A: Mathematical and Theoretical*, 45(44):444016, October 2012.

[34] Ali Mostafazadeh. Exact PT-symmetry is equivalent to Hermiticity. *Journal of Physics A: Mathematical and General*, 36(25):7081, June 2003.

[35] Ryan S. Bennink, Vincent Wong, Alberto M. Marino, David L. Aronstein, Robert W. Boyd, C. R. Stroud, Svetlana Lukishova, and Daniel J. Gauthier. Honeycomb Pattern Formation by Laser-Beam Filamentation in Atomic Sodium Vapor. *Physical Review Letters*, 88(11):113901, February 2002.

[36] Govind P. Agrawal. *Nonlinear Fiber Optics*. Academic Press, 6th edition, 2019.

[37] E Benítez Rodríguez, L M Arévalo Aguilar, and E Piceno Martínez. Corrigendum: 'A full quantum analysis of the Stern–Gerlach experiment using the evolution operator method: analysing current issues in teaching quantum mechanics'. *European Journal of Physics*, 38(6):069501, November 2017.

[38] N. Westerberg, C. Maitland, D. Faccio, K. Wilson, P. Öhberg, and E. M. Wright. Synthetic magnetism for photon fluids. *Physical Review A*, 94(2):023805, August 2016.

[39] N. N. Bogolyubov. On the theory of superfluidity. *J. Phys. (USSR)*, 11:23–32, 1947.

[40] Mauro Falconieri. Thermo-optical effects in Z -scan measurements using high-repetition-rate lasers. *Journal of Optics A: Pure and Applied Optics*, 1(6):662–667, November 1999.

[41] S Couris, M Renard, O Faucher, B Lavorel, R Chaux, E Koudoumas, and X Michaut. An experimental investigation of the nonlinear refractive index (n2) of carbon disulfide and toluene by spectral shearing interferometry and z-scan techniques. *Chemical Physics Letters*, 369(3-4):318–324, February 2003.

[42] Robert W. Boyd. *Nonlinear Optics*. Academic Press, Inc., 3rd edition, 2008.

[43] M Sheik-Bahae, David J Hagan, and Eric W Van Stryland. Dispersion and band-gap scaling of the electronic kerr effect in solids associated with two-photon absorption. *Physical review letters*, 65(1):96, 1990.

[44] Yangjian Cai, Xuanhui Lu, and Qiang Lin. Hollow Gaussian beams and their propagation properties. *Optics Letters*, 28(13):1084, July 2003.

[45] N. Apurv Chaitanya, M. V. Jabir, Jagannath Banerji, and Goutam Kumar Samanta. Hollow Gaussian beam generation through nonlinear interaction of photons with orbital angular momentum. *Scientific reports*, 6(1):32464, 2016.

[46] Sabir Ul Alam, Niraj Kumar Soni, A. Srinivasa Rao, Hongsen He, Yu-Xuan Ren, and Kenneth K. Y. Wong. Two-photon microscopy with enhanced resolution and signal-to-background ratio using hollow Gaussian beam excitation. *Optics Letters*, 47(8):2048, April 2022.

[47] Jingyan Zhan, Denghui Li, Domenico Bongiovanni, Yinxiao Xiang, Shengyao Chen, Yujie Zhang, Liqin Tang, Daohong Song, Jianke Yang, Roberto Morandotti, and Zhigang Chen. Nonlinear generation of hollow beams in tunable plasmonic nanosuspensions. *APL Photonics*, 8(7):076102, July 2023.

[48] M. S. Soskin, V. N. Gorshkov, M. V. Vasnetsov, J. T. Malos, and N. R. Heckenberg. Topological charge and angular momentum of light beams carrying optical vortices. *Physical Review A*, 56(5):4064–4075, November 1997.

[49] I.V. Basistiy, M.S. Soskin, and M.V. Vasnetsov. Optical wavefront dislocations and their properties. *Optics Communications*, 119(5-6):604–612, September 1995.

[50] Zhengjun Liu, Haifa Zhao, Jianlong Liu, Jie Lin, Muhammad Ashfaq Ahmad, and Shutian Liu. Generation of hollow Gaussian beams by spatial filtering. *Optics Letters*, 32(15):2076, August 2007.

[51] Jianping Yin, Weijian Gao, and Yifu Zhu. Generation of dark hollow beams and their applications. In *Progress in Optics*, volume 45, pages 119–204. Elsevier, 2003.

[52] L. Mandel. Complex Representation of Optical Fields in Coherence Theory*. *Journal of the Optical Society of America*, 57(5):613, May 1967.

[53] Samuel N. Alperin, Robert D. Niederriter, Juliet T. Gopinath, and Mark E. Siemens. Quantitative measurement of the orbital angular momentum of light with a single, stationary lens. *Optics Letters*, 41(21):5019–5022, November 2016.

[54] Vladimir Denisenko, Vladlen Shvedov, Anton S. Desyatnikov, Dragomir N. Neshev, Wieslaw Krolikowski, Alexander Volyar, Marat Soskin, and Yuri S. Kivshar. Determination of topological charges of polychromatic optical vortices. *Optics Express*, 17(26):23374, December 2009.

[55] Lihong V Wang. Multi-stage Stern–Gerlach experiment modeled. *Journal of Physics B: Atomic, Molecular and Optical Physics*, 56(10):105001, May 2023.

[56] Wentao Yu, Ziheng Ji, Dashan Dong, Xusan Yang, Yunfeng Xiao, Qihuang Gong, Peng Xi, and Kebin Shi. Super-resolution deep imaging with hollow Bessel beam STED microscopy. *Laser & Photonics Reviews*, 10(1):147–152, January 2016.

Chapter 5

Tunability of synthetic fields in third order nonlinear process

5.1 Introduction

Particle spin dynamics provides one of the richest frameworks for exploring quantum geometry and its manifestations [1]. Fundamentally, the relativistic formalism of quantum mechanics by Dirac necessitated the existence of spin and its dynamical interaction in presence of magnetic field [2]. The unwitting first experimental evidence of spin was revealed through the famous Stern-Gerlach experiment [3, 4] which is followed by innumerable tests on this degree of freedom [5, 6, 7]. In condensed-matter physics, spin-dynamics and its geometrical interpretation forms the foundational principles of *spintronic* devices [8, 9]. Such configurations are indispensable ingredients of non-volatile magnetic random access memory (MRAM) [10], magnetometers [11], automotive braking systems [12], and racetrack memory [13], with significant applications in perimeter defense systems [14]. Scattering-immune spin transport via the creation of topologically non-trivial spin texture would lead to topological Hall effect (THE) [15, 16, 17] and by leveraging its features, the next generation of spintronic devices is expected to exhibit a significant reduction in power consumption and improved device functionalities [18, 19].

The existence of topologically non-trivial particles such as *optical Skyrmions* and the discovery of the optical analogue of spin Hall effect (SHE) facilitate greater control of the *pseudo*-spin transport mechanism via tuning suitable optical degree of freedom [20, 21, 22, 23, 24, 25]. The geometric character in polarization optics is introduced via adopt-

ing suitable gauge symmetries in the paraxial dynamics in optically birefringent systems [26]. By virtue of the fact that nonlinear optical configurations exhibit perturbative dynamics naturally, they provide a fertile ground for exploring geometrical manifestations and topological connections in photonics. In a seminal work by Karnieli *et al.*, an equivalence was drawn between a $\chi^{(2)}$-based frequency conversion process (in *frequency-state* basis) and the dynamics of a spin-$\frac{1}{2}$ particles in a synthetic magnetizing field [27]. Such an equivalence paves the route for developing analogous all-optical spintronic functionalities such as the *Giant Magneto Resistance* (GMR) effect as well as the creation of topologically non-trivial 3D magnetization textures [28]. It is worthwhile to note that an all-optical setting for topology-assisted *pseudo*-spin transport exhibits a unique feature in terms of extremely broad operational bandwidth. An integrated photonics based approach further facilitates preserving the state fidelity (low coupling losses) and hence, high signal-to-noise ratio [29, 30]. Amongst the broad category of nonlinear optical processes, $\chi^{(3)}$-led self-action and four-wave mixing (FWM) effects are the most prevalent. In particular, the dynamics of self-action effects, such as self-focusing [31] and filamentation [32], tend to exhibit intricate topologically non-trivial manifestations, which are revealed through complex spatial beam structures [33, 34, 35]. In this article, we present an analogous SHE in a $\chi^{(3)}$-mediated nonlinear optical interaction. The pump-probe based experimental measurements reveal the existence of *pseudo*-spin basis modes which exhibit a symmetric transverse separation in presence of an 'experimentally-controllable' all-optical gauge-field. Through an analytical formalism, we show that a spatial asymmetry in the pump laser beam leads to non-trivial, gauge-dictated, synthetic magnetization textures which is responsible for probe beam splitting, thereby an analogous all-optical SHE. Interestingly, the dynamical interaction adheres to a $\mathcal{PT}$-symmetric non-Hermitian system that exhibits a real-valued eigenvalue spectrum [36, 37, 38] for $\chi^{(3)} < 0$. Overall, the results derive their novelty via the demonstration for proof-of-principle extension of SHE-like dynamics to non-Hermitian interactions.

5.2 Theoretical Formulation for $\chi^{(3)}$ dynamics

We also start here with the same recipe as described before. We consider the propagation of a strong light beam at frequency ω_p along z direction in a $\chi^{(3)}$ nonlinear medium. In scalar approximation, we define $|\psi_p\rangle = \frac{1}{2}\left[a_p(\vec{r})e^{i(\omega_p t - k_p z)} + c.c\right]$ where k_p is the wavevector of the beam. The strong pump beam spontaneously generates two co-propagating fields *viz.* $|\psi_+\rangle$ and $|\psi_-\rangle$ which are governed by the linearized nonlinear Schrödinger's equation (NLSE) in the paraxial framework and is given by [39],

$$\nabla_T^2 a_+ + 2ik_p\frac{\partial a_+}{\partial z} = -\frac{6\chi^{(3)}\omega_p^2}{c^2}|a_p|^2 a_+ - \frac{3\chi^{(3)}\omega_p^2}{c^2}a_p^2 e^{2i\Phi}a_-^* \tag{5.1}$$

$$\nabla_T^2 a_- + 2ik_p\frac{\partial a_-}{\partial z} = -\frac{6\chi^{(3)}\omega_p^2}{c^2}|a_p|^2 a_- - \frac{3\chi^{(3)}\omega_p^2}{c^2}a_p^2 e^{2i\Phi}a_+^* \tag{5.2}$$

Here we have defined $|\psi_\pm\rangle = \frac{1}{2}\left[a_\pm(\vec{r})e^{i(\omega_p t - k_p z)} + c.c\right]$. The z-independent Hamiltonian depicted through dynamical Eqs. are expressed as [40, 27]

$$i\frac{\partial}{\partial z}|\Psi'\rangle = \left[\frac{(\vec{p}_T - \vec{\mathcal{A}})^2}{2\bar{m}} - \vec{\sigma}\cdot\vec{\mathcal{M}}\right]|\Psi'\rangle = \hat{H}\,|\Psi'\rangle \tag{5.3}$$

where $|\Psi'\rangle = U^\dagger(a_+\ a_-^*)^T$ defines the spinor in rotated frame. $\vec{p}_T = -i\vec{\nabla}_T = -i(\hat{x}\frac{\partial}{\partial x} + \hat{y}\frac{\partial}{\partial y})$ is the equivalent momentum operator, $\bar{m} = k_p\sigma_z$ is equivalent mass operator and $\vec{\sigma} \equiv [\sigma_x, \sigma_y, \sigma_z]$ is the triad of Pauli spin matrices. $\vec{\mathcal{A}} = -\vec{\nabla}_T\Phi\sigma_z$ is gauge-dictated magnetic vector potential, $\vec{\mathcal{M}} = \mathcal{M}_0\hat{\mathcal{M}} = \Omega\sin(2\varphi)e^{-i(2m+1)\pi/2}\hat{x} + \Omega\cos(2\varphi)e^{i(2m+1)\pi/2}\hat{y} + (k_p + \Omega)\hat{z}$ is the synthetic magnetization created by the pump beam where $\Omega = \frac{\omega_p}{c}n_2 I_p = \frac{3\chi^{(3)}\omega_p^2}{2k_p c^2}|\mathbb{A}_0|^2$ and $a_p = \mathbb{A}_0 e^{i\varphi(x,y)}$ (where φ is real). It is worth pointing out that the dynamical evolution of eigenmodes $|\Psi'_\pm\rangle$ states as depicted by $\hat{H}$ has a non-Hermitian character

with a broken anti-$\hat{P}\hat{T}$-symmetry for any $\chi^{(3)} < 0$ [40]. It is important to note that synthetic magnetic field is absent due to trivial nature of synthetic magnetic potential.

$$\vec{\mathbb{B}} = \vec{\nabla}_T \times \vec{\mathcal{A}} = -\vec{\nabla}_T \times \vec{\nabla}_T \Phi \sigma_z = 0 \tag{5.4}$$

From an alternative perspective, the approach provides a platform for realizing complex all-optical synthetic magnetization textures $\left(\vec{\mathcal{M}}(x,y)\right)$ via altering the structural symmetry of the pump beam. The propagation of *pseudo*-spin states ($|\Psi'_{\pm}\rangle$) through the created magnetization textures could be precisely controlled in space that is reflected through restructuring of probe beam. Eq. (5.3), therefore, provides a broad framework for exploring a quantum two-level dynamics in a purely classical $\chi^{(3)}$-led self-action effect. In order to reveal the impact of this approach, we use a transformation $|\Psi'\rangle = \mathbb{P}\,|\Psi''\rangle$ which essentially aligns the local magnetization direction ($\hat{\mathcal{M}}$) along $\hat{z}$ where $\mathbb{P}$ is defined as

$$\mathbb{P} = \cos\frac{\theta}{2}\mathbb{I} - i\sin\frac{\theta}{2}(\vec{\sigma}\cdot\hat{\phi}) = exp\left(-i\frac{\theta}{2}\vec{\sigma}\cdot\hat{\phi}\right) \tag{5.5}$$

where $\theta = \cos^{-1}(\hat{\mathcal{M}}\cdot\hat{z})$ is polar angle and $\phi = \tan^{-1}(\mathcal{M}_y/\mathcal{M}_x)$ is azimuthal angle with $\mathbb{I}$ defining the 2×2 identity operation. By following an identical recipe, Eq. (5.3) transforms to

$$i\frac{\partial}{\partial z}|\Psi''\rangle = \left[\frac{(\vec{p}_T - \vec{\mathcal{A}}')^2}{2\bar{m}} + V\right]|\Psi''\rangle \tag{5.6}$$

where, the transformed gauge-dictated vector and scalar potentials in new reference frame are

$$\begin{aligned} V &= -i\mathbb{P}^{\dagger}\frac{\partial}{\partial z}\mathbb{P} - \mathcal{M}_0\sigma_z \\ \vec{\mathcal{A}}' &= i\mathbb{P}^{\dagger}\vec{\nabla}_T\mathbb{P} + \mathbb{P}^{\dagger}\vec{\mathcal{A}}\mathbb{P} \end{aligned} \tag{5.7}$$

Here, $|\Psi''_{\pm}\rangle$ constitute the eigenmodes of the dynamical system (given by Eq. (5.6)) which are identical to spinor in 'two-level' quantum systems. In this rotated frame, we only consider terms proportional to σ_z and in the adiabatic limit, the transformed potentials turn out to be [41, 27]

$$\begin{aligned} V &= -\mathcal{M}_0\sigma_z \\ \vec{\mathcal{A}}' &= \{\cos\theta\,\vec{\nabla}_T(\phi/2-\Phi)\}\sigma_z - \frac{\vec{\nabla}_T\phi}{2}\sigma_z \end{aligned} \tag{5.8}$$

Consequently, the synthetic magnetic field ($\vec{\mathcal{B}}$) is the transformed frame is expressed as

$$\vec{\mathcal{B}} = \vec{\nabla}_T \times \vec{\mathcal{A}}' = \{\vec{\nabla}_T\cos\theta \times \vec{\nabla}_T(\phi/2-\Phi)\}\sigma_z \tag{5.9}$$

By comparing $\hat{\mathcal{M}}$ with a unit vector ($\hat{n}$) in cartesian coordinates $\hat{n} = \sin\theta\cos\phi\;\hat{x} + \sin\theta\sin\phi\;\hat{y} + \cos\theta\;\hat{z}$, we obtain $\cos\theta = \frac{\mathcal{M}_z}{\mathcal{M}_0} = \frac{\Omega+k_p}{\mathcal{M}_0}$ where $\mathcal{M}_0 = \sqrt{k_p^2+2k_p\Omega}$. In the first step, we evaluate the second term of Eq. (5.9) after decomposition,

$$\begin{aligned} \vec{\nabla}_T\cos\theta\times\vec{\nabla}_T\Phi &= \vec{\nabla}_T\left(\frac{\mathcal{M}_z}{\mathcal{M}_0}\right)\times\vec{\nabla}_T\int\Omega\,dz' \\ &= \left[\frac{1}{\mathcal{M}_0}\vec{\nabla}_T\Omega - \frac{k_p\mathcal{M}_z}{\mathcal{M}_0^3}\vec{\nabla}_T\Omega\right]\times\int\vec{\nabla}_T\Omega\,dz' \\ &= \frac{k_p\Omega}{\mathcal{M}_0^3}\vec{\nabla}_T\Omega\times\int\vec{\nabla}_T\Omega\,dz' = 0 \end{aligned} \tag{5.10}$$

Therefore, $\vec{\mathcal{B}}$ is essentially determined from the first term which is estimated to be

$$\begin{aligned}\vec{\mathcal{B}} = \vec{\nabla}_T \times \vec{\mathcal{A}}' &= -\left(\frac{k_p\Omega}{\mathcal{M}_0^3}\vec{\nabla}_T\Omega \times \vec{\nabla}_T\varphi\right)\sigma_z \\ &= -\frac{1}{2}\hat{z}\left[\hat{\mathcal{M}}\cdot\left(\frac{\partial\hat{\mathcal{M}}}{\partial x}\times\frac{\partial\hat{\mathcal{M}}}{\partial y}\right)\right]\end{aligned} \tag{5.11}$$

where, we have taken $\phi = \frac{\pi}{2} - 2\varphi$. The synthetic electric field ($\vec{\mathcal{E}}$) is defined as

$$\begin{aligned}\vec{\mathcal{E}} &= -\vec{\nabla}_T V - \frac{\partial\vec{\mathcal{A}}'}{\partial z} \\ &= \vec{\nabla}_T\mathcal{M}_0\sigma_z - \frac{\partial}{\partial z}\left\{\cos\theta\,\vec{\nabla}_T(\phi/2-\Phi) - \frac{\vec{\nabla}_T\phi}{2}\right\}\sigma_z \\ &= \vec{\nabla}_T\mathcal{M}_0\sigma_z - \frac{\partial}{\partial z}\left(\frac{\mathcal{M}_z}{\mathcal{M}_0}\right)\vec{\nabla}_T(\phi/2-\Phi)\sigma_z - \left(\frac{\mathcal{M}_z}{\mathcal{M}_0}\right)\vec{\nabla}_T\frac{\partial}{\partial z}(\phi/2-\Phi)\sigma_z + \frac{1}{2}\vec{\nabla}_T\frac{\partial}{\partial z}\phi \\ &= \vec{\nabla}_T\mathcal{M}_0\sigma_z - \frac{k_p\Omega}{\mathcal{M}_0^3}\frac{\partial\Omega}{\partial z}\vec{\nabla}_T(\phi/2-\Phi)\sigma_z + \left(\frac{\mathcal{M}_z}{\mathcal{M}_0}\right)\vec{\nabla}_T\Omega\sigma_z \\ \vec{\mathcal{E}} &= \left[\vec{\nabla}_T\mathcal{M}_0 + \left(\frac{\mathcal{M}_z}{\mathcal{M}_0}\right)\vec{\nabla}_T\Omega + \frac{k_p\Omega}{\mathcal{M}_0^3}\frac{\partial\Omega}{\partial z}\vec{\nabla}_T(\varphi+\Phi)\right]\sigma_z\end{aligned} \tag{5.12}$$

Equation (5.11) clearly indicates that $\vec{\mathcal{B}}$ is purely dictated by transverse variation of synthetic magnetization $\vec{\mathcal{M}}$. In Cartesian coordinates, $\vec{\mathcal{B}}$ takes the following form

$$\vec{\mathcal{B}} = -\hat{z}\frac{k_p\Omega}{\mathcal{M}_0^3}\left(\frac{\partial\Omega}{\partial x}\frac{\partial\varphi}{\partial y} - \frac{\partial\Omega}{\partial y}\frac{\partial\varphi}{\partial x}\right)\sigma_z \tag{5.13}$$

which clearly depicts that $\vec{\mathcal{B}}$ depends on pump beam profile only. As an example, we consider a Gaussian pump beam of beam waist w and radius of curvature R which is expressed as

$$a_p^{(G)} = \mathbb{A}_0\, exp\left(-\frac{x^2+y^2}{w^2}\right)\, exp\left(-ik_p\frac{x^2+y^2}{R}\right) \tag{5.14}$$

This would readily give us $\varphi = k_p\left(\frac{x^2+y^2}{R}\right)$ and coupling factor turns out

$$\begin{aligned}\Omega &= \frac{3\chi^{(3)}\omega_p^2}{2k_pc^2}|\mathbb{A}_0|^2 = \frac{3\chi^{(3)}\omega_p^2}{2k_pc^2}|\widetilde{\mathbb{A}}_0|^2\ exp\left(-2\frac{x^2+y^2}{w^2}\right)\\ &= \Omega_0\ exp\left(-2\frac{x^2+y^2}{w^2}\right)\end{aligned}$$

Upon simplification,

$$\begin{aligned}\vec{\mathcal{B}} &= -\hat{z}\frac{k_p\Omega}{\mathcal{M}_0^3}\left(\frac{\partial\Omega}{\partial x}\frac{\partial\varphi}{\partial y} - \frac{\partial\Omega}{\partial y}\frac{\partial\varphi}{\partial x}\right)\sigma_z\\ &= -\hat{z}\frac{k_p\Omega}{\mathcal{M}_0^3}\left[\Omega\left(-\frac{4x}{w^2}\right)\frac{2k_py}{R} - \Omega\left(-\frac{4y}{w^2}\right)\frac{2k_px}{R}\right]\sigma_z\\ \vec{\mathcal{B}} &= 0\end{aligned} \tag{5.15}$$

It is now clear from Eq. (5.11) that a Gaussian pump beam $\left(a_p^{(G)} \sim e^{-\frac{r^2}{w_p^2}}\right)$ manifests into $\vec{\mathcal{B}} = 0$ in any frame of reference. On the other hand, a spatial asymmetry in the pump beam structure gives rise to the possibility of topological bands. We adopt a simple route for breaking radial symmetry in the pump beam by considering an elliptic Gaussian (EG) pump beam which is expressed as

$$a_p^{(EG)} = \mathbb{A}_0\ exp\left(-\frac{x^2}{w_x^2} - \frac{y^2}{w_y^2}\right)\ exp\left(-ik_p\frac{x^2}{R_x} - ik_p\frac{y^2}{R_y}\right) \tag{5.16}$$

where $[w_x,\ w_y]$ and $[R_x,\ R_y]$ are beam waists and radius of curvatures along $\hat{x}$ and $\hat{y}$ directions respectively. This would lead to $\varphi = \frac{k_px^2}{R_x} + \frac{k_py^2}{R_y}$ and $\Omega = \Omega_0\ e^{\left(-\frac{2x^2}{w_x^2}-\frac{2y^2}{w_y^2}\right)}$ with $\Omega_0 = \frac{3\chi^{(3)}\omega_p^2}{2k_pc^2}|\widetilde{\mathbb{A}}_0|^2$.

$$\begin{aligned}\vec{\mathcal{B}} &= -\hat{z}\frac{k_p\Omega}{\mathcal{M}_0^3}\left(\frac{\partial\Omega}{\partial x}\frac{\partial\varphi}{\partial y}-\frac{\partial\Omega}{\partial y}\frac{\partial\varphi}{\partial x}\right)\sigma_z \\ &= -\hat{z}\frac{k_p\Omega}{\mathcal{M}_0^3}\left[\Omega\left(-\frac{4x}{w_x^2}\right)\frac{2k_py}{R_y}-\Omega\left(-\frac{4y}{w_y^2}\right)\frac{2k_px}{R_x}\right]\sigma_z \\ &= \hat{z}\frac{k_p^2\Omega^2}{\mathcal{M}_0^3}8xy\left(\frac{1}{w_x^2R_y}-\frac{1}{w_y^2R_x}\right)\sigma_z\end{aligned} \tag{5.17}$$

For our experimental condition and at optical frequencies, it is safe to assume $\mathcal{M}_0 = \sqrt{k_p^2+2k_p\Omega} \approx k_p$. So, our magnetic field becomes

$$\vec{\mathcal{B}} \approx (-\hat{z})\frac{8\Omega^2}{k_p}xy\left(\frac{1}{w_y^2R_x}-\frac{1}{w_x^2R_y}\right)\sigma_z \tag{5.18}$$

which represents a massive fermion dynamics. By virtue of non-zero $\vec{\mathcal{B}}$, the Lorentz force on probe photons will be,

$$
\begin{aligned}
\vec{\mathcal{F}} &= q_e(\vec{v}_T \times \vec{\mathcal{B}}) = \frac{q_e}{\bar{m}}(\vec{p}_T \times \vec{\mathcal{B}}) \\
&= -\frac{iq_e}{\bar{m}}(\vec{\nabla}_T \times \vec{\mathcal{B}}) \\
&= -\frac{iq_e}{k_p\sigma_z}\left[\left(\hat{x}\frac{\partial}{\partial x} + \hat{y}\frac{\partial}{\partial y}\right) \times \hat{z}\frac{8\Omega^2}{k_p}xy\left(\frac{1}{w_x^2 R_y} - \frac{1}{w_y^2 R_x}\right)\sigma_z\right] \\
&= -\frac{i8q_e}{k_p^2}\left(\frac{1}{w_x^2 R_y} - \frac{1}{w_y^2 R_x}\right)\Omega_0^2\left[\left(\hat{x}\frac{\partial}{\partial x} + \hat{y}\frac{\partial}{\partial y}\right) \times \left(e^{\left(-\frac{4x^2}{w_x^2}-\frac{4y^2}{w_y^2}\right)}xy\right)\hat{z}\right] \\
&= -\frac{i8q_e}{k_p^2}\left(\frac{1}{w_x^2 R_y} - \frac{1}{w_y^2 R_x}\right)\Omega_0^2 e^{\left(-\frac{4x^2}{w_x^2}-\frac{4y^2}{w_y^2}\right)}\left[\left(y - \frac{8x^2 y}{w_x^2}\right)(-\hat{y}) + \left(x - \frac{8xy^2}{w_y^2}\right)\hat{x}\right] \\
&= -\frac{i8q_e}{k_p^2}\left(\frac{1}{w_x^2 R_y} - \frac{1}{w_y^2 R_x}\right)\Omega_0^2 e^{\left(-\frac{4x^2}{w_x^2}-\frac{4y^2}{w_y^2}\right)}\left[x\left(1 - \frac{8y^2}{w_y^2}\right)\hat{x} - y\left(1 - \frac{8x^2}{w_x^2}\right)\hat{y}\right] \\
&= \kappa_0 e^{\left(-\frac{4x^2}{w_x^2}-\frac{4y^2}{w_y^2}\right)}\left[x\left(1 - \frac{8y^2}{w_y^2}\right)\hat{x} - y\left(1 - \frac{8x^2}{w_x^2}\right)\hat{y}\right]
\end{aligned}
\tag{5.19}
$$

where $\kappa_0 = \frac{8iq_e\Omega_0^2}{k_p^2}\left(\frac{1}{w_y^2 R_x} - \frac{1}{w_x^2 R_y}\right)$. Here, $q_e = \pm 1$ is the emergent charge corresponding to each pseudo-spin basis constituting the probe beam and bears a sign determined by pseudo-spin orientation with respect to the local magnetization ($\vec{\mathcal{M}}$) axis. We consider elliptic Gaussian beam with ellipticity $e_p = 0.10,\ 0.60,\ 0.88$ as shown in Fig. 5.1(a)-(c), where $e_p = 1 - \frac{w_x}{w_y}$. Corresponding to this, we present the force field distribution $\left(\frac{\vec{\mathcal{F}}}{\kappa_0}\right)$ in Fig. 5.1(d)-(f). It is apparent that $|\vec{\mathcal{F}}|$ exerts an azimuthally symmetric force on eigenmodes ($|\Psi'\rangle$) when pump has small ellipticity ($e_p = 0.10$). An increase in pump beam ellipticity results in $|\vec{\mathcal{F}}|$ localized close to y-axis and directed in $\pm x$-direction. Therefore, it is expected that the two eigenmodes $|\Psi'_{\pm}\rangle$ (in Eq. 5.6) would localize in the $x-y$ plane away from the y-axis. In addition, the magnitude of $\vec{\mathcal{F}}$ monotonically increases as a function of pump power and therefore, the impact of pump beam ellipticity would exemplify more at higher pump

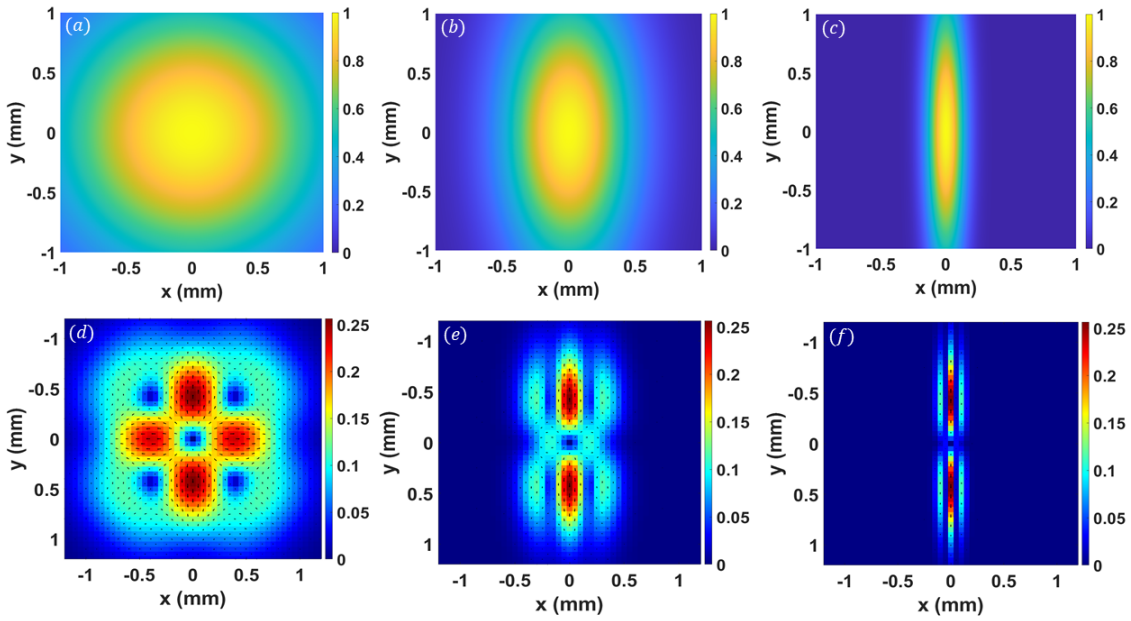

Figure 5.1: (a)-(c) represents elliptic pump beam profiles for $w_y = 1200\ \mu m$ and $w_x = 1100\ \mu m,\ 500\ \mu m,\ 150\ \mu m$ corresponding to ellipticity of 0.90 (a), 0.40 (b), 0.12 (c) respectively. (d)-(f) represents a force field $\left(|\vec{\mathcal{F}}|\right)$ intensity map for pump beam with ellipticity of 0.90 (a), 0.40 (b), 0.12 (c) respectively.

powers. In order to gain a deeper insight, we solved Eq. (5.6) numerically via beam propagation method and used experimental values of physical quantities which are described in the next section. By considering two examples where $w_x = 500\ \mu m,\ w_y = 1200\ \mu m$ and $w_x = 150\ \mu m,\ w_y = 1200\ \mu m$ for the nonlinear medium of length T, we simulated the probe beam profile at the exit face ($z = +\frac{T}{2}$) at different values of incident pump powers (P_p) and shown in Fig. 5.2(a)-(d) and Fig. 5.2(e)-(h) respectively. A comparison between Fig. 5.2(a)-(d) and Fig. 5.2(e)-(h) shows that the probe beam distortion is elucidated more when pump beam ellipticity is high. Also, the probe beam distorts more at higher pump powers for a given pump ellipticity. The conclusions drawn from the simulated $\vec{\mathcal{F}}$ in Fig. 5.1(d)-(f) predict a similar variation in the transmitted probe beam. In fact, there is a distinct appearance of two lobes in the simulated probe beam for the pump beam ellipticity of

0.88 (for $P_p = 500\ mW$) and the centroids of the two lobes are separated by $\approx 0.16\ mm$ at $z = \pm\frac{T}{2}$. Alternately, this could be viewed as asymmetric Lorentz force experienced by the photons in the eigenmodes $|\Phi'_{\pm}\rangle$ and consequently, they are scattered to redistribute in a pattern as shown in Fig. 5.2(h). Such a dynamics is analogous to scattering of *spin* (or superposed *spin*) states in an inhomogeneous (real) magnetic field [15, 16]. In resemblance, the scattering of photons in analogous spinor ($|\Phi'_{\pm}\rangle$) basis is essentially due to synthetic magnetic field ($\vec{\mathcal{B}}$) led Lorentz force.

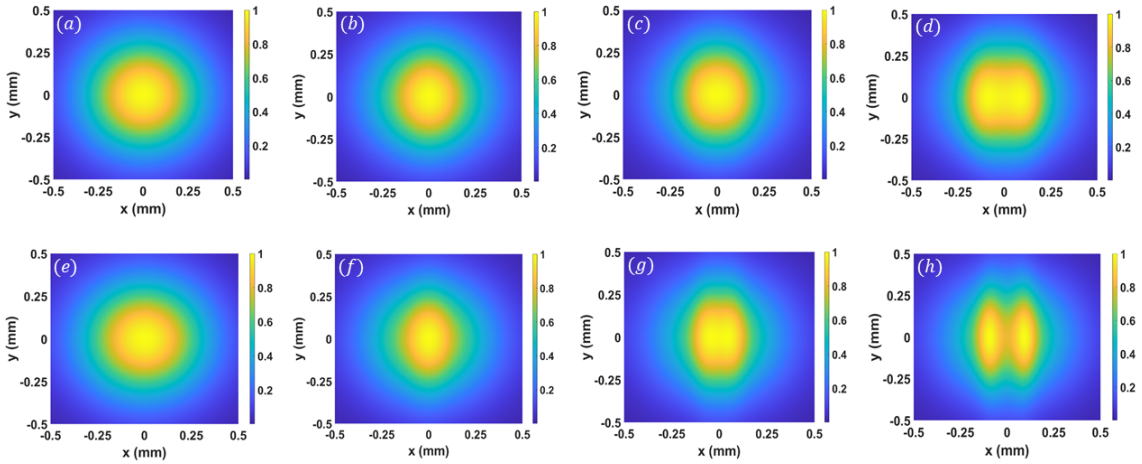

Figure 5.2: (a)-(d) represents simulated probe beam profiles at the exit face nonlinear medium ($z = +\frac{T}{2}$) for $w_x = 500\ \mu m$ and $w_y = 1200\ \mu m$ at average pump beam power of (a) $30\ mW$, (b) $150\ mW$, (c) $300\ mW$, (d) $500\ mW$ respectively. (e)-(h) represents simulated probe beam profiles at the exit face nonlinear medium ($z = +\frac{T}{2}$) for $w_x = 150\ \mu m$ and $w_y = 1200\ \mu m$ at average pump beam power of (a) $30\ mW$, (b) $150\ mW$, (c) $300\ mW$, (d) $500\ mW$ respectively.

Since, a geometric interpretation of $\vec{\mathcal{E}}$ is hinged on z-dependence of $\vec{\mathcal{A}}'$ ($\propto\ \Omega$), we focus on $\vec{\mathcal{B}}$ which could lead to geometric phases being acquired by the optical state $|\Psi''\rangle$. Hence, the transmitted probe beam will acquire a geometric phase in presence of a non-vanishing

$\vec{\mathcal{B}}$ field which is given by

$$\begin{aligned}\Theta^{(EG)} &= \frac{1}{2\pi}\iint_S \vec{\mathcal{B}}\cdot d\vec{S} \\ &= \frac{4}{\pi k_p}\left(\frac{1}{w_x^2 R_y}-\frac{1}{w_y^2 R_x}\right)\iint_S \Omega^2 xy\, dx\, dy \\ &= \frac{4}{\pi k_p}\left(\frac{1}{w_x^2 R_y}-\frac{1}{w_y^2 R_x}\right)\Omega_0^2\iint_S e^{-\left(\frac{4x^2}{w_x^2}+\frac{4y^2}{w_y^2}\right)} xy\, dx\, dy\end{aligned} \tag{5.20}$$

In order to simplify Eq. (5.20), we choose polar coordinates *i.e.* $x = \rho\cos\frac{\phi}{n}$ and $y = \rho\sin\frac{\phi}{n}$ where n defines the number of symmetry axis in $\vec{\mathcal{B}}(x,y)$. In case of an elliptic pump beam, $n = 2$ by virtue of an inherent two-fold spatial symmetry-axis. Therefore, for $\rho = 0 \rightarrow \rho = \infty$, Eq. (5.20) turns out

$$\begin{aligned}\Theta^{(EG)} &= \frac{4\Omega_0^2}{\pi k_p}\left(\frac{1}{w_x^2 R_y}-\frac{1}{w_y^2 R_x}\right)\iint_S e^{-4\rho^2\left(\frac{\cos^2(\phi/2)}{w_x^2}+\frac{\sin^2(\phi/2)}{w_y^2}\right)}\rho\cos\left(\frac{\phi}{2}\right)\rho\sin\left(\frac{\phi}{2}\right)\rho\, d\rho\, d\phi \\ &= \frac{2\Omega_0^2}{\pi k_p}\left(\frac{1}{w_x^2 R_y}-\frac{1}{w_y^2 R_x}\right)\int_{\phi_1}^{\phi_2}\int_{\rho=0}^{\infty} e^{-4\rho^2\left(\frac{\cos^2(\phi/2)}{w_x^2}+\frac{\sin^2(\phi/2)}{w_y^2}\right)}\rho^3\, d\rho\sin\phi\, d\phi \\ &= \frac{\Omega_0^2}{32\pi k_p}\left(\frac{1}{w_x^2 R_y}-\frac{1}{w_y^2 R_x}\right)\int_{\phi_1}^{\phi_2}\frac{\sin(\phi)}{\alpha(\phi)^2}\, d\phi\end{aligned} \tag{5.21}$$

where $\alpha(\phi) = \frac{\cos^2\left(\frac{\phi}{2}\right)}{w_x^2}+\frac{\sin^2\left(\frac{\phi}{2}\right)}{w_y^2}$. This has a zero contribution to the integration in Eq. (5.21) when ϕ goes from $\phi_1 = 0 \rightarrow \phi_2 = 2\pi$. Therefore, $\Theta_+^{(EG)} = \theta_0$ when $\phi_1 = 0 \rightarrow \phi_2 = \pi$ and $\Theta_-^{(EG)} = -\theta_0$ when $\phi_1 = \pi \rightarrow \phi_2 = 2\pi$ respectively. In other words, the light transport dynamics results in acquiring quantized geometric phase (of opposite polarity) by the spinors $|\Psi'_\pm\rangle$. The two lobes, which are the two eigenmodes $|\Psi'_\pm\rangle$ in Eq. (5.6), constitute two distinguishable bands (in real space) and the gap between the lobes (or

bands) is governed by pump laser intensity. This is reminiscent of a spin-Hall effect (SHE) in an all-optical configuration where the synthetic magnetization texture is created by the pump beam.

5.3 Experimental methods

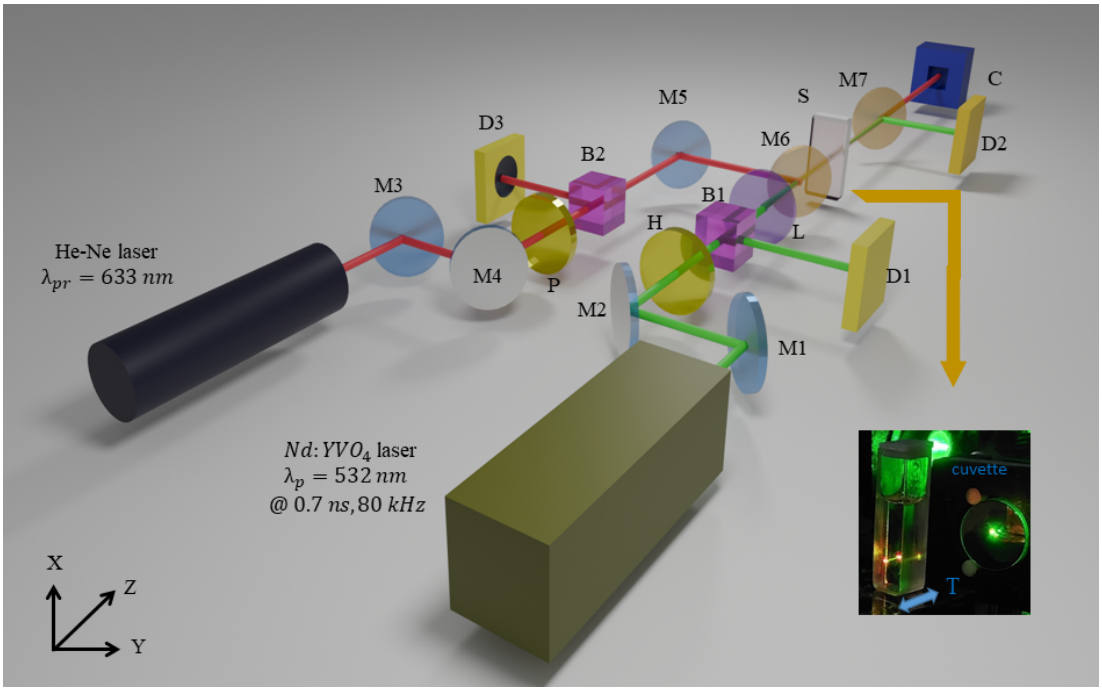

Figure 5.3: shows the collinear pump-probe based experimental configuration for observing topological Hall effect (THE) in an asymmetric synthetic magnetic field ($\vec{\mathcal{B}}$). B1: Polarizing beam-splitter; B2: Non-polarizing beam-splitter; S: sample; D1-D3: Power meter; H: Half-wave plate; P: Polarizer; M1-M5: Steering mirror; M6 & M7: Dichroic mirrors for realizing collinear arrangement; L: cylindrical lens; C: CCD camera. *Inset*: $T = 1\ cm$ thick cuvette filled with toluene that exhibits $\chi^{(3)} < 0$ (defocusing) for $700\ ps$ pulsed laser centered at $532\ nm$ wavelength.

The experimental configuration is a collinear pump-probe setup realized using a frequency doubled $Nd : YVO_4$ pulsed laser delivering pulses of $\sim 1\ ns$ width at $532\ nm$ central wavelength acting as a pump beam. The pump pulses are linearly polarized TEM_{00} Gaussian profile. A combination of half wave plate (HWP) and polarizing beam splitter

(PBS) is used for controlling the incident pump power. The pump beam passes through a plano-convex cylindrical lens (CL) of appropriate focal length (f) which creates an elliptic beam profile at the focus. The beam ellipticity and dimensions are estimated using a knife-edge based scanning beam profiler (NanoScan, Ophir, USA). We used an organic solvent *toluene* as a nonlinear medium which was housed in a $T = 1\ cm$ thick cuvette and positioned at the pump beam focus ($z = 0$) such that the laser beam entry and exit faces are given by $z = \pm\frac{T}{2}$. The probe beam is a beam from $He - Ne$ laser ($633\ nm$ wavelength) which is different from the pump wavelength. The choice of detuned probe beam is motivated by the realization of a collinear pump-probe configuration (using a dichroic mirror) as shown in Fig. (5.3). In such a scenario, it appears that the nonlinear polarization ($P^{(3)}$) contains two distinguishable frequency components ω_{pr} and $(2\omega_p - \omega_{pr})$ where ω_{pr} is the angular frequency of probe beam. However, it is to be noted that $\omega_p - \omega_{pr} << \frac{\omega_{pr}}{2}$ in the present case. This ensures dominant nonlinear polarization to oscillate at ω_{pr} and consequently, the error involved in assuming identical $\chi^{(3)}$ for diagonal and off-diagonal terms in Eqs. (5.1) and (5.2) is negligible [39, 42]. Another dichroic mirror was employed to separate the two beams. A CCD camera of the pixel size of $4.4\ \mu m \times 4.4\ \mu m$ (GRAS 2.0, Point Grey, USA) was used for recording the probe beam structure and it was positioned at a distance $\approx 30\ cm$ from the cuvette.

5.4 Results and Discussion

In order to carry out the experimental investigation, we used CL of focal length $f = 500\ mm$ which resulted in pump beam waist of $w_x \approx 500\ \mu m$ and $w_y \approx 1200\ \mu m$. Figure 5.4(a)-(d) shows the recorded probe beam structure at different pump power (P_p) levels. It is apparent that the transmitted probe beam undergoes a nominal asymmetric distortion when average incident pump power changes from $P_p = 30\ mW$ to $P_p = 500\ mW$. This could be qualita-

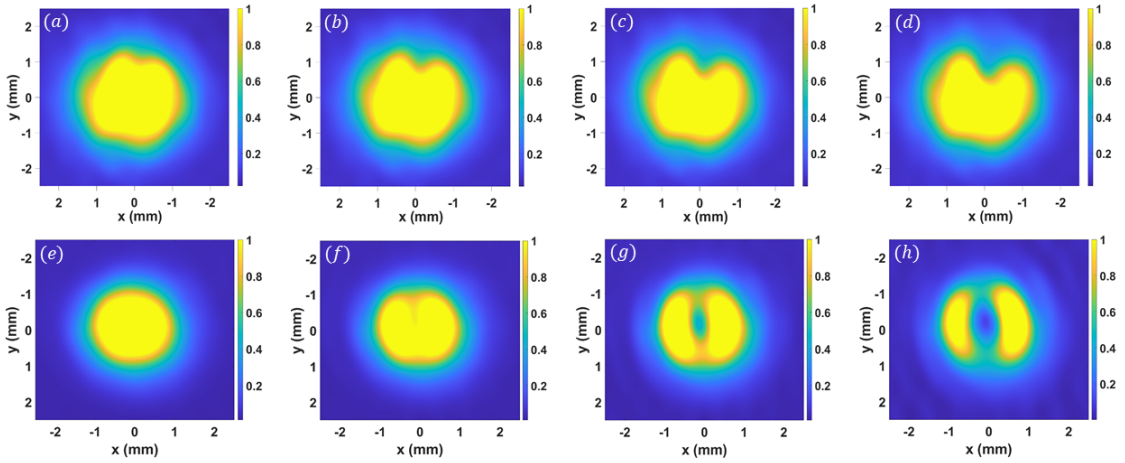

Figure 5.4: (a)-(d) represents experimentally measured probe beam profiles at the far field ($z = \frac{T}{2} + 30\ cm$) for $w_x = 500\ \mu m$ and $w_y = 1200\ \mu m$ at average pump beam power of (a) $30\ mW$, (b) $150\ mW$, (c) $300\ mW$, (d) $500\ mW$ respectively. (e)-(h) experimentally measured probe beam profiles at the far field ($z = \frac{T}{2} + 30\ cm$) for $w_x = 150\ \mu m$ and $w_y = 1200\ \mu m$ at average pump power of (e) $30\ mW$, (f) $150\ mW$, (g) $300\ mW$, (h) $500\ mW$ respectively.

tively compared with the simulated probe beam profiles in Fig. 5.2(a)-(d) where probe beam distortion is apparent. Subsequently, we employed a CL of focal length $f = 100\ mm$ which resulted in $w_x \approx 150\ \mu m$ and $w_y \approx 1200\ \mu m$ at focus (ellipticity ≈ 0.88) and the recorded probe beams are shown in Fig. 5.4(e)-(h). At an average pump power $P_p \geq 300\ mW$, there is a discernible splitting of the probe beam into two crescent-shaped lobes and the separation between the lobes increases as a function of pump power P_p. When $P_p \approx 500\ mW$, the separation between lobes were recorded to be $\approx 1.6\ mm$ on the CCD camera plane. The distance between exit face of the cuvette and the CCD plane is $\approx 30\ cm$. The diffraction-limited tracing of the probe beam to the cuvette exit plane gives $\approx 0.15\ mm$ separation between the lobes in the near-field. This closely resembles the separation obtained from the simulated probe beam profile shown in Fig. 5.2(h) which essentially implies that the asymmetry in pump beam ($\vec{\mathcal{B}} \neq 0$) results in generation of eigenmodes $|\Psi'_{\pm}\rangle$.

It is worth pointing out that each of the lobes ($|\Psi'_{\pm}\rangle$) have quantized (but opposite) phase.

In order to experimentally ascertain that, we follow a two step procedure, namely (i) setting a balanced Mach-Zehnder interferometer (MZI) which is followed by (ii) an appropriate phase retrieval algorithm for obtaining the acquired geometric phase. The MZI is slightly misaligned at the combining non-polarizing beam splitter for obtaining straight-line fringes. The reference and the signal probe intensities are subtracted from the recorded fringe pattern at different pump powers that are shown in Figs. 5.5(a)-(d). When $P_p \leq 150\ mW$ (with ellipticity ≈ 0.88), the phase distribution across the wavefront remains uniform. The modification in fringe pattern is discernible at high pump power and the lobes are distinguishable at $P_p \approx 500\ mW$. In order to extract phase information from the recorded fringe pattern, a Fourier transform based phase retrieval algorithm is implemented [43] (see appendix B for more details). As a first step, we carry out a spatial Fourier transformation of the recorded fringe patterns (Figs. 5.5(a)-(d)) which is represented by three distinct peaks on the Fourier plane. The spatial Fourier spectrum is marked by two spatial frequency components symmetrically positioned about the *zeroth*-order component. A centroid-based approach, rather than a peak-based approach, was employed for accurately ascertaining the coordinates of the side lobes [44, 45]. Since, both the side lobes carry identical phase information, any one of them is employed for retrieving the phase distribution across the probe beam wavefront. In order to compensate the computational artifacts, we shifted the selected side lobe to the origin and eventually, carried out an inverse Fourier transform for obtaining the phase distribution. It is worth noting that the recovered phase distribution undergoes abrupt phase jumps within the computational window (wavefront) and contains arbitrary phase information at the regions of null intensity. This is essentially a consequence of phase-profile wrapping within a sector from $-\pi$ to π. A *transport of intensity* (TIE) based algorithm was employed for unwrapping of the computationally recovered phase distribution across the wavefront [46, 47, 48, 49, 50]. In the TIE algorithm, the complex-field is estimated at two de-focused planes along with one focused plane via propagating the field using angular

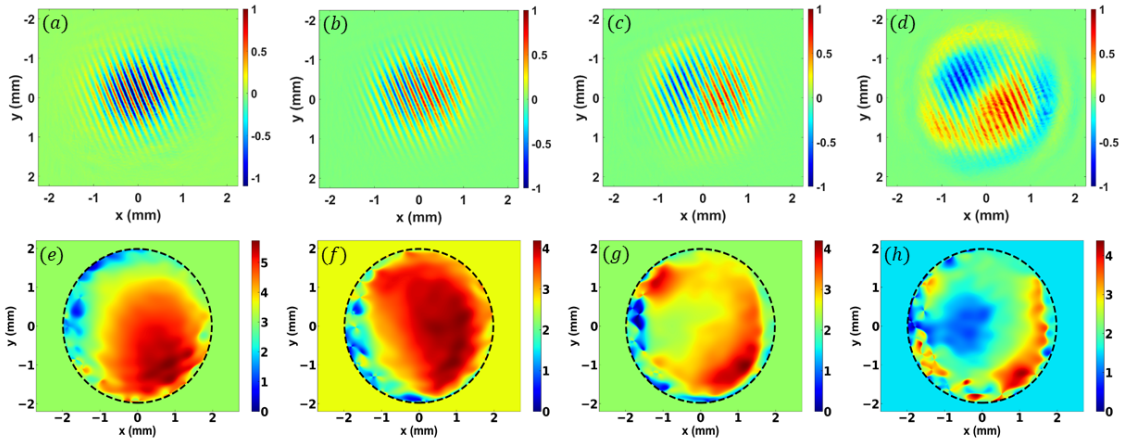

Figure 5.5: (a)-(d) represents the subtracted pattern of interfering beams from the interference pattern for $w_x = 150\ \mu m$ and $w_y = 1200\ \mu m$ at average pump power of (a) $30\ mW$, (b) $150\ mW$, (c) $300\ mW$, (d) $500\ mW$ respectively. (e)-(h) represents computationally retrieved unwrapped phase profile from the subtracted fringe pattern, for $w_x = 150\ \mu m$ and $w_y = 1200\ \mu m$ at average pump power of (e) $30\ mW$, (f) $150\ mW$, (g) $300\ mW$, (h) $500\ mW$ respectively.

spectrum method. This is followed by solving the Helmholtz equation and the recovered unwrapped phase distribution is shown in figures 5.5(e)-(h) at different pump powers. The black dotted circle represents the computational window. It is apparent that there is a phase redistribution at $P_p \approx 500\ mW$ and the probe beam could be distinctly divided into two regions such that these two regions bear opposite signs. A comparison with the Fig. 5.4(h) allows us to infer that the two crescent-shaped lobes have opposite phases. In other words, it depicts a situation where the photons in two eigenmodes $|\Psi'\rangle$ are opposite in phase *i.e.* the spinor of the transformed Hamiltonian (in Eq. 5.6) are spatially separated. This has a distinct analogy with SHE in purely nonlinear optical configuration.

5.5 Conclusion

We presented an analytical framework for understanding the dynamics of a $\chi^{(3)}$ nonlinear optical interaction from a spin-transport perspective and consequently, we drew a connec-

tion between probe beam restructuring with geometric manifestations of self-action type interaction. In order to realize non-trivial topological manifestation, a non-zero synthetic magnetic field is constructed using an elliptic Gaussian pump beam. This is accompanied by a z-dominant synthetic magnetization which leads to non-trivial splitting of probe beam. The analytical formalism adopts gauge transformations that define the vector as well as scalar gauge-fields naturally without the explicit knowledge of dressed-state. Consequently, the approach allows us to set-up equivalent 'equations of motion' for the dressed-states which provides a simplified tool for determining the alterations in the probe beam. The experimentally observed crescent-shaped lobes are the equivalent *pseudo*-spin accumulation in real space, which is essentially a consequence of SHE. The phase retrieval of the recorded spatial bands elucidates the formation of oppositely directed *pseudo*-spin states. A full quantum mechanical treatment of the $\chi^{(3)}$ based interaction will provide a feasible scheme for utilizing the spatial beam restructuring for quantum information transport and processing. Since, $\chi^{(3)}$ is relatively small for liquids and solids, a near-resonant self-action effect in a thermal vapor, or preferably a cold-atom ensemble, would be a more viable system for observing such effects at single-photon level.

References

[1] Robert Oeckl. The quantum geometry of spin and statistics. *Journal of Geometry and Physics*, 39(3):233–252, 2001.

[2] P. A. M. Dirac and J. C. Polkinghorne. The principles of quantum mechanics. *Physics Today*, 11(6):32–33, 06 1958.

[3] Walther Gerlach and Otto Stern. Der experimentelle Nachweis der Richtungsquantelung im Magnetfeld. *Zeitschrift fur Physik*, 9:349–352, December 1922.

[4] Horst Schmidt-Böcking, Lothar Schmidt, Hans Jürgen Lüdde, Wolfgang Trageser, Alan Templeton, and Tilman Sauer. The Stern-Gerlach experiment revisited. *The European Physical Journal H*, 41(4-5):327–364, November 2016.

[5] Leon Karpa and Martin Weitz. A stern–gerlach experiment for slow light. *Nature Physics*, 2(5):332–335, May 2006.

[6] Iacopo Carusotto and Cristiano Ciuti. Quantum fluids of light. *Rev. Mod. Phys.*, 85:299–366, Feb 2013.

[7] Mandip Singh. Quantum Stern-Gerlach experiment and path entanglement of a Bose-Einstein condensate. *Physical Review A*, 95(4):043620, April 2017.

[8] Igor Žutić, Jaroslav Fabian, and S. Das Sarma. Spintronics: Fundamentals and applications. *Rev. Mod. Phys.*, 76:323–410, Apr 2004.

[9] Atsufumi Hirohata, Keisuke Yamada, Yoshinobu Nakatani, Ioan-Lucian Prejbeanu, Bernard Diény, Philipp Pirro, and Burkard Hillebrands. Review on spintronics: Principles and device applications. *Journal of Magnetism and Magnetic Materials*, 509:166711, 2020.

[10] S. S. P. Parkin, K. P. Roche, M. G. Samant, P. M. Rice, R. B. Beyers, R. E. Scheuerlein, E. J. O'Sullivan, S. L. Brown, J. Bucchigano, D. W. Abraham, Yu Lu, M. Rooks, P. L. Trouilloud, R. A. Wanner, and W. J. Gallagher. Exchange-biased magnetic tunnel junctions and application to nonvolatile magnetic random access memory (invited). *Journal of Applied Physics*, 85(8):5828–5833, 04 1999.

[11] Diana C. Leitao, Floris J. F. Van Riel, Mahmoud Rasly, Pedro D. R. Araujo, Maria Salvador, Elvira Paz, and Bert Koopmans. Enhanced performance and functionality in spintronic sensors. *npj Spintronics*, 2(1):54, nov 2024.

[12] Tuantuan Li, Qin Shi, Zhang Lei, Lin He, and Bingjiao Liu. Research on mechanism and key technology of intelligent vehicles brake by wire system. In *2019 3rd Conference on Vehicle Control and Intelligence (CVCI)*, pages 1–8, 2019.

[13] Stuart S. P. Parkin, Masamitsu Hayashi, and Luc Thomas. Magnetic domain-wall racetrack memory. *Science*, 320(5873):190–194, 2008.

[14] Swaroop Ghosh. Spintronics and security: Prospects, vulnerabilities, attack models, and preventions. *Proceedings of the IEEE*, 104(10):1864–1893, 2016.

[15] P. Bruno, V. K. Dugaev, and M. Taillefumier. Topological hall effect and berry phase in magnetic nanostructures. *Phys. Rev. Lett.*, 93:096806, Aug 2004.

[16] A. Neubauer, C. Pfleiderer, B. Binz, A. Rosch, R. Ritz, P. G. Niklowitz, and P. Böni. Topological hall effect in the *A* phase of mnsi. *Phys. Rev. Lett.*, 102:186602, May 2009.

[17] Han Wang, Yingying Dai, Gan-Moog Chow, and Jingsheng Chen. Topological hall transport: Materials, mechanisms and potential applications. *Progress in Materials Science*, 130:100971, 2022.

[18] Sheng Yang, Yuelei Zhao, Xichao Zhang, Xiangjun Xing, Haifeng Du, Xiaoguang Li, Masahito Mochizuki, Xiaohong Xu, Johan Åkerman, and Yan Zhou. Fundamentals and applications of the skyrmion hall effect. *Applied Physics Reviews*, 11(4):041335, 12 2024.

[19] Zhejunyu Jin, Zhaozhuo Zeng, Yunshan Cao, and Peng Yan. Skyrmion hall effect in altermagnets. *Phys. Rev. Lett.*, 133:196701, Nov 2024.

[20] Yijie Shen, Qiang Zhang, Peng Shi, Luping Du, Xiaocong Yuan, and Anatoly V. Zayats. Optical skyrmions and other topological quasiparticles of light. *Nature Photonics*, 18(1):15–25, Jan 2024.

[21] Gil Bashan, Shani Izhak, Ofir Yesharim, and Ady Arie. Spintronic effects and devices in nonlinear optics. *APL Photonics*, 10(1):010904, 01 2025.

[22] Aiping Yang, Aru Kong, Fanfei Meng, Xusheng Chen, Min Lin, Peng Shi, Luping Du, Xiaocong Yuan, and Biao Wang. Optical skyrmions: from fundamentals to applications. *Journal of Optics*, 27(4):043002, Feb 2025.

[23] Wenyu Gao, Yuan Zhou, Xing Li, Yanan Zhang, Qiang Zhang, Manman Li, Xianghua Yu, Shaohui Yan, Xiaohao Xu, and Baoli Yao. Topological light field: from singular to skyrmionic optics and beyond. *Journal of Optics*, 27(8):083001, Aug 2025.

[24] Alexey Kavokin, Guillaume Malpuech, and Mikhail Glazov. Optical spin hall effect. *Phys. Rev. Lett.*, 95:136601, Sep 2005.

[25] C. Leyder, M. Romanelli, J. Ph. Karr, E. Giacobino, T. C. H. Liew, M. M. Glazov, A. V. Kavokin, G. Malpuech, and A. Bramati. Observation of the optical spin hall effect. *Nature Physics*, 3(9):628–631, Sep 2007.

[26] Fu Liu, Saisai Wang, Shiyi Xiao, Zhi Hong Hang, and Jensen Li. Polarization-dependent optics using gauge-field metamaterials. *Applied Physics Letters*, 107(24):241106, 12 2015.

[27] Aviv Karnieli, Shai Tsesses, Guy Bartal, and Ady Arie. Emulating spin transport with nonlinear optics, from high-order skyrmions to the topological hall effect. *Nature Communications*, 12(1):1092, Feb 2021.

[28] Shani Izhak, Aviv Karnieli, Ofir Yesharim, Shai Tsesses, and Ady Arie. All-optical spin valve effect in nonlinear optics. *Opt. Lett.*, 49(4):1025–1028, Feb 2024.

[29] Sourabh Jain, May H. Hlaing, Kang-Chieh Fan, Jason Midkiff, Shupeng Ning, Cheng-hao Feng, Po-Yu Hsiao, Patrick T. Camp, and Ray T. Chen. Incubating advances in integrated photonics with emerging sensing and computational capabilities. *Applied Physics Reviews*, 12(1):011337, 03 2025.

[30] Xuhan Guo, Xingchen Ji, Baicheng Yao, Teng Tan, Allen Chu, Ohad Westreich, Avik Dutt, Cheewei Wong, and Yikai Su. Ultra-wideband integrated photonic devices on silicon platform: from visible to mid-ir. *Nanophotonics*, 12(2):167–196, 2023.

[31] P. L. Kelley. Self-focusing of optical beams. *Phys. Rev. Lett.*, 15:1005–1008, Dec 1965.

[32] Eyal Feigenbaum, Jean-Michel G. Di Nicola, and Jeff D. Bude. Revisiting beam filamentation formation conditions in high power lasers. *Opt. Express*, 27(8):10611–10630, Apr 2019.

[33] N. Westerberg, C. Maitland, D. Faccio, K. Wilson, P. Öhberg, and E. M. Wright. Synthetic magnetism for photon fluids. *Phys. Rev. A*, 94:023805, Aug 2016.

[34] Shani Izhak, Aviv Karnieli, Ofir Yesharim, Shai Tsesses, and Ady Arie. Pseudospin transverse localization of light in an optical disordered spin-glass phase. *Phys. Rev. Lett.*, 134:123803, Mar 2025.

[35] J. T. Mendonça. Self-phase modulation and superfluidity in twisted fluids of light. *Europhysics Letters*, 129(6):64004, apr 2020.

[36] Carl M. Bender and Stefan Boettcher. Real spectra in non-hermitian hamiltonians having $\mathcal{PT}$ symmetry. *Phys. Rev. Lett.*, 80:5243–5246, Jun 1998.

[37] A. Guo, G. J. Salamo, D. Duchesne, R. Morandotti, M. Volatier-Ravat, V. Aimez, G. A. Siviloglou, and D. N. Christodoulides. Observation of $\mathcal{PT}$-symmetry breaking in complex optical potentials. *Phys. Rev. Lett.*, 103:093902, Aug 2009.

[38] Carl M. Bender, Dorje C. Brody, and Hugh F. Jones. Complex extension of quantum mechanics. *Phys. Rev. Lett.*, 89:270401, Dec 2002.

[39] Robert W. Boyd. *Nonlinear Optics*. Academic Press, Inc., 3rd edition, 2008.

[40] Soumik Nandi, Arannya Ghosh, Dinesh Beniwal, Abhishek Mondal, Ashok K. Mohapatra, and Ritwick Das. All-optical stern-gerlach effect in a parity-time anti-symmetric nonlinear refractive medium. *Opt. Express*, 33(12):24237–24248, Jun 2025.

[41] Karin Everschor-Sitte and Matthias Sitte. Real-space berry phases: Skyrmion soccer (invited). *Journal of Applied Physics*, 115(17):172602, 04 2014.

[42] M. Sheik-Bahae, D. J. Hagan, and E. W. Van Stryland. Dispersion and band-gap scaling of the electronic kerr effect in solids associated with two-photon absorption. *Phys. Rev. Lett.*, 65:96–99, Jul 1990.

[43] Mitsuo Takeda, Hideki Ina, and Seiji Kobayashi. Fourier-transform method of fringe-pattern analysis for computer-based topography and interferometry. *J. Opt. Soc. Am.*, 72(1):156–160, Jan 1982.

[44] Nishant Goyal and Kedar Khare. Carrier-frequency estimation for digital holograms of phase objects. *Appl. Opt.*, 63(7):B42–B48, Mar 2024.

[45] Mandeep Singh and Kedar Khare. Accurate efficient carrier estimation for single-shot digital holographic imaging. *Opt. Lett.*, 41(21):4871–4874, Nov 2016.

[46] Kazuyoshi Itoh. Analysis of the phase unwrapping algorithm. *Appl. Opt.*, 21(14):2470–2470, Jul 1982.

[47] Michael Reed Teague. Deterministic phase retrieval: a green's function solution. *J. Opt. Soc. Am.*, 73(11):1434–1441, Nov 1983.

[48] Richard M. Goldstein, Howard A. Zebker, and Charles L. Werner. Satellite radar interferometry: Two-dimensional phase unwrapping. *Radio Science*, 23(4):713–720, 1988.

[49] Kazuo Ishizuka and Brendan Allman. Phase measurement of atomic resolution image using transport of intensity equation. *Journal of Electron Microscopy*, 54(3):191–197, 08 2005.

[50] Neeraj Pandey, Amitava Ghosh, and Kedar Khare. Two-dimensional phase unwrapping using the transport of intensity equation. *Appl. Opt.*, 55(9):2418–2425, Mar 2016.

Chapter 6

Conclusion and Future Prospect

6.1 Conclusions

Self action effect is one of the most prevalent third-order nonlinear optical process and it has been investigated intensively for nearly half a century now. A high intense laser beam is responsible for creating two ansatz fields (a_+ and a_-) through *filamentation* process while propagating through a medium exhibiting $\chi^{(3)}$ nonlinearity. The propagation of pump and newly generated beams is governed by the nonlinear Schrödinger equation (NLSE). Under low pump depletion approximation, coupled wave equations (CWEs) governing the dynamics of a_+ and a_- are modelled in a quantum mechanical Schrödinger equation-like form where amplitudes of generated fields constitute the state of this system i.e. $|\Psi\rangle = (a_+ \quad a_-^*)^T$. The Hamiltonian ($\hat{H}$), describing such a dynamical system under suitable rotation and approximation mimics the Hamiltonian of a charged particle in an *electromagnetic* field. Hence, an electric field ($\vec{\mathcal{E}}$) and a magnetic field ($\vec{\mathcal{B}}$), both synthetic in nature, are created through our formalism and a synthetic magnetization ($\vec{\mathcal{M}}$) is also defined in this process. Both beam a_+ & a_- are assigned with two opposite pseudo-charges $q_{e_\pm}$ so an equal and opposite amount of Lorentz force $\left(\vec{\mathcal{F}} = q_e\left[\vec{\mathcal{E}} + \vec{v} \times \vec{\mathcal{B}}\right]\right)$ acts on them. It gives us an alternate route to ascertain the dynamics of ansatz fields by utilizing the equation of motion evaluated from the Lorentz force instead of explicitly solving CWEs. Here, we notice that $\hat{H}$ is non-Hermitian in nature but it satisfies anti-commutation with $\hat{\mathcal{P}}\hat{\mathcal{T}}$ operator. On explicit mathematical computing, it turns out that eigenvalues of $\hat{H}$ are real only when $\chi^{(3)} < 0$. We used a frequency-doubled $Nd : YVO_4$ pulsed laser

delivering pulses of $\sim 0.7\ ps$ as pump beam for our experimentation. The laser is operated at $80\ kHz$ repetition rate and at this experimental condition, our nonlinear medium *toluene* displays a negative $\chi^{(3)}$ which would make our system to have real eigenvalues. A He-Ne laser is used as *probe* beam to observe the effects created by the pump beam.

It is also identified that both electric and magnetic field depend upon $\vec{\mathcal{M}}$ which further depends on the pump beam characteristics. Two different transverse pump wavefront (a) Gaussian and (b) Elliptic Gaussian are considered for tuning the synthetic fields.

For Gaussian pump profile, $\vec{\mathcal{B}}$ vanishes but $\vec{\mathcal{E}}$ remains non-zero due to azimuthal symmetry of pump beam. The artificial scalar potential in this case $\mathcal{V} = -\vec{\sigma} \cdot \vec{\mathcal{M}}$ reminds us of potential of Stern-Gerlach experiment $V = -\vec{\mu} \cdot \vec{B}_S$ where $\vec{B}_S$ is the external applied magnetic field. In the current scenario, $\chi^{(3)}$ mediated interaction imitates the SG effect but due to azimuthal symmetry, the beams get deflected in all transverse directions by an equal amount instead of single directional splitting in original SG effect. This result in generation of a hollow Gaussian beam with no orbital angular momentum which is further confirmed experimentally by standard techniques.

For Elliptic Gaussian (EG) pump profile, azimuthal symmetry is broken so we now have a non-zero $\vec{\mathcal{B}}$ pointed in longitudinal direction (along $\hat{z}$) alongside a non-zero $\vec{\mathcal{E}}$ acting transversely (along $\hat{r}_T$). So, pseudo-charged particle travels where $\vec{\mathcal{E}}$ and $\vec{\mathcal{B}}$ are pointing at right angles and both are completely dependent on magnetization $\vec{\mathcal{M}}$ created by EG pump. This is analogous to the topological Hall effect (THE) and just like the original system, here oppositely pseudo-charged particles move in opposite directions that creates a crescent-like pattern. Also in THE, electrons acquire a non-zero phase depending upon the local magnetization texture and here we have both theoretically and experimentally observed that both a_+ and a_- acquire a non-zero geometric phase depending on pump beam topology.

6.2 Future Prospect

Since, $\chi^{(3)}$ is relatively small for liquids and solids, a near-resonant self-action effect in a thermal vapor, or preferably a cold-atom ensemble, would be a more viable system for observing filamentation effects at the single-photon level. $\chi^{(3)}$ is tunable in atomic system depending upon energy level transition *i.e.* detuning of medium. Changing detuning both $\chi^{(3)} < 0$ and $\chi^{(3)} > 0$ are achievable in a single medium and controlling pump intensity, an exceptional point (EP) can be encountered. This would open up multiple application avenues like sensing. Also, for $\chi^{(2)}$ mediated parametric down conversion process shows non-Hermitian nature. Down-converted photons *viz.* signal and idler would acquire phase depending upon pump profile that would be beneficial for quantum computing. To observe an EP in $\chi^{(2)}$, apart from intensity, phase mismatch of interacting beams has to be changed which can be made possible by utilizing the thermo-optic manifestation of anisotropic crystals.

Appendix A

A.1 Estimation of $\chi^{(3)}$ and single-beam Z-scan experiment

The experimental Z-scan configuration includes frequency-doubled $Nd:YVO_4$ laser delivering Fourier-transform limited $0.7\ ns$ pulses as an excitation source. The laser delivers an average power of $\approx 500\ mW$ at a central wavelength of $\lambda_0 = 532\ nm$. The pulse repetition rate is fixed to $80\ kHz$ and a combination of half-wave plate (HWP) and polarising cubic beam splitter (PBS) is used for controlling the optical power incident on the nonlinear optical (NLO) medium which is $1\ mm$ thick cuvette containing toluene. The excitation beam is focused to a $\approx 40\ \mu m$ spot size using a plano-convex lens (L) of $100\ mm$ focal length. The NLO medium was placed on a translation stage which traverses a distance of $110\ mm$ through the focal point ($z = 0$) of the excitation laser beam. Two photodetectors D_1 and D_2 are used for measuring the power in the reference beam (at the PBS) and the transmitted beam (from S) respectively. In the closed aperture (CA) Z- scan configuration, an aperture (A), with $\leq 25\%$ transmittance is placed adjacent to detector D_2 for estimating the nonlinear refractive index (n_2). A pre-focal peak in the transmittance curve is indicative of $n_2 < 0$ which has been observed in our case. On the other hand, the absence of aperture, also known as open-aperture (OA) measurement, allows the estimation of NLO absorption. In order to accurately estimate the n_2 and hence, $\chi^{(3)}$ for toluene, the measured CA transmittance curves were fitted using the relation [1]

$$\Delta T = 1 - \frac{4x\Delta\phi_0}{(x^2+9)(x^2+1)} \tag{A.1}$$

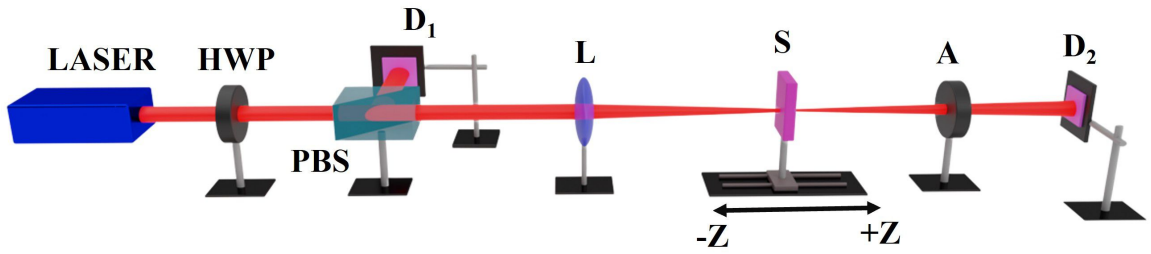

Figure A.1: Schematic to show single-beam Z-scan experiment using frequency-doubled $Nd:YVO_4$ laser.

where $\Delta\phi_0 = \frac{\omega_p}{c} n_2 I_0 L_{eff}$ is the phase change due to nonlinear refraction at the focus with $\omega_p = \frac{2\pi c}{\lambda_o}$, L_{eff} = (1 - $e^{-\alpha L}$)/α is the effective length of the medium, L is the cuvette length and α is the linear absorption of toluene, $x = z/z_0$ where z_0 is Rayleigh length for the excitation laser beam. An accurate fitting yields the value of n_2 which is related to $Re(\chi^{(3)})$ through [2]

$$\chi^{(3)} = \left[\frac{n_p^2 c}{12\pi^2}\right] n_2 \tag{A.2}$$

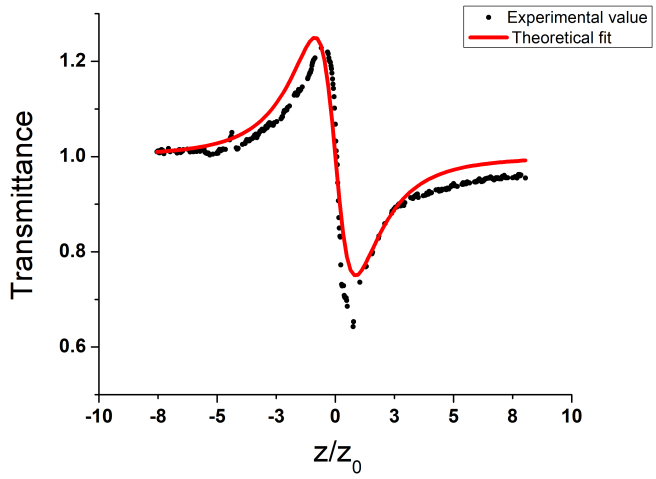

Figure A.2: Normalized transmittance for closed aperture Z-scan measurement of toluene. Black dots represent the recorded transmittance and the solid (red) line represents the theoretical fit.

The theoretical fits yields real part of third-order nonlinear susceptibility of toluene to be $Re(\chi^{(3)}) \approx -2.9 \times 10^{-19}\ m^2/V^2$.

References

[1] M. Sheik-Bahae, A.A. Said, T.-H. Wei, D.J. Hagan, and E.W. Van Stryland. Sensitive measurement of optical nonlinearities using a single beam. *IEEE Journal of Quantum Electronics*, 26(4):760–769, 1990.

[2] Robert W. Boyd. *Nonlinear Optics*. Academic Press, Inc., 3rd edition, 2008.

Appendix B

B.1 Phase retrieval through Fourier Transform

Interferometry is the most widely used process for evaluating phase information in any interaction [1]. Interferogram recorded in a perfectly aligned interferometer would readily give us the required phase change but this requires greater precision and control in the setup. Instead, when the interacting beams are aligned in a tilted fashion, straight line fringes appear in the camera and the intensity pattern I_0 can be represented as

$$I_0(x,y) = I_1(x,y) + I_2(x,y)\cos\{(f_{x0}\,x + f_{y0}\,y) + \xi(x,y)\} \tag{B.1}$$

where f_{x0} and f_{y0} are the carrier frequencies along x and y direction respectively associated with the straight line pattern and $\xi(x,y)$ is the phase variation across the beam wavefront. To extract phase information, we employ a Fourier transform-based phase retrieval technique given by Takeda *et.al* [2] in 1982. Experimentally, we first setup a balanced Mach-Zehnder interferometer for probe beam and then separately recorded the intensity profiles of signal (experimental) arm (I_E) as well as reference arm (I_R) when they are not interfering. Finally, we recorded the generated interference pattern (I_F) at input pump beam power $500\ mW$ which is shown in Fig. B.1(a). Figure B.1(b) and B.1(c) show the transmitted probe beam profile (I_E) through *toluene* and reference probe beam profile (I_R) respectively, recorded at the CCD, at the same input pump power level of $500\ mW$. Then we subtract I_E and I_R from fringe pattern I_F and that subtracted intensity profile $\Delta I = I_F - I_R - I_E$ is shown in Fig. B.1(d). This subtracted intensity will be used as I_0 as shown in Eq. (B.1), i.e. $\Delta I \equiv I_0$.

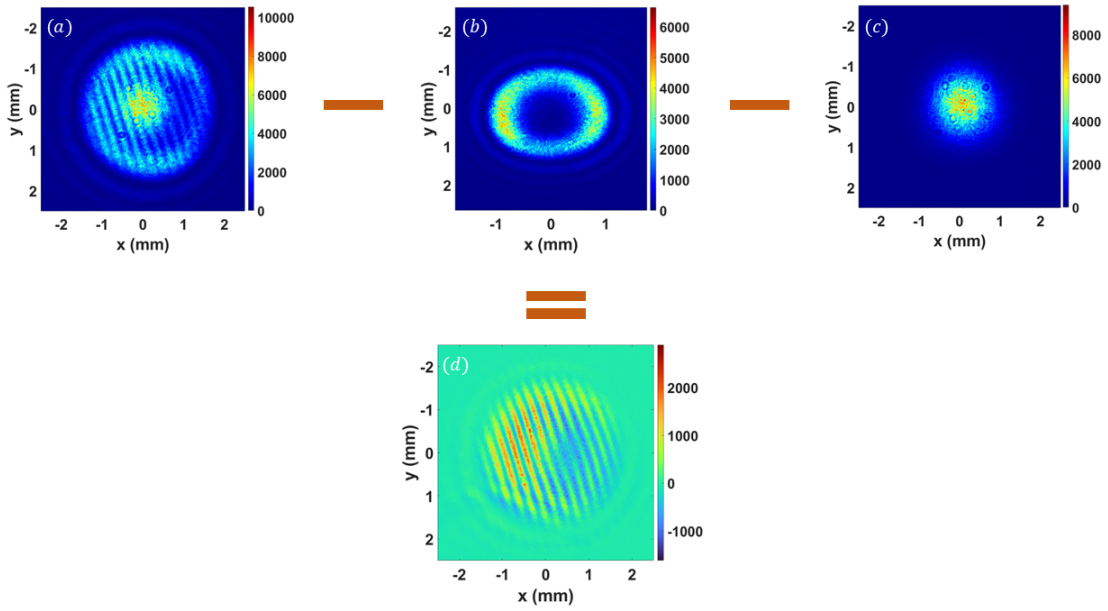

Figure B.1: (a) shows recorded interference fringe pattern at $500\ mW$, (b) shows recorded pattern of the beam travelling through nonlinear medium (toluene) and (c) shows recorded reference Gaussian beam pattern at the mentioned power level. (d) represents the subtracted intensity profile

A slight tilting of interfering beams provides an advantage from an experimental perspective, but at the cost of introducing a spatial periodicity component with the required phase. For convenience, we rewrite Eq. (B.1) in following fashion

$$I_0(x,y) = I_1(x,y) + I_3(x,y)\, e^{i(f_{x0}\ x + f_{y0}\ y)} + I_3^*(x,y)\, e^{-i(f_{x0}\ x + f_{y0}\ y)} \tag{B.2}$$

Here, we have defined $I_3 = \frac{1}{2} I_2(x,y)\ exp[i\xi(x,y)]$ which contain the phase variation. Now we perform a 2D Fourier transform of Eq. (B.2) and it turns out

$$\widetilde{I}_0(f_x,f_y) = \widetilde{I}_1(f_x,f_y) + \widetilde{I}_3(f_x - f_{x0}, f_y - f_{y0}) + \widetilde{I}_3^*(f_x + f_{x0}, f_y + f_{y0}) \tag{B.3}$$

Here tilde defines the Fourier transformed function. The Fourier-transformed pattern of intensity profile of Fig. B.1(d) is shown in Fig. B.2(a). As per Eq. (B.3), Fourier spectrum has three distinct components. One DC component at center and two non-zero components

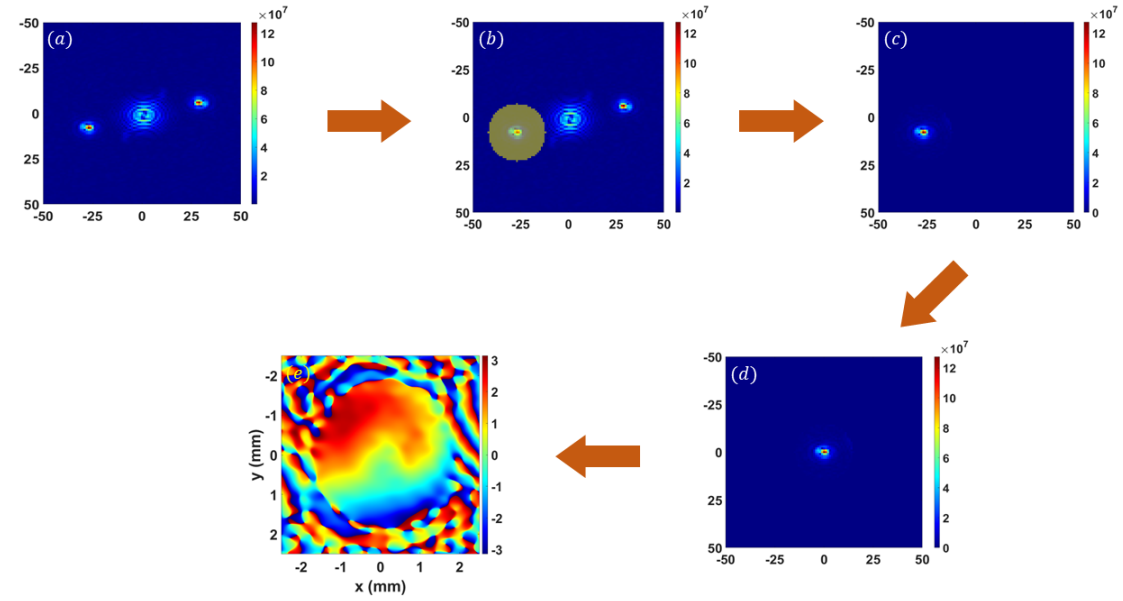

Figure B.2: (a) shows Fourier transformed spectrum of the subtracted fringe pattern, (b) a mask is applied on either of the non-zero values in Fourier domain, (c) only the masked region survives and the rest is eliminated from the algorithm, (d) shows that the masked region has been shifted to the origin to remove carrier frequency contribution, (e) shows phase variation in real space evaluated through inverse Fourier transform.

related to the carrier frequency, positioned symmetrically at a distance of $\sqrt{f_{x0}^2 + f_{y0}^2}$ from the center in Fourier domain. This is confirmed by the computed Fast Fourier Transform (FFT) image shown in Fig. B.2(a). Our interest is in the non-zero contributions because it contains the required phase information [see Eq. (B.2) and (B.3)]. So, we have to remove the DC part and for that, we have to choose either of $\widetilde{I}_3$ and $\widetilde{I}_3^*$ due to their identical nature. Numerically, we apply a circular mask of radius of 15 pixels on $\widetilde{I}_3^*$ and it has been shown in Fig. B.2(b). Next, only the masked region is survived and the rest is eliminated for further processing and the resultant is presented in Fig. B.2(c). We shift the masked region by an amount of $\sqrt{f_{x0}^2 + f_{y0}^2}$ to bring into center which makes the Fourier form $\widetilde{I}_3^*(f_x, f_y)$. Figure B.2(d) depicts that the masked region is shifted to the origin in Fourier domain. Finally, an inverse Fourier transform (IFT) is performed to produce corrected pattern in real space.

Mathematically, $\widetilde{I_3^*}(f_x, f_y) \xrightarrow{IFT} I_3^*(x, y)$ and to extract phase we further decompose intensity into amplitude and phase using logarithm as stated below

$$\ln\left[I_3^*(x,y)\right] = \ln\left[\left(\frac{1}{2}\right) I_2(x,y)\right] - i\xi(x,y) \tag{B.4}$$

It is now extremely convenient to evaluate the phase from the intensity profile and numerically achieved phase for probe beam at input pump power of $500\ mW$ is plotted in Fig. B.2(e).

The phase in Fig. B.2(e) evaluated through above technique has range from $-\pi$ to π. But, Fourier transform based technique is not sufficient to resolve any phase jump present at any point of the beam wavefront. So, this phase is known as *wrapped* phase. To extract the amount of phase change in the range from 0 to multiples of 2π to avoid phase jumps, we have to unwrap [3, 4] the previously obtained phase. To do that, we perform a Transfer of Intensity Equation (TIE) based phase unwrapping technique [5, 6]. The unwrapped phase for average pump power of $500\ mW$ is shown in Fig. 5.5(h).

References

[1] Joseph W Goodman. Introduction to fourier optics. *3rd ed., by Englewood, CO: Roberts & Co. Publishers*, 1, 2005.

[2] Mitsuo Takeda, Hideki Ina, and Seiji Kobayashi. Fourier-transform method of fringe-pattern analysis for computer-based topography and interferometry. *J. Opt. Soc. Am.*, 72(1):156–160, Jan 1982.

[3] Kazuyoshi Itoh. Analysis of the phase unwrapping algorithm. *Appl. Opt.*, 21(14):2470–2470, Jul 1982.

[4] Richard M. Goldstein, Howard A. Zebker, and Charles L. Werner. Satellite radar interferometry: Two-dimensional phase unwrapping. *Radio Science*, 23(4):713–720, 1988.

[5] Michael Reed Teague. Deterministic phase retrieval: a green's function solution. *J. Opt. Soc. Am.*, 73(11):1434–1441, Nov 1983.

[6] Neeraj Pandey, Amitava Ghosh, and Kedar Khare. Two-dimensional phase unwrapping using the transport of intensity equation. *Appl. Opt.*, 55(9):2418–2425, Mar 2016.